UNIVERSITY OF CALIFORNIA, IRVINE

Morphologically Distinct Cell Delivery Composites and Tissue Integrating Implants Processed Using Bijels

DISSERTATION

submitted in partial satisfaction of the requirement for the degree of

DOCTOR OF PHILOSOPHY

in Chemical and Biochemical Engineering

by

Todd James Thorson

Dissertation Committee:
Professor Ali Mohraz, Chair
Professor Elliot Botvinick, Chair
Professor Wendy Liu

2019

DEDICATION

To Floyd

TABLE OF CONTENTS

LIST OF FIGURES

LIST OF TABLES

LIST OF EQUATIONS

ACKNOWLEDGEMENTS

Thank you, Ali and Elliot. For taking a chance on me in beginning this collaboration, for always guiding and pushing me towards work that I can feel proud of, for your patience with my shortcomings, for your trust, and for setting an example as truly exceptional members of the academic community.

Thank you to my many CSL and BEAMS lab-mates. For teaching me techniques upon joining the lab, listening to my research problems, fleshing out random ideas, making the lab an enjoyable place, and for being easy targets inside the laser tag arena. Particular thank you to Dr. Jessica Witt for teaching me all bijel and bijel processing techniques, to Dr. Mark Keating for your seemingly endless knowledge about all topics, especially coding in ImageJ and MATLAB, and to Rachel Gurlin for helping get my materials implanted.

Thank you, Ann. For always being there for me, through fun rides in the rain, taking care of the cats, or helping me find a room to work in.

Thank you, Linda. For teaching me cell culture, always providing PBS when my “stray cat” persona walked through the door, and your work in developing the green fluorescent “Hulk” cells.

Thank you, parents, siblings, and lifelong friends. For always listening and supporting me, for understanding when I could not always make it home for holidays, and for taking the time and resources to visit me periodically during this chapter of my life.

Thank you, Kristin. For your love and support.
From the Brooklyn Bridge to the Orange County beaches, you bring the brightness to my life.

Thank you, publishers for granting permission to use copyrighted materials to support this dissertation. Permission granted from Copyright Clearance Center, Inc.

CURRICULUM VITAE

EDUCATION

2019 Doctor of Philosophy – Chemical and Biochemical Engineering, University of California, Irvine, Irvine, California, USA. Advisors: Ali Mohraz & Elliot Botvinick
NSF IGERT Trainee – Biophotonics Across Energy, Space & Time

2013 Master of Science – Chemical and Biochemical Engineering, University of Iowa, Iowa City, Iowa, USA. Advisor: C. Allan Guymon. Thesis Title: *Phase Behavior and Stimuli Response in Lyotropic Liquid Crystalline Templated Photopolymers*

2011 Bachelor of Science – Chemical and Biological Engineering, Minor – Biology, Iowa State University, Ames, Iowa, USA. Advisor: Jennifer Heinen (O'Donnell)

JOURNAL PUBLICATIONS

1. Thorson TJ, Botvinick EL, Mohraz A. Composite Bijel-Templated Hydrogels for Cell Delivery, ACS Biomaterials Science and Engineering. 2018, 4, 587-594. Doi: 10.1021/acsbiomaterials.7b00809
2. Thorson TJ, Gurlin RE, Botvinick EL, Mohraz A. Bijel-Templated Implantable Biomaterials for Enhancing Tissue Integration and Vascularization. 2019. *Submitted for review*.
3. Thorson TJ, McDevitt KM, Mumm DR, Botvinick EL, Mohraz A. Microstructural Characterization of Bijel-Derived Materials. 2019. *In preparation*.

PATENTS

1. Mohraz A, Thorson TJ, Botvinick EL. Self-Assembly Derived Co-Continuous Materials for Biomedical Devices. Patent Cooperation Treaty. June 8, 2018.
2. Thorson TJ, Groisman L, Mohraz A, Botvinick EL. Tissue Integrated Drug Delivery System. Patent Cooperation Treaty. Jan. 16, 2019.

PRESENTATIONS

1. Society for Biomaterials Annual Meeting, Atlanta, GA, April 2018. Oral Presentation: Foreign body response mitigation and tissue integration in morphologically unique bijel-templated hydrogel implants.
2. American Institute of Chemical Engineers Annual Meeting, Minneapolis, MN, October 2017. Oral Presentation: Tissue response and integration in biomaterial implants derived from morphologically unique emulsion gels.
3. American Chemical Society Colloid and Surface Science Symposium, New York, NY, July 2017. Oral Presentation: Tissue integration and cell delivery using morphologically unique bijel-derived materials.

4. University of California Bioengineering Symposium, Los Angeles, CA, June 2017. Oral Presentation: Tissue response and integration in biomaterial implants derived from morphologically unique emulsion gels.
5. American Institute of Chemical Engineers Annual Meeting, San Francisco, CA, November 2016. Oral Presentation: Cell delivery systems via complex emulsion templated hydrogels.
6. MRSEC Fall Meeting, Madison, WI, September 2012. Poster Presentation: Modeling Lyotropic Liquid Crystal Templated Polymers for Enhanced Stimuli-Sensitivity.
7. American Institute of Chemical Engineers Annual Meeting, Salt Lake City, UT. Poster Presentation: Polymerization of Emulsified Microemulsions

LEADERSHIP ACTIVITIES & TEACHING

Chemical Engineering & Materials Science Graduate Student Association, ChEMS GSA

President	2016-2017
Chemical Engineering Ambassador to the Faculty	2015-2016
First Year Representative	2014-2015

Teaching Assistantships

Introduction to Numerical Methods in Engineering, UC Irvine,	Fall 2016, 2017, 2018
Unit Operations I, UC Irvine,	Fall 2015
Engineering Problem Solving I, University of Iowa	Fall 2012
Process Control, University of Iowa	Fall 2011

PROFESSIONAL SOCIETIES

American Institute of Chemical Engineers (AIChE)
Society for Biomaterials (SFB) – *Tissue Interaction Special Interest Group*

PROFESSIONAL EXPERIENCE

GEA Westfalia Separator, *Process Support Specialist*, Northvale, NJ 2013-2014

ABSTRACT OF THE DISSERTATION

Morphologically Distinct Cell Delivery Composites and Tissue Integrating Implants Processed Using Bijels

by

Todd James Thorson

Doctor of Philosophy in Chemical and Biochemical Engineering

University of California, Irvine, 2019

Professor Ali Mohraz, Chair; Professor Elliot Botvinick, Chair

Biomaterials are engaged ubiquitously to regenerate or replace damaged or diseased tissues. Numerous processing techniques aim to impart interconnected, porous structures within biomaterials to support cell delivery, direct tissue growth, and increase the acceptance of foreign materials in the body. Many processing techniques lack predictable control of scaffold architecture, and rapid prototyping methods are often limited by time-consuming, layer-by-layer fabrication of micro-features appropriate for biomaterials applications. Further, scaffold architecture is implicated in the body's innate ability to isolate foreign substances making mitigation of this foreign body response (FBR) essential to ensuring the longevity of implanted biomaterials and devices. Bicontinuous interfacially jammed emulsion gels (bijels) offer a robust, self-assembly-based platform for synthesizing a new class of morphologically distinct biomaterials. Bijels form via kinetic arrest of temperature-driven spinodal decomposition in partially miscible binary liquid

systems. These non-equilibrium soft materials comprise co-continuous, fully percolating, non-constricting liquid domains separated by a nanoparticle monolayer. In this dissertation, fluid incompatibility in bijels is exploited to process biocompatible precursors to form hydrogel scaffolds displaying the morphological characteristics of the parent bijel template. Bijel-derived materials are first used to generate structurally unique, fibrin-loaded polyethylene glycol hydrogel composites to demonstrate a new, robust cell delivery system. Next, bijel-derived materials are investigated as tissue integrating implants with high vascularization and FBR mitigation potential stemming from their uniquely arranged pore morphology, presenting a new paradigm for designing long-lasting biomaterials.

CHAPTER 1. INTRODUCTION

1.1 MOTIVATION

The development of new materials that interact with natural biological systems (biomaterials) to regenerate damaged tissues and organs where donor tissues are scarce, provide long-lasting therapy, or aid in disease diagnostics is vital to improving quality of life and longevity while alleviating the immense burden of healthcare expenditures.[1] Over the last century, the field of biomaterials has evolved from “off the shelf” items that were considered bioinert; to bioactive materials that can interact with tissues, be resorbed, or release drugs; and finally, to tissue regenerative materials that can direct cell activity on the molecular level.[2] Biomaterials science is inherently a wide-ranging focus with no true “one-size-fits-all.” Like there are many different systems in the body that comprise distinctive chemical and physical properties, there are many different materials that have been explored and purposed as biomaterials. For instance, regarded as the first “modern-era” biomaterial (post-World War II), the first intraocular lens to correct blindness-inducing cataracts was simply a piece of dome-shaped plastic (polymethyl methacrylate, PMMA), the same material used in the cockpit of the British Submarine Spitfire airplane.[3] Plastic-based intraocular lenses are still widely used today, as are plastic knee and hip replacements, metal heart valves and bone fixation screws, silicone implants, collagen based skin replacements, and Teflon® catheters.[1,4] This list is meant to exemplify the range of bulk materials exploited as biomaterials throughout the years. Today’s tissue regenerative biomaterials integrate an array of naturally and/or synthetically derived components carefully devised to regrow wounded tissues,[5]

efficiently deliver cells or other therapeutics,[6] promote tissue infiltration,[7] and reduce the immune response to device materials.[8] The remainder of this introductory chapter will first introduce the basic concept of tissue engineering, highlighting the need for porous scaffolds and how nature inspires investigation of morphologically complex materials. Second, deterrence of the immune response to porous implanted biomaterials is introduced, and an unmet need for improving treatment of diabetes is emphasized. Lastly, a brief overview of the remaining topics covered in this dissertation is presented.

1.2 SCAFFOLDS FOR TISSUE ENGINEERING

The tissue engineering paradigm is presented in Figure 1 and follows these general steps: 1) harvesting of cells (for example, bone marrow-derived stem cells) from the patient or a suitable donor, 2) proliferation of cells in vitro, 3) seeding of cells in a porous scaffold, 4) incubation of the seeded scaffold in vitro for further proliferation and tissue organization, and 5) transplantation of the seeded scaffold to the patient at the site of tissue damage. Of great importance in this process is the porous scaffold which may be developed using various templating techniques,[9] layer-by-layer stereolithography,[10] direct writing,[11] or harvested directly from decellularized organs.[12] Scaffolds comprising interconnected porous architectures provide efficient transport of cell-supportive nutrients and avenues for cell proliferation, migration, and vascularization.[7] Of the various scaffold materials, hydrogels derived from synthetic and natural building blocks have found widespread utility in developing advanced, customizable biomaterials.[15] Briefly, hydrogels contain a cross-linked network of high water content building blocks and are attractive

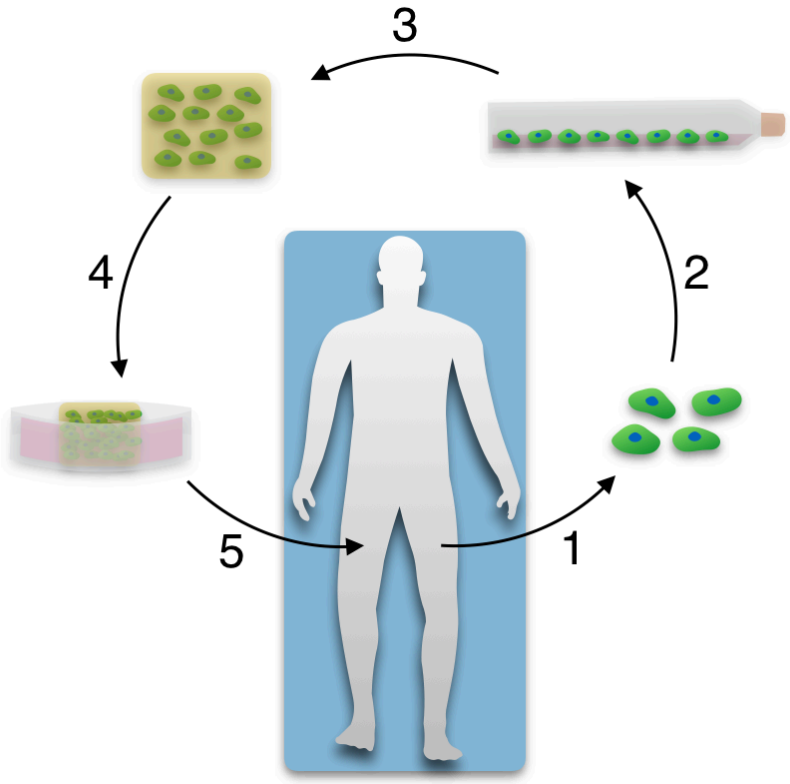

Figure 1. Schematic of the tissue engineering paradigm.

due to biocompatibility and tunable chemical, physical, and mechanical properties.[16] Further discussions on hydrogels and their application in therapeutic cell delivery and biocompatibility are included in Chapter 3 and Chapter 4 of this dissertation, respectively.

Porous tissue engineering scaffolds (Figure 1: Step 3) may exhibit a variety of microstructures with length scales that facilitate cell migration and proliferation. For example, a network of spherical pores connected via pore throats is the result of templating poly(hydroxyethyl methacrylate) (polyHEMA) hydrogels in either fused microparticles arrangements (Figure 2a)[17] or high internal phase emulsions (HIPEs) (Figure 2b).[18] These porous examples sustain cell viability and influence vascularization

of implants, however small pore throats impede cell migration[19] and limit mechanical integrity.[13]

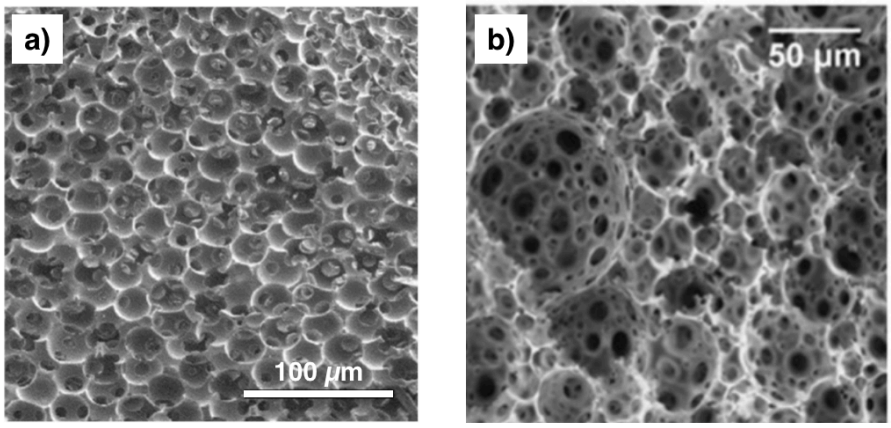

Figure 2. Examples of porous hydrogel scaffolds. a) Fused microparticles and b) high internal phase emulsions used to synthesize hydroxyethyl methacrylate and glycerol monomethacrylate scaffolds, respectively. *Journal of Materials Chemistry. B,* Materials for biology and medicine by Royal Society of Chemistry (Great Britain) Reproduced with permission of Royal Society of Chemistry in the format Thesis/Dissertation via Copyright Clearance Center.

Compared to randomly porous materials, mathematically-based minimal architectures such as the gyroid (Figure 3a) boast enhanced transport,[20] mechanical,[21] and high surface area for tissue growth.[22] Interestingly, similar anisotropic architectures are found in nature in marine organisms like the seastar, *Pisaster giganteus* (Figure 3b), explored as a bone tissue regeneration biomaterial.[23] The gyroid and other similarly designed structures can be assembled in layer-by-layer fashion, however, micrometer resolution requires lengthy fabrication steps.[24] Achieving these structures through scalable, robust techniques may have substantial impact on the availability and design of complex tissue engineering scaffolds.

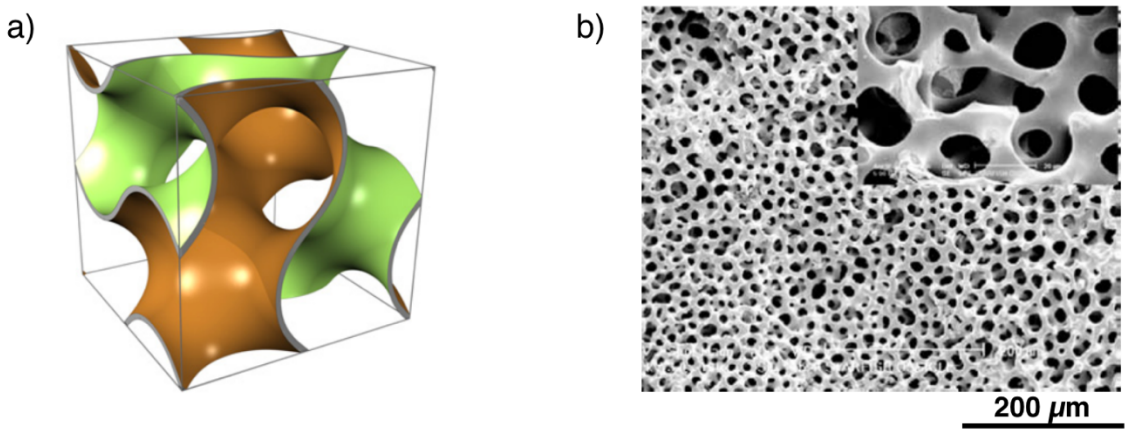

Figure 3. a) Gyroid minimal surface and b) minimal surface-like skeletal elements of the *Pisaster giganteus* seastar used in bone tissue engineering. a) Republished with permission of Pergamon, from Minimal surface scaffold designs for tissue engineering, Kapfer, *et al. 32* (29), 2011; permission conveyed through Copyright Clearance Center, Inc. b) Republished with permission of Pergamon, from Developing macroporous bicontinuous materials as scaffolds for tissue engineering, Martina, *et al. 26* (28), 2005; permission conveyed through Copyright Clearance Center, Inc.

1.3 IMMUNE RESPONSE TO IMPLANTED BIOMATERIALS

Revisiting the list of today's commonly employed bulk biomaterials in Section 1.1, the long-term viability of many implants is hampered by the body's inborn mechanism to protect itself from a foreign substance, or the foreign body response (FBR).[25] For example, high density polyethylene knee replacements loosen over time causing further wear to the joint,[26] while silicone breast implants undergo surface contraction and calcification during the FBR, interfering in early breast cancer tumor detection.[27] Moreover, tissue implants such as pancreatic beta cells encapsulated in hydrogels for the treatment of type 1 diabetes (T1D) are rendered useless by the FBR, prompting long-term pharmaceutical immune-suppression for such a treatment.[28] Upon implantation of a biomaterial, local tissue damage initiates early wound healing steps, and the fate of the

implant is contingent on the subsequent host-material interaction.[25,29] Prolonged inflammation at the implant site mark the foreign body response (FBR), which culminates in dense fibrotic tissue around the implant, deleterious to transplant tissue and functions of tissue-free devices such as catheters[30] and cochlear implants.[31] Hence, the alleviation of the FBR is essential for developing long-lasting diagnostic, therapeutic, and complex organ (liver, pancreas) replacement devices where tissue engineering routes are currently inadequate.

Interconnected porous biomaterials, as discussed in the previous section, promote tissue ingrowth and vascularization while reducing the FBR.[1] Take for instance the templating method used to synthesize the porous scaffold in Figure 2a. When compared to its non-porous analog (Figure 4a), there is nearly a four-fold reduction of fibrotic tissue (represented by the arrows in eosin stained collagen in histology sections), a result solely credited to the addition of the porous microstructure.[32] Furthermore, implant vascularization can be tuned with pore size (Figure 4b),[32] providing a strategy of interfacing porous scaffolds with existing biomaterials to aid in functional lifetime of implanted devices.[1]

We are actively engaging an unmet need for improved insulin infusion sets (IISs) that comprise a small cannula (often Teflon®) implanted under the skin to deliver insulin to diabetics during periods of high blood glucose (hyperglycemia).[33,34] IISs are tethered via soft tubing to a user-interfacing pump that calculates the amount of insulin required to maintain healthy blood sugar levels after meals.[4] IISs are recommended by their manufacturers to be worn for just 48 to 72 hours which can put frequent burden on

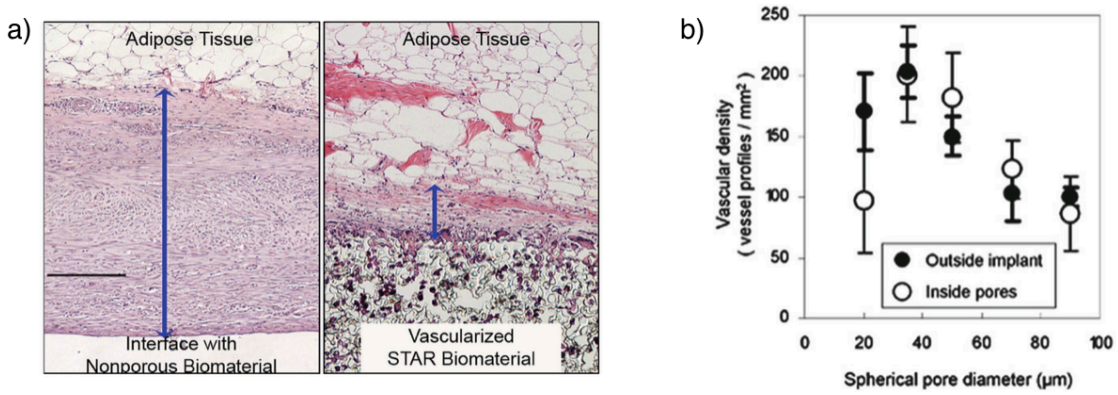

Figure 4. Tissue response to porous implants in skin. a) Histology sections from 6-week implantation in pigs, blue arrows represent fibrotic tissue stained with eosin, scale bar: 200 μm and b) vascular density as a function of pore size from 4-week implantation in mice. Vascularization "sweet spot" corresponding to equal vascular density inside and outside the porous implant when ~30 μm pores are used. Reprinted by permission from Copyright Clearance Center, Inc: Springer Nature*, Surgical Innovations in Glaucoma,* STARflo: A Suprachoroidal Drainage Implant Made from STAR® Biomaterial, Pourjavan, *et al.* 2014.

patients, especially children.[35–37] After implantation on an IIS cannula, prolonged inflammation gives rise to the FBR and development of fibrotic tissue around the distal end of the cannula thereby obstructing insulin flow and absorption. Unreliable insulin disruption puts the patient in grave danger as extremely high or low blood-sugar levels may lead to confusion, coma, or even death.[33,38] Considered the "Achilles Heel" of insulin pump treatment,[33] IISs are notoriously unreliability and as reported in 2015, account for some of the highest number of Food and Drug Administration recalls in the United States.[39] In Chapter 4, we investigate the beneficial tissue integration properties of a scalable minimal surface-like hydrogel. We hypothesize that if we interface current IIS cannula materials with our minimal surface-like hydrogels, then the functional wear-time for IISs can be dramatically increased from three days up to two weeks.

1.4 OVERVIEW OF THE DISSERTATION

The remainder of this dissertation is outlined as follows: In Chapter 2, I introduce a morphologically distinct class of soft matter - the bicontinuous interfacially jammed emulsion gel (bijel). I discuss the key components required for formation, provide examples of bijel systems and chief to the central theme of my research, I describe how bijels are processed into tailorable minimal surface-like porous structures particularly suited for biomaterials applications. Chapter 3 explores composite bijel-templated hydrogels (CBiTHs) comprising co-continuous hydrogel phases – a structure-supportive polyethylene glycol (PEG) phase and a cell-supportive fibrin phase – for therapeutic cell delivery. Chapter 4 investigates the tissue integration and FBR properties of bijel-templated PEG implants in mice and introduces a new paradigm to the design of long-lasting IIS cannulas. Lastly, core conclusions and a brief discussion of future work with biomaterials processed using bijels are summarized in Chapter 5.

CHAPTER 2. MORPHOLOGICALLY DISTINCT BIOMATERIALS PROCESSED USING BIJELS

2.1 BICONTINUOUS INTERFACIALLY JAMMED EMULSION GELS

2.1.1 INTRODUCTION

The research detailed in this dissertation engages a morphologically distinct class of soft material named the bicontinuous interfacially jammed emulsion gel (bijel). The bijel was first demonstrated in simulations by the Michael Cates group at the University of Edinburgh.[40] In this work, nanoparticles were introduced to a partially miscible binary fluid system to arrest spinodal decomposition phase separation (Figure 5).

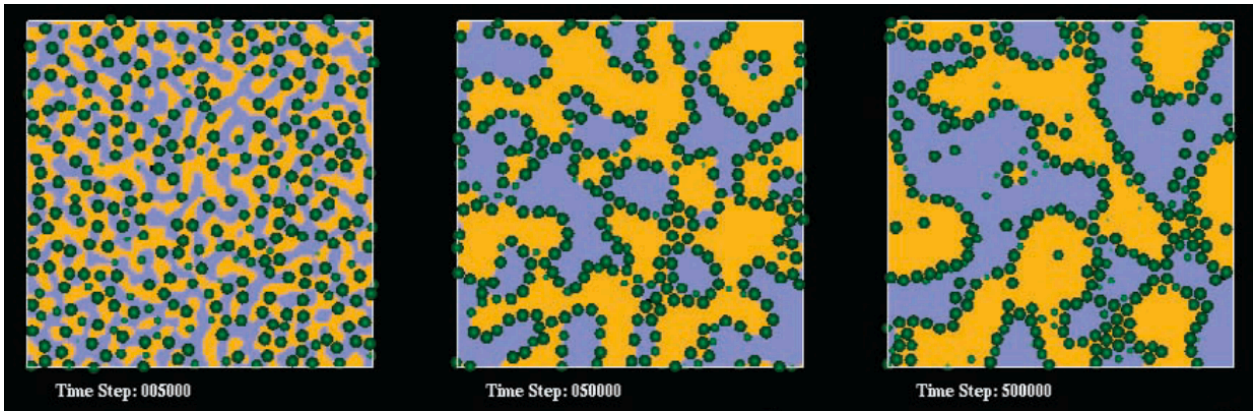

Figure 5. Formation simulation snapshots illustrating the early, middle, and late stage particle jamming of bijels, respectively. From *Science* **2005,** *309* (5744), 2198-2201. Reprinted with permission from AAAS.

Spinodal decomposition is a special case of phase separation where in contrast to small droplets nucleating and growing in one phase, there exists no energic barrier to widespread separation in either phase, and the fluids separate into fully bicontinuous fashion.[41] These bicontinuous phases self-assemble during the phase separation process, evolving in a dynamically self-similar manner in which the characteristic length

(or diameter of the channel-like phases) increases with time, but the morphology (surface curvature, pore size distribution) of the system is unchanged throughout.[42] In other words, the interface is coarsening in such a way that the percolating fluid phases have approximately the same average size. Spinodal decomposition is driven by minimization of interfacial area of the two fluids which ultimately bulk separates into stacked layers, in the presence of gravity, with the denser fluid on the bottom. The Cates group simulations demonstrated that if certain nanoparticles were introduced to a system undergoing spinodal decomposition, they would spontaneously adsorb at the liquid-liquid interface to aid in the minimization of the interfacial area and eventually jam (or arrest) the interface once completely occupied by particles, forming the bijel. The following sections expand on the general concepts of the bijel.

2.1.1.1 MISCIBILITY

The description of bijels above touches on many concepts key to bijel formation. First is the partially miscible binary fluid system. Simply speaking, two fluids are selected which are miscible at certain temperatures and immiscible at other temperatures. As the bijel is formed by arresting fluids that are phase separating, the fluids must begin in a miscible state and transition to an immiscible state. While there are other stimuli for this transition (e.g. pressure), I will focus on changes in temperature for this dissertation. Additionally, I will use the term “temperature quench” to denote this transition from the miscible to immiscible state, regardless of the direction of the temperature change. One example of such a system is water and 2,6-lutidine (W/L). From the experimentally

derived coexistence curve shown in Figure 6, W/L are miscible at compositions and temperatures below the curve, and immiscible above the curve, separating into a water-rich phase (Figure 6 “A”) and a lutidine-rich phase (Figure 6 “B”).[43] Of note, these phases are not pure, hence the “-rich” label and the “C_A, C_B” labels in Figure 6, representing the concentration of lutidine in the respective phase.

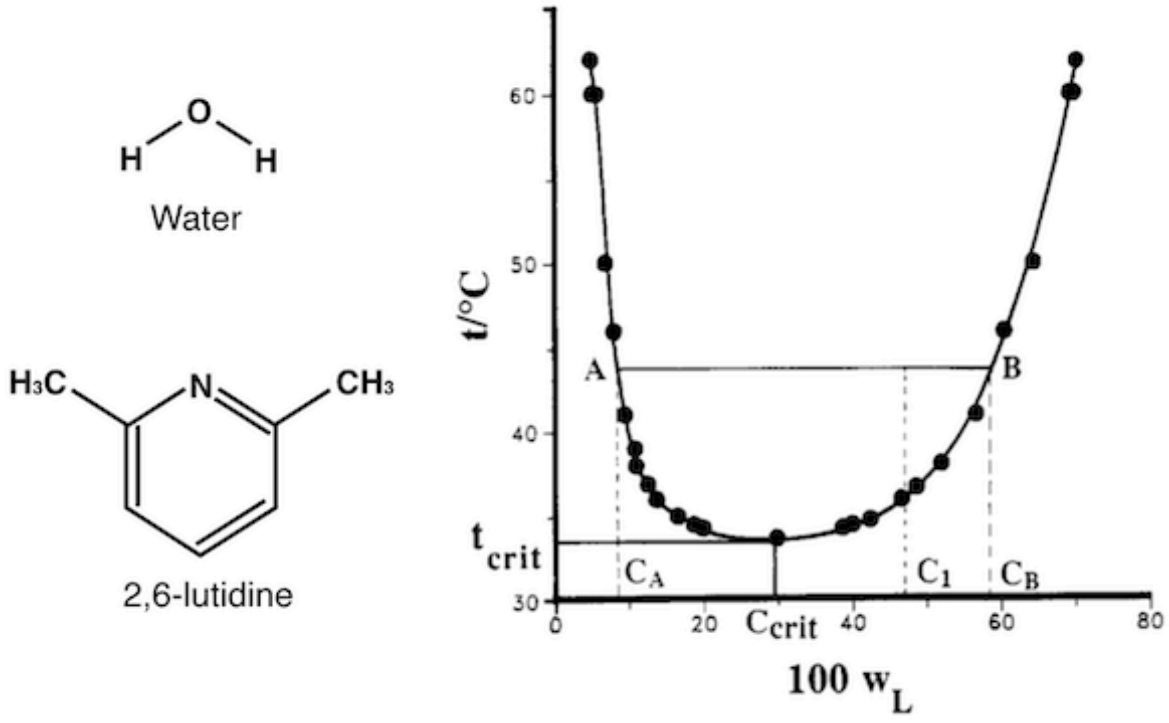

Figure 6. Coexistence curve for water and 2,6-lutidine. Republished with permission from *Journal of Chemical and Engineering Data* **1993,** *38* (4), 516-519. Copyright 1993 American Chemical Society.

2.1.1.2 SPINODAL DECOMPOSITION

The next key topic is the arresting of fluids undergoing *spinodal decomposition.* From the thermodynamics standpoint, spinodal decomposition occurs when there is no energic barrier to phase separation.[44] In the spinodal state, $\partial^2 \Delta G^{mix}/\partial x^2 < 0$, meaning that the fluid system cannot remain stable to even small perturbations in composition

resulting in spontaneous separation of the fluids throughout the entire volume.[45] Referring back to Figure 6, spinodal decomposition occurs in W/L when the fluids are mixed at the critical composition ("C_{crit}") and quenched above the lower critical solution temperature ("t_{crit}"). For W/L, the C_{crit} and t_{crit} (herein denoted as "C_c" and "T_c") are 28% lutidine by mass fraction (0.064 lutidine by mole fraction, x_L) and 34.1°C, respectively.[43] The two fluids separate in a manner driven solely by minimizing their interfacial area, splitting into fully percolating bicontinuous tube-like phases that grow in diameter until bulk separation occurs. Importantly, the evolution of spinodal decomposition is said to be "self-similar"[46] as although the diameters of the phases are growing, they are growing in a similar fashion throughout the volume. Through this mechanism, the fluid-fluid interfacial area is minimized resulting in a spinodal interface, where nearly every point on the interface has equal and opposite principal curvatures (k_1 *and* k_2), signatures of a mathematical hyperbolic or "saddle" point.[47] A three-dimensional (3D) rendering of fluids undergoing spinodal decomposition and a spinodal surface are depicted in Figure 7 having negative Gaussian curvature, *K,* and zero mean curvature, H. For this particular example, the blue colored phase represents the water-rich phase, while the transparent phase (everything that is not blue) represents the 2,6-lutidine-rich phase. The 3D rendering also exemplifies the bicontinuity of the fluid phases and the self-similar nature of their morphology.

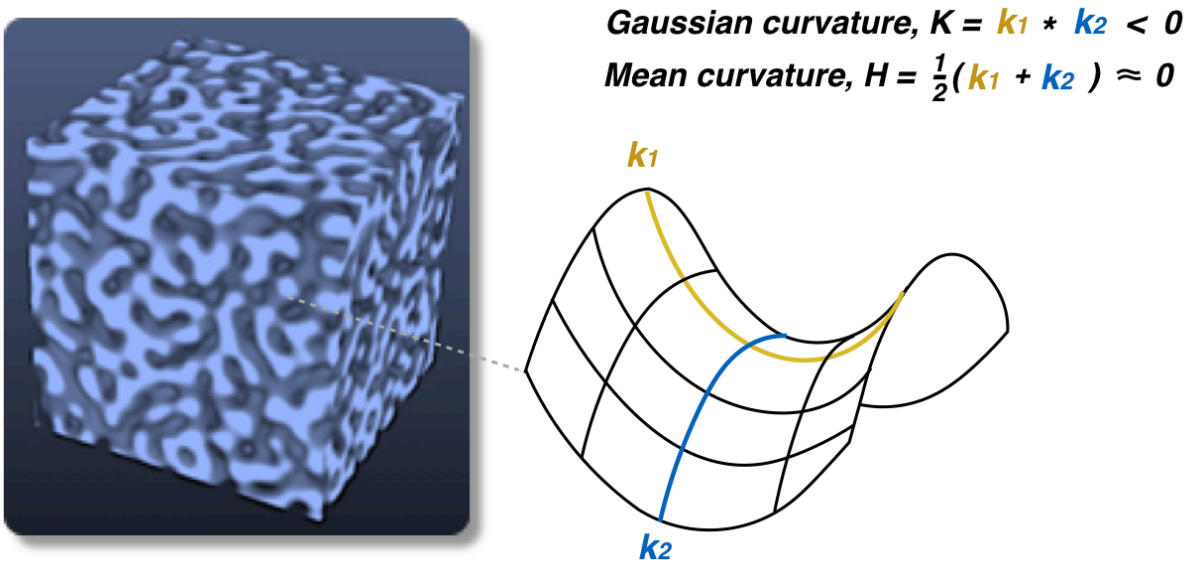

Figure 7. 3D rendering of W/L system undergoing spinodal decomposition and the corresponding interfacial curvature features.

2.1.1.3 PARTICLES

Required for the formation of bijels, colloidal particles are added to the binary fluid system and are responsible for arresting spinodal decomposition.[40] The colloidal designation used here indicates that particles are generally between 1 nm and 1 μm in diameter.[48] For the remainder of this dissertation, I refer to these colloidal particles simply as "nanoparticles." Nanoparticles have been used to stabilize immiscible solvents as emulsions (e.g. water stabilized in bulk oil or vice versa) dating back more than a century,[49] finding application as pharmaceutical creams[50] and food products,[51] to name a few.

Nanoparticle surface chemistry dictates the interaction with fluids, herein termed the "wettability." In a binary fluid system, the three-phase contact angle, θ, calculated from the force balance of interfacial tensions in the system, is used to quantify this wettability

were by convention the angle is measured through the polar phase.[52] Figure 8 illustrates how nanoparticles position on the W/L interface as they prefer the water with $\theta < 90°$, prefer both liquids equally with $\theta = 90°$, and prefer the 2,6-lutidine with $\theta > 90°$. Nanoparticles with $\theta \approx 90°$ are described as near-neutrally wetting, and are required for bijel formation where under this condition, the nanoparticles to not impose curvature to the W/L interface.[53] During bijel formation, the nanoparticles are initially well-dispersed in the miscible W/L phase, then are either swept up by or diffuse via Brownian motion to the coarsening interface until completely occupying the interface, thereby arresting the phase separation.[54] The energy required to dislodge a nanoparticle from the W/L interface is several orders of magnitude greater than the thermal energy, *k*T.[55]

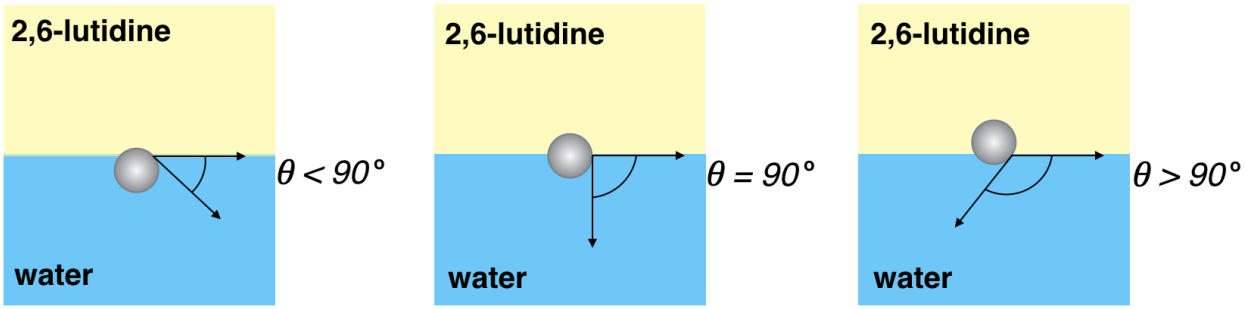

Figure 8. Three-phase contact angle for nanoparticles of varying W/L surface wettability.

2.1.1.4 TUNABLE BIJEL DOMAIN SIZE

As bijel formation is a result of kinetic jamming of spinodal decomposition using nanoparticles, the characteristic fluid domain size, ξ, is dependent on the nanoparticle diameter, d, and the particle volume fraction, ϕ.[54] Equation 1 is used to calculate the domain size where the particle-laden bijel interface exists as a close-packed monolayer and experimentally inversely proportional to volume fractions between 0.01 and 0.04.[54]

$$\xi = \left(\frac{\pi}{\sqrt{3}}\right)\left(\frac{d}{\phi}\right) \quad (1)$$

2.1.2 EXPERIMENTALLY REALIZED BIJELS

While the Cates group showed that near-neutrally wetting particles could indeed arrest spinodal decomposition and theoretically form the bijel, successful bijel formation was realized experimentally two years later by the Paul Clegg group, also at the University of Edinburgh.[54] In the experiments, fluorescently-labeled silicon dioxide (silica) nanoparticles were dispersed in water and 2,6-lutidine at the critical composition (x_{Lut} = 0.064) and quenched to 40°C (above T_c = 34.1°C). Recall from the previous section and Figure 6 that this process will result in spinodal decomposition of W/L. Fluorescein isothiocyanate (FITC) was covalently bonded to the silica particles for direct visualization of bijel formation using laser scanning confocal microscopy, a technique which scans a laser across a region of interest to excite the fluorescent FITC molecules and collects emitted light for each scanned position to construct an image. Key to confocal microscopy is the use of a pinhole aperture that blocks out-of-focus emitted light to acquire high-resolution images of only select focal planes.[56] A cartoon schematic with the corresponding confocal image during bijel formation is illustrated in Figure 9.[54] Silica nanoparticles are dispersed in the W/L system at room temperature (Figure 9a), the sample is quenched to 40°C prompting spinodal decomposition and the adsorption of nanoparticles to the sweeping W/L interface (Figure 9b),

and jamming occurs when the W/L interface is replaced entirely by nanoparticles, forming the bijel (Figure 9c). As described in the previous section, the silica nanoparticles used to form bijels must have near-neutrally wetting surface chemistry. If the particles prefer one phase (take for instance a preference towards the water-rich phase, $\theta < 90°$), they do not arrange evenly on the spinodal interface, disrupting interfacial jamming. Careful adjustments to nanoparticle surface chemistry are paramount to bijel formation. Like the first experimental bijel, the research in this dissertation uses fluorescently-labeled silica with surface chemistry tuning achieved through drying adsorbed surface water in a vacuum oven.

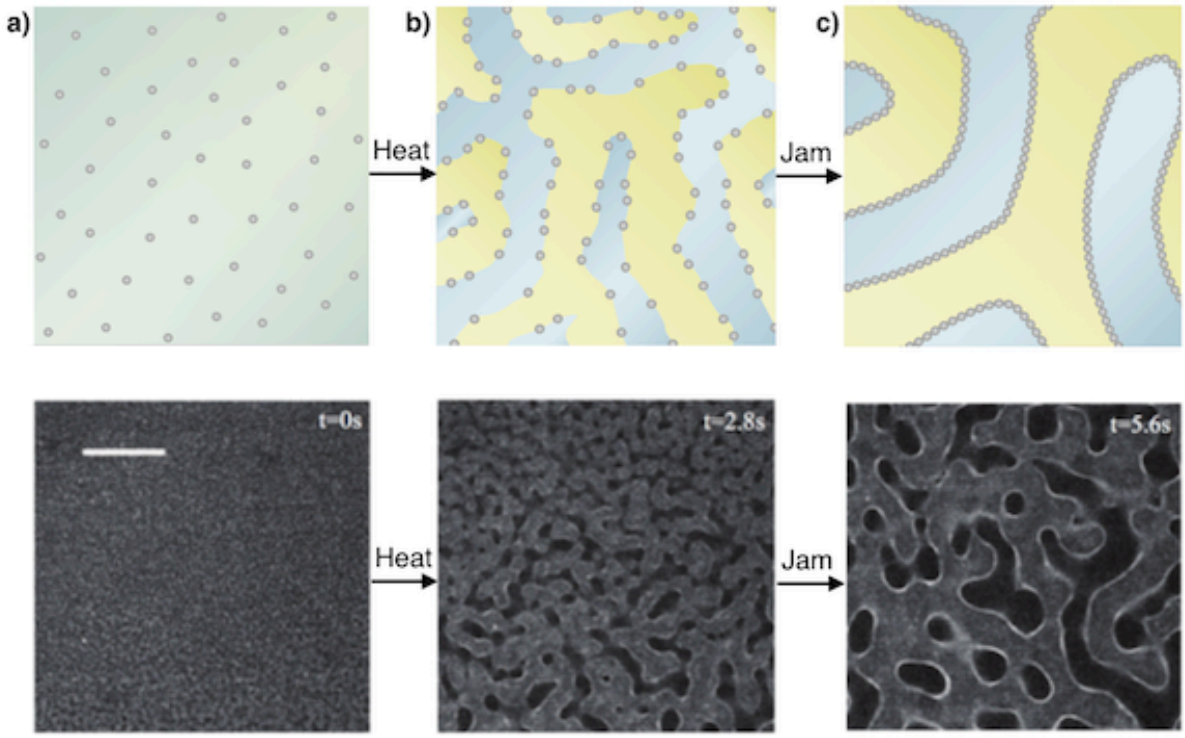

Figure 9. Cartoon and corresponding confocal images of bijel formation. Scale bar, 100 μm. Republished with permission of Nature Publishing Group, from Bicontinuous emulsions stabilized solely by colloidal particles, Herzig *et al. 6* (12), **2007**; permission conveyed through Copyright Clearance Center, Inc.

Since the innovation of the silica-stabilized W/L bijel a decade ago, many features of the bijel and additional nanoparticle chemistries and binary fluid systems have been explored. The following are selected examples of these explored systems. Herzig *et al*. showed that W/L bijels remain stable up to seven months when stored above the Tc and behave as a "semi-solid," able to withstand small loads through interface deformation and particle rearrangement.[54] Reeves *et al*. quantitatively analyzed the curvature features of the particle-laden bijel interface as a function of particle size, showing that smaller particles result in curvature features more representative of a spinodal-like interface (i.e. negative Gaussian and zero mean curvatures).[57] Clegg *et al*. used a silica modifier (or silanizing agent) to tune surface wettability to stabilize an ethanol/dodecane fluid system.[55] Huang *et al*. used carboxylated silica and polystyrene nanoparticles along with a polymer surfactant (i.e. surface active agent common to water/oil stabilization)[58] to form water/toluene and water/decane bijels through mixing, rather than a temperature quench.[53] Haase *et al.* introduced a water/diethylphthalate bijel using surfactant-modified silica and a solvent in which fluid composition acts as the stimulus for spinodal decomposition, rather than a temperature quench.[59] Additionally, the fluid composition stimulus technique has been used with water/hexanediol diacrylate and surfactant that can be polymerized to form bijel-based fibers with relevance in separations applications.[60,61] A list of bijel liquid systems that includes additional examples is presented in Table 1.

Of particular importance to the research performed in this dissertation is the study of bijel rheology performed by Lee *et al.* in the UCI Colloid Science Laboratory.[62] In this

work, two bijel systems – W/L and nitromethane/ethylene glycol (NM/EG) bijels – were analyzed via parallel plate rheometry. Bijels were formed on a rheometer (MCR 301, Anton-Paar) and subjected to constant oscillation (strain: 0.1%, frequency: 1 Hz) to characterize the viscoelastic properties of the selected bijels. The time-evolved elastic storage (G') and loss (G'') moduli of the W/L and NM/EG bijels for various temperature

Table 1. Liquid Systems for Bijels

Fluid 1	**Fluid 2**
Water	2,6-Lutidine[54]
Ethanol	Dodecane[55]
Nitromethane	Ethylene Glycol[62]
Water	Succinonitrile[63]
Water (gelatin rich)	Water (starch rich)[64]
Water	Toluene[53]
Water	Decane[53]
Nitromethane	Propylene Glycol
Nitromethane	Ethanediol[65]
Water	Isobutyric Acid[66]
Water	Diethylphthalate[59]
Water	Hexanediol Diacrylate[60,61]
Ethylene Carbonate	*p*-Xylene[67]
Styrene Trimer	Polybutene[68]
Nitroethane	Propylene Glycol
Propylene Carbonate	Di-n-octyl phthalate
Propylene Carbonate	Ethyl Decanoate
Butanediol	Propylene Carbonate
Butanediol	Polyethylene Glycol Diacrylate

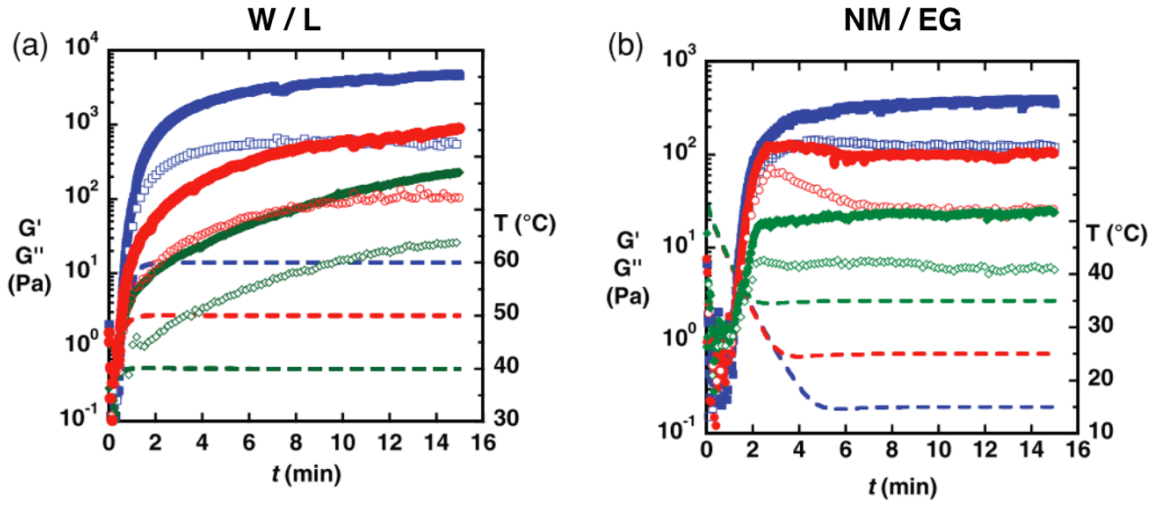

Figure 10. Storage (G') and Loss (G'') of measured with parallel place rheometry for W/L (a) and NM/EG (b) bijels. Reprinted with permission from *Advanced Functional Materials,* **2013,** *23* (4), 417-423. Copyright 2013 John Wiley and Sons.

quenches are shown in Figure 10; note the NM/EG has an inverted coexistence curve (i.e. quenched by cooling the fluids), having a T_c of 40°C.[62] Gelation is marked by G' > G'' which occurs within a couple minutes in both systems. Importantly, G' in W/L bijels is approximately an order of magnitude greater in than in NM/EG bijels. G' increases with deeper temperature quenches in both systems and continues to increase with time for W/L bijels. This increase is attributed to Van der Waals attractions between the silica nanoparticles experienced in the W/L bijels, forming a "monogel." Conversely, G' measurements levels off early in NM/EG. Incredibly, the monogel stays in tact after the interfacial tension between the two fluid phases is removed (the temperature is brought back to the miscible region on the coexistence curve). This behavior is illustrated in Figure 11 using a time series of confocal microscopy images shows the NM/EG bijel completely remixing, while the nanoparticle monogel formed in the W/L bijel persists, even after the

fluids remix.[62] The heightened elastic storage modulus in W/L bijels offers a robust fluid template for creating porous materials. The following section details the inception of bijel processing, examples of previously processed materials, and how I have used bijel processing to develop a new class of biomaterial with the distinct morphological features inherent to bijels.

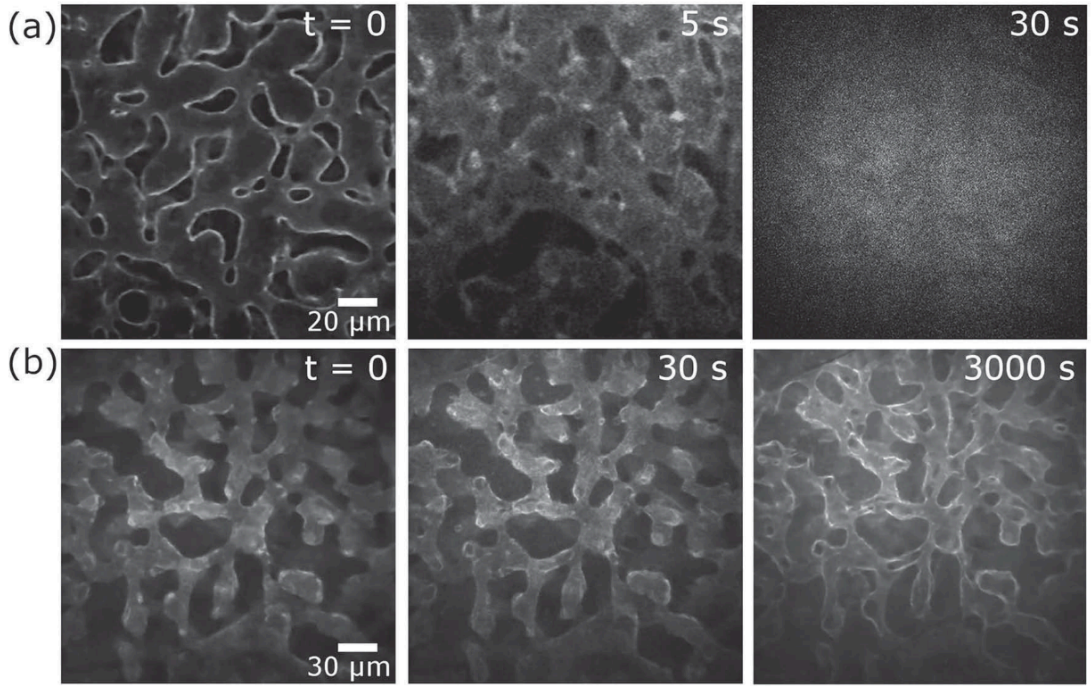

Figure 11. Time series of fluorescence confocal microscopy images showing the behavior of a) NM/EG bijels and b) W/L bijels as the liquids remix. Reprinted with permission from *Advanced Functional Materials,* **2013,** *23* (4), 417-423. Copyright 2013 John Wiley and Sons.

2.2 BIJEL PROCESSSING

2.2.1 INTRODUCTION

As described in the previous section, bijels self-assemble into kinetically stable soft materials comprising fully percolating, bicontinuous fluid phases separated by a near minimal surface monolayer of colloidal particles. The fundamental morphology of bijels is

of great attraction for numerous material applications; in the initial bijel simulation study by the Cates group, the bijel is proposed as a cross-flow reactor boasting high permeability and high interfacial area.[40] Mathematically defined minimal surfaces have been studied for decades for materials that optimize transport and mechanical properties.[69,70] For instance, the fully bicontinuous phases separated by the Schoen's Gyroid minimal surface has demonstrated excellent thermal and electrical conductivity.[20] More recently, Qin *et al.* have shown significant compressive properties in graphene materials derived from the Schoen G minimal surface.[21] This surface has also been explored as a tissue engineering scaffold with enhanced transport properties for diffusion of nutrients and waste for growing tissues.[24] These surfaces can be formed using additive manufacturing techniques such as multi-photon photolithography, however, this method is limited by slow processing for finely resolved surfaces, thereby limiting scale-up for industrial implementation.[24,71] Hence, materials derived from a self-assembly process with near-minimal surface morphological characteristics – the bijel – are attractive alternatives. Previous simulation work shows that signatures of minimal surfaces (i.e. negative Gaussian and zero mean curvature) are present in during the self-similar spinodal decomposition process.[42,72,73] Additional simulation work by Frijters and Harting calculated increased hydraulic permeability through bijels as compared to a randomly porous material.[74] This section describes how bijels can be experimentally processed into morphologically unique porous media that I have harnessed to create a new class of biomaterials.

2.2.2 USING THE BIJEL TO TEMPLATE POROUS MATERIALS

Although the bijel is kinetically stable, the bicontinuous fluid phases are thermodynamically incompatible, hence phase separation. This thermodynamic incompatibility was specifically exploited by Lee and Mohraz in 2010,[75] pioneering a bijel processing route that allows formation of free-standing, 3D materials that possess the distinctive morphological features inherent to bijels. This bijel processing technique introduced a robust method for locking in the bijel microstructure for processing into a unique class of porous materials with great potential in (but not limited to) energy systems, catalysis, and human health applications.

Bijel processing into 3D porous materials is performed by first forming a bijel using a critical solution of water and 2,6-lutidine (x_L = 0.064), quenched above the T_c (34.1°C) using electromagnetic radiation (μ-waves), and carefully maintained in an oven above the T_c (i.e. in the spinodal region of the coexistence curve, Figure 6). Next, a polymer pre-cursor (e.g. monomer or oligomer) with selective solubility is added gently to the top of the W/L bijel and allowed to transport by gravity and diffusion throughout the continuous fluid phase of the bijel. The typical transport time for a bijel with a total volume ~200 μL is four hours. For a more detailed demonstration, consider a W/L bijel formed in a glass cylinder (Figure 12a). A solution of polyethylene glycol diacrylate (PEGDA) and photoinitiator (Darocur® 1173) is pipetted onto the bijel and begins to partition into the 2,6-lutidine-rich bijel phase (Figure 12b, “M”). The bijel is maintained above the T_c for at least four hours to allow complete transport of the PEGDA and photoinitiator throughout the phase volume (Figure 12c). Lastly, excess volume is pipetted from the top of the bijel,

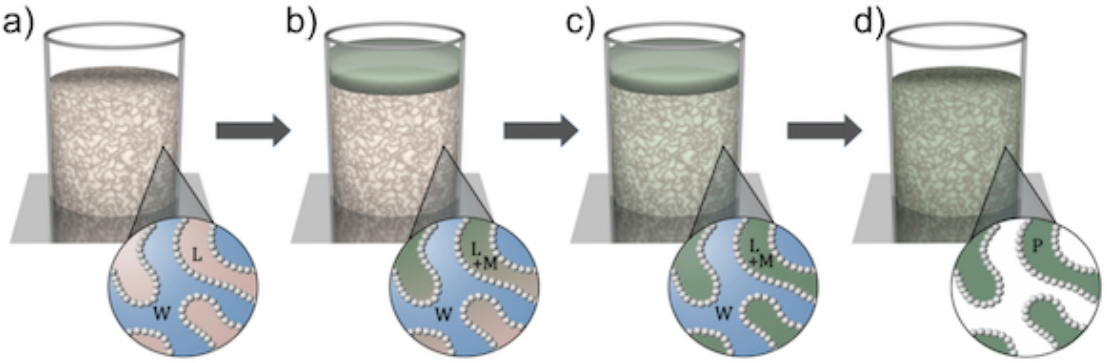

Figure 12. Bijel processing for forming 3D porous scaffold materials. Reprinted with permission from *Advanced Functional Materials,* **2013,** *23* (4), 417-423. Copyright 2013 John Wiley and Sons.

and ultraviolet (UV) light is used to cross-link the PEGDA phase, thereby forming a stiff polymer gel, locking in the parent bijel morphology. Remaining fluids are removed from the cross-linked material, completing the processing of the bijel into a 3D microporous polymer scaffold (Figure 12d). In its initial demonstration in the literature,[75] confocal microscopy images of the W/L particle-laden bijel interface before (Figure 13a) and after (Figure 13b) processing reveal that the microstructure is directly locked in following polymerization, embedding the fluorescently-labeled silica in the newly formed scaffold. Scanning electron microscopy (SEM) micrographs also reveal the bulk microstructure (Figure 13c) and particle-embedded surface (Figure 13d) of the newly formed material. The silica particles may be removed by etching in hydrofluoric acid or high molarity sodium hydroxide.

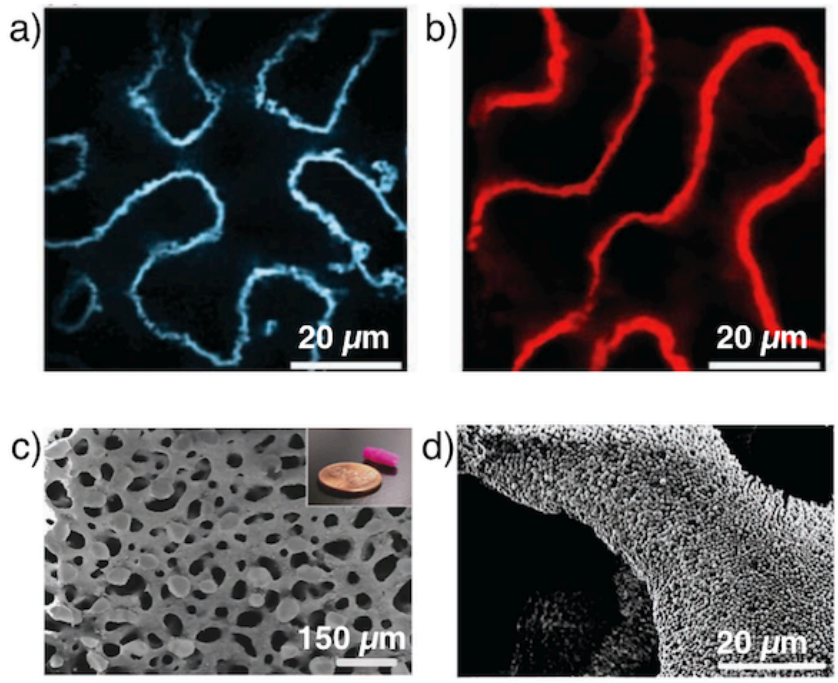

Figure 13. Demonstration of a porous material processed using bijels. Confocal microscopy images of the particle-laden W/L bijel interface before a) and after b) polymerization. SEM micrographs of the porous material exhibiting the bulk morphology c) and particle-embedded material surface. Reprinted with permission from *Advanced Materials* **2010,** *22* (43), 4836-4841. Copyright 2010 John Wiley and Sons.

The bijel processing technique uses a common UV-initiated, radical chain growth polymerization mechanism within one of the bijel phases.[76] Following the steps illustrated in Figure 14, initiation is achieved using UV light and splits the Darocur® 1173 photoinitiator (I) into two fragments, each containing a free radical (·). Other initiation mechanisms exist (e.g. thermal initiation) but for the experiments discussed throughout this dissertation, all initiation is performed using UV light. An initiator fragment encounters a monomer (M) and associates with the monomer forming a covalent bond with the alkene of an acrylate functional group, thereby transferring the free radical to the monomer species. In this example, the monomer is PEGDA. The radical then propagates to another

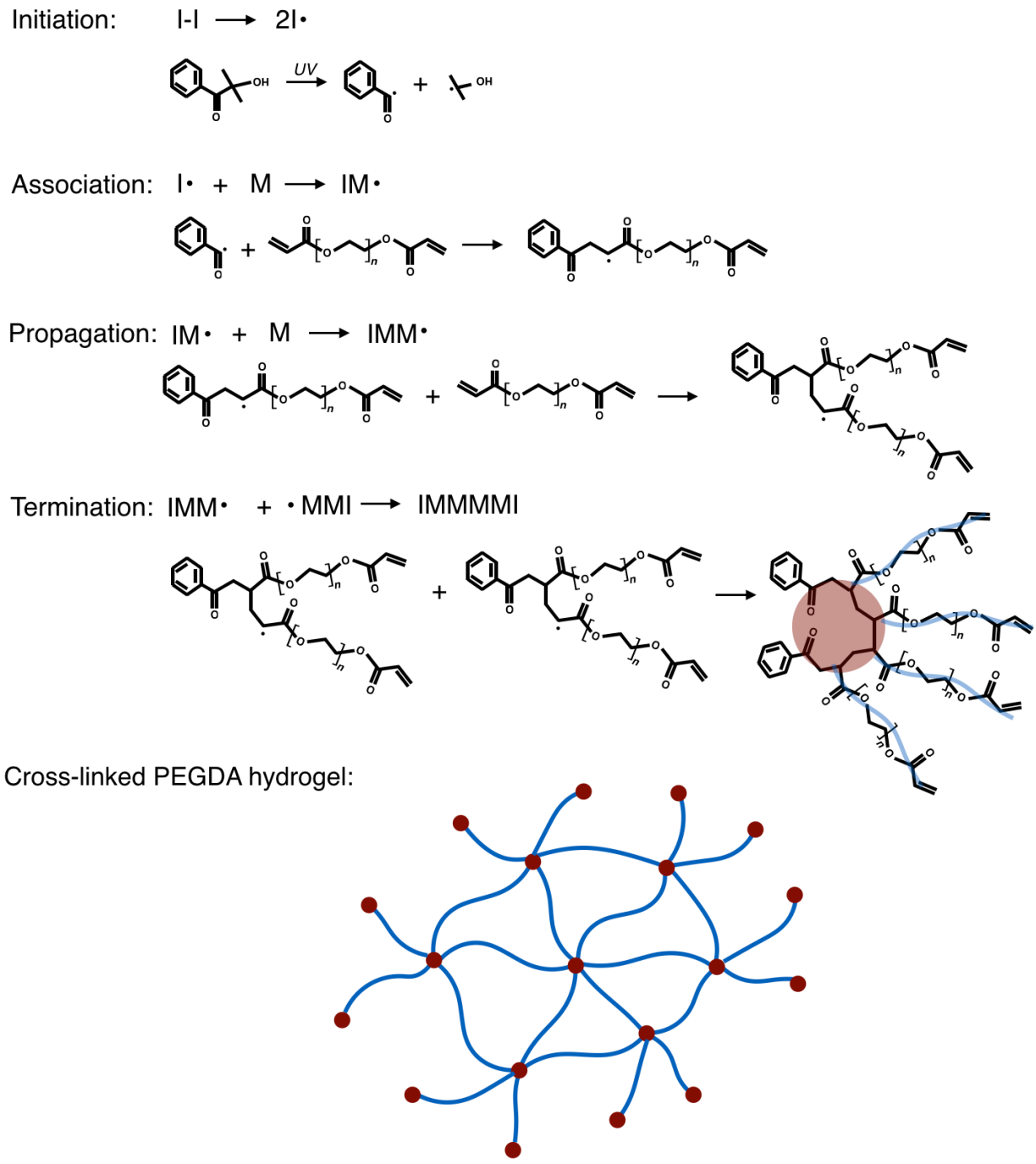

Figure 14. Radical photopolymerization of PEGDA hydrogel.

PEGDA molecule growing the polymer chain by one monomer. The propagation step can continue, forming a long polymer chain until encountering another free radical species, terminating polymerization. For this simplified example, consider two propagating PEGDA polymers each with two monomer groups that come into contact, terminating the chain growth polymerization with four total monomer groups. Using a red circle to denote the cite of chain growth, and blue lines to denote the monomer, a simplified version of a cross-linked PEGDA hydrogel is drawn in which all acrylates are undergoing the described polymerization steps (red circles are bonding together to link the blue lines). For simplicity in this example, PEGDA is considered a monomer meaning there is only ethylene glycol unit, but PEGDA is actually an "oligomer," meaning it is already a polymer consisting of a small number of ethylene glycol repeat units. Additionally, radical chain growth is not limited to acrylate functional groups; other common radical chain growth functional groups include acrylamides and vinyls.[76] The bijel processing technique allows materials to be formed with a variety of chemistries, with the caveat of selective solubility in either the water-rich or 2,6-lutidine-rich phase. A list of monomers and oligomers (herein referred to as "polymer precursors") that have been used to process bijels into porous polymer scaffolds is presented in Table 2.

Table 2. Polymer Precursors used in Bijel Processing

Polymer Precursor
Polyethylene glycol diacrylate (PEGDA)[77,78]
1,6-Hexanediol diacrylate (HDDA)[60,75,79]
Ethoxylated trimethylolpropane triacrylate (3 arm PEG)[62,80]
Dipentaerythritol pentaacrylate (5 arm PEG)[75]
Tri(propylene glycol) diacrylate
Trimethylolpropane triacrylate
Hydroxyethyl methacrylate (HEMA)-*co*-acrylic acid
2-Phenoxyethyl acrylate
Propoxylated glyceryl triacrylate
Ethoxylated bisphenol A diacrylate
Gelatin Methacrylate
Sulfobetaine methacrylate
N-isopropylacrylamide
Acrylamide

Digital images of example bijel-derived porous polythethylene glycol (PEG)-based hydrogels, PEGDA, ethoxylated trimethylolpropane triacrylate (herein referred to as "PEGTA"), and dipentaerythritol pentaacrylate are shown in Figure 15. These example materials were processed using the method described above, using rhodamine B isothiocyanate (RITC)-labeled silica to form the W/L bijel template, hence the pink color. By altering the PEG-based material and the pore size, simply through adding a different precursor solution to the bijel and changing the particle loading volume, mechanical properties such as the compressive modulus of bijel-processed materials can be tuned. Table 3 exemplifies this robust aspect of bijel processing as the compressive modulus is increased by either decreasing the pore size in the same material (PEGDA) or changing material (PEGDA versus PEGTA).

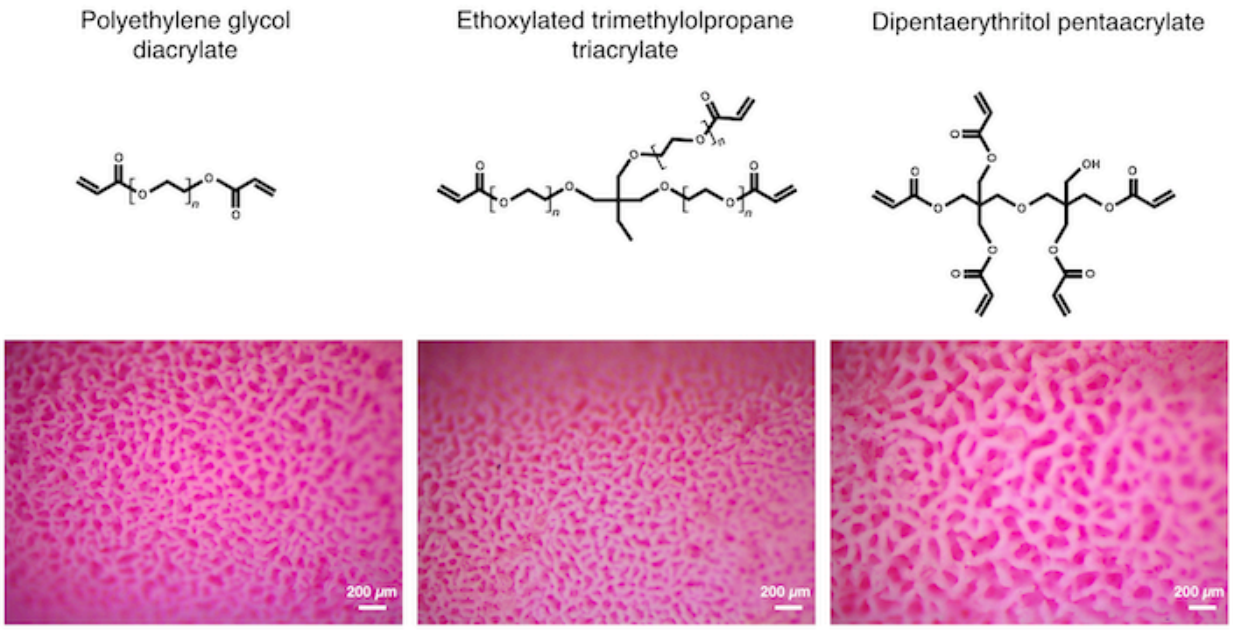

Figure 15. Multi-acrylated PEG polymers processed using bijels

Table 3. Compressive moduli of example PEG-based materials processed using bijels

Template Material	Pore size (μm)	Compressive Modulus, *E* (kPa)
PEGDA	28	795.70 ± 5.59%
PEGDA	32	591.57 ± 9.17%
PEGDTA	32	822.23 ± 10.20%

2.2.3 USING BIJEL PROCESSING TO CREATE BIOMATERIALS

To date, the most robust bijel system for processing is W/L due to the enhanced viscoelastic behavior and irreversible monogel formation, discussed in the previous section. Since the inception of W/L bijel processing, porous ceramics,[75] gold[77] and silver[80] monoliths, and electrode materials[79] have been developed. Witt *et al.* used W/L bijel processing of 1,6-Hexanediol diacrylate (HDDA) to construct high energy, high power 3D electrodes using that outperform similar type materials derived from graphene sheets,[81] graphite foams,[82] and carbon nanotubes[83] through unique, co-continuous microstructure and tunability of pore size and active layer thickness.[79]

PEG-based materials, already discussed previously for processing, have long been investigated as biomaterials that limit protein adsorption to decrease the inflammatory response.[84] Additionally, the process of "PEGylation" is common in drug delivery as adding PEG to a therapeutic does not get recognized by the immune system.[85] In chapters 3 and 4 below, I expand on the attractive details of PEG and use PEG-based scaffolds processed using bijels to introduce a new class of biomaterial. For this section,

two additional materials with potential as biomaterials processed using bijels are detailed: gelatin methacrylate (gelMA) and sulfobetaine methacrylate (SBMA).

2.2.3.1 GELATIN METHACRYLATE

Gelatin is a polypeptide derived from collagen, a prominent protein found in the extracellular matrix (ECM) in skin, bone, and connective tissues throughout the body.[86] Amine groups present in lysine amino acids can be modified through methacrylation (i.e. adding methacrylate functional groups) which allows formation of cross-linked gels through UV-initiated polymerization.[87] The percentage of methacrylated amine groups permits tunable degradation by naturally occurring matrix metalloproteinase (MMP) enzymes such as collagenase (MMP-1), making gelatin-based materials attractive as implantable, biodegradable regenerative tissue scaffolds[88] (Figure 16a, photoinitiator: Irgacure® 2959). Gelatin methacrylate (gelMA) hydrogel scaffolds were successfully processed using W/L bijels stabilized by FITC-labeled silica, imaged via confocal microscopy (Figure 16b). Biodegradability was demonstrated by soaking a disk of bijel-dervied gelMA in 0.5 mg/mL collagenase (Sigma-Aldrich), confirming the synthesis of the first biodegradable, bijel-derived material.

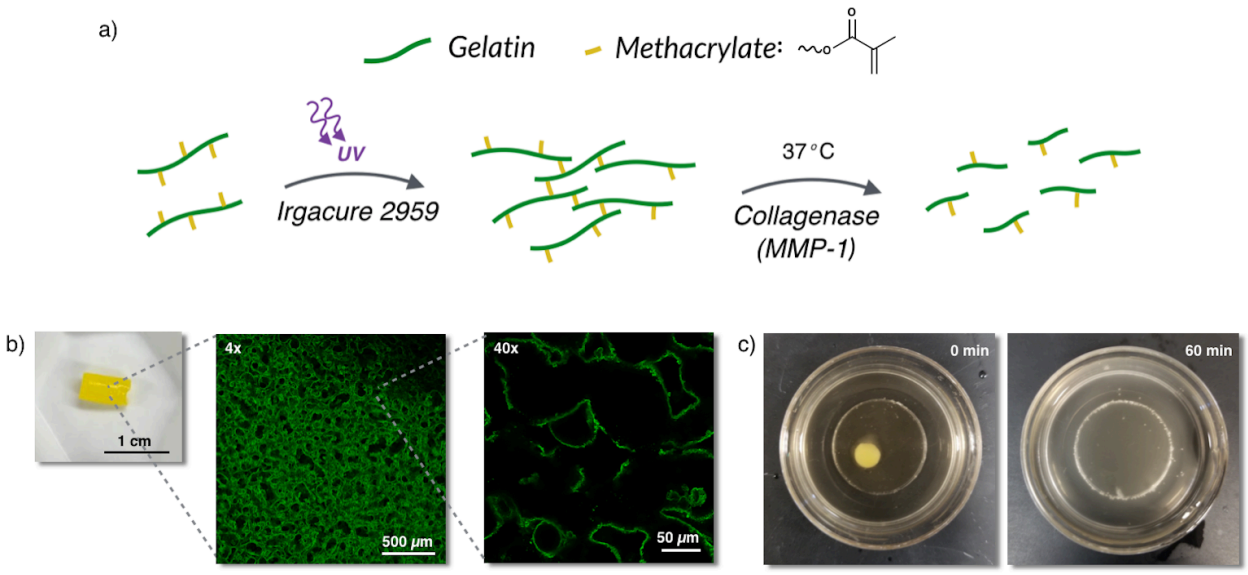

Figure 16. Gelatin methacrylate (gelMA) scaffolds processed using W/L bijels. a) Schematic of gelatin methacrylate cross-linking and enzymatic degradation using collagenase, b) gelMA scaffolds images using confocal microsopy under 4x and 40x magnification and c) degradation of gelMA scaffold demonstrated in collagenase solution with complete degradation achieved after 60 min.

2.2.3.2 SULFOBETAINE METHACRYLATE

One subtype of hydrogels that has attracted significant interest as a non-fouling biomaterial is the zwitterionic hydrogel, named for their balanced cation/anion ratio.[89] These materials tightly bind water molecules through electrostatics, rather than weaker hydrogen bonds as is the case in most hydrogels, giving rise to a stronger repulsion of molecules attempting to disrupt the hydrogel-water complex, namely proteins. Sulfobetaine methacrylate (SBMA) is one such material that has demonstrated this non-fouling behavior.[31,90] To demonstrate our ability to synthesize SBMA hydrogels from bijels, an aqueous solution of SBMA (20% w/v), N'N-methylenebisacrylamide (15% w/w relative to SBMA), and Irgacure® 2959 (2% w/w relative to SBMA) were pipetted on W/L

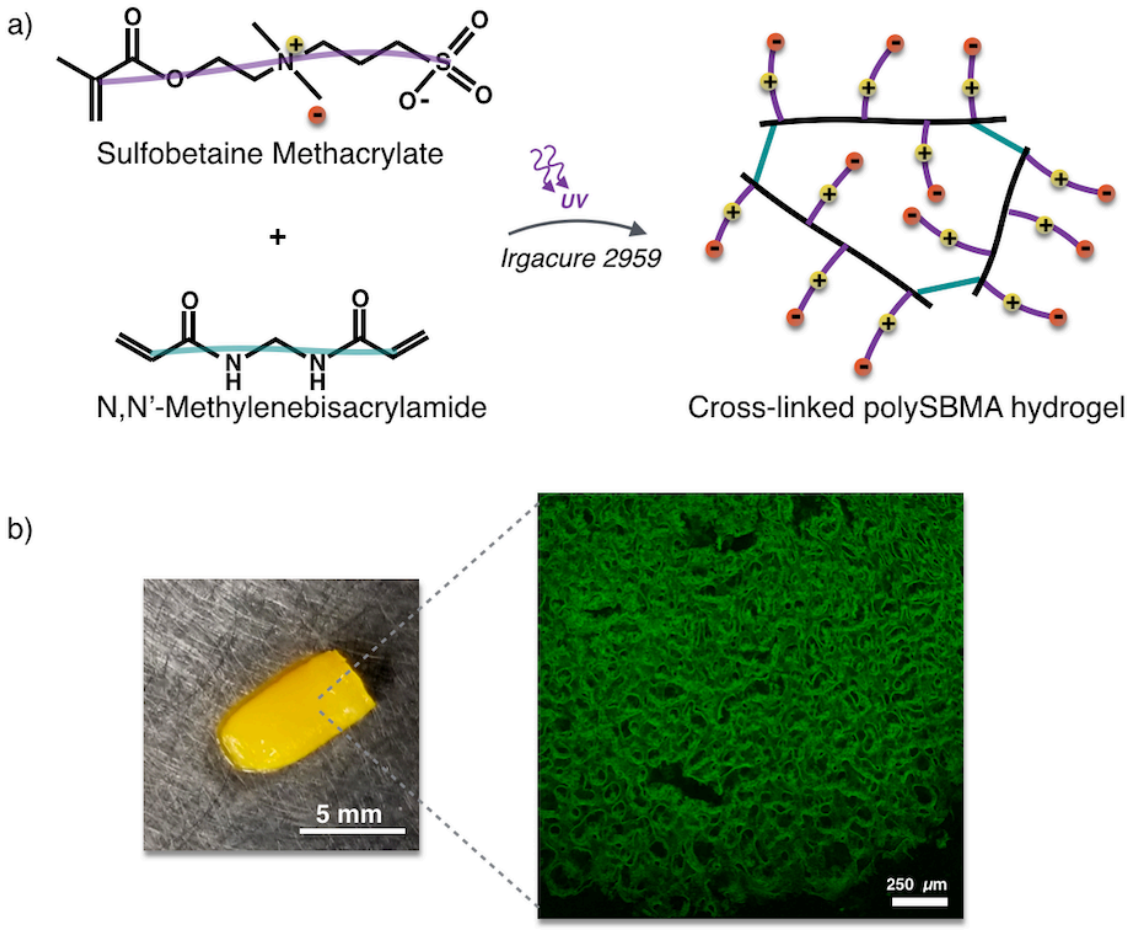

Figure 17. Zwitterionic sulfobetaine methacrylate (SBMA) scaffolds processed using W/L bijels. a) Color-coded schematic of SBMA cross-linking using N'N'-methylenebisacrylamide and b) digital camera and confocal microscopy image of a representative bijel-derived SBMA hydrogel scaffold.

bijels stabilized by FITC-labeled silica and allowed to partition into the water-rich phase at 70°C for four hours. After equilibration, polymerization was initiated with UV light to form the final cross-linked SBMA hydrogels, represented schematically in Figure 17a and confirmed with confocal microscopy in Figure 17b. Bijel-derived zwitterionic hydrogels may further enhance foreign body response mitigation, therefore, future research investigating tunability of mechanical properties and protein adsorption using these intriguing materials is recommended.

2.2.4 MICROSTRUCTURAL CHARACTERIZATION OF MATERIALS PROCESSED USING BIJELS

Because the high-performance electrodes and biomaterials described in previous section were processed from bijels, their specific microstructural features such as pore size uniformity and near-spinodal curvature are inferred from their source template. Although microscopy techniques such as scanning electron microscopy (SEM) aid in material characterization, thorough quantification of microstructure in bijel-derived materials would substantiate their place as scalable near-spinodal materials. To this end, microstructural characterization was performed on processed bijels and several competing porous materials using micro-computed tomography (microCT), a common technique used in medical imaging and material characterization.[91] Briefly, X-rays are guided to a sample fixed on a rotating stage (Figure 18a). Some X-rays are blocked by the presence of contrasting material while remaining X-rays hit the detector and are transformed into single image slices with the sample appearing white (Figure 18b). These slices may be viewed individually or used to create 3D reconstructions of the material with

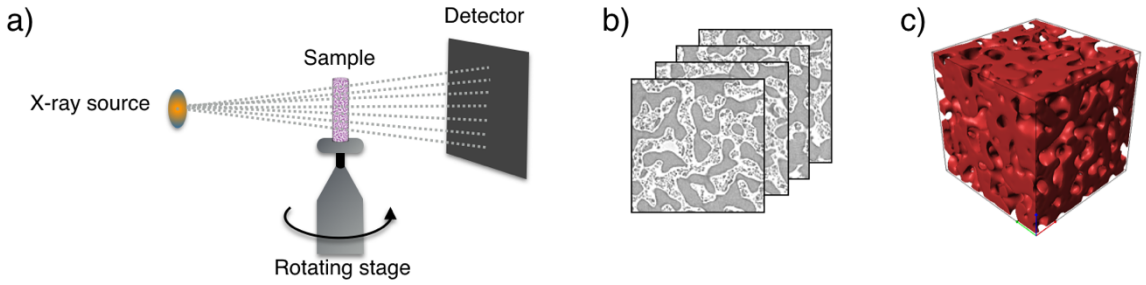

Figure 18. Key features of microCT. a) Components include an X-ray source, rotating sample stage and X-ray detector, b) single images slices gathered at each rotational position, and c) 3D reconstruction of stacked image slices, processed in ScanIP®.

micrometer resolution (Figure 18c).[92] An in-depth discussion of all characterization algorithms will be disclosed by Kyle McDevitt of the UCI Colloid Science Laboratory in the future. For this dissertation, I will highlight major findings as they relate to near-spinodal surface biomaterials.

Porous materials used in this study include a bijel-derived polymer scaffold processed by pyrolysis to leave only a carbon scaffold (Figure 19a), a bijel-derived poly(3,4-ethlylenedioxythiophene) (PEDOT) polymer scaffold (Figure 19b), an off the shelf porous metal (Figure 19c), a polystyrene high internal phase emulsion (polyHIPE) foam (Figure 19d), and a PEGDA inverse opal (Figure 19e). Porous metals are commonly used for thermoforming defect-free automotive parts,[93] while polyHIPE foams and inverse opal polymers and further processed metal materials have been used as regenerative medicine[18,94] and energy storage and discharge[95,96] materials, respectively.

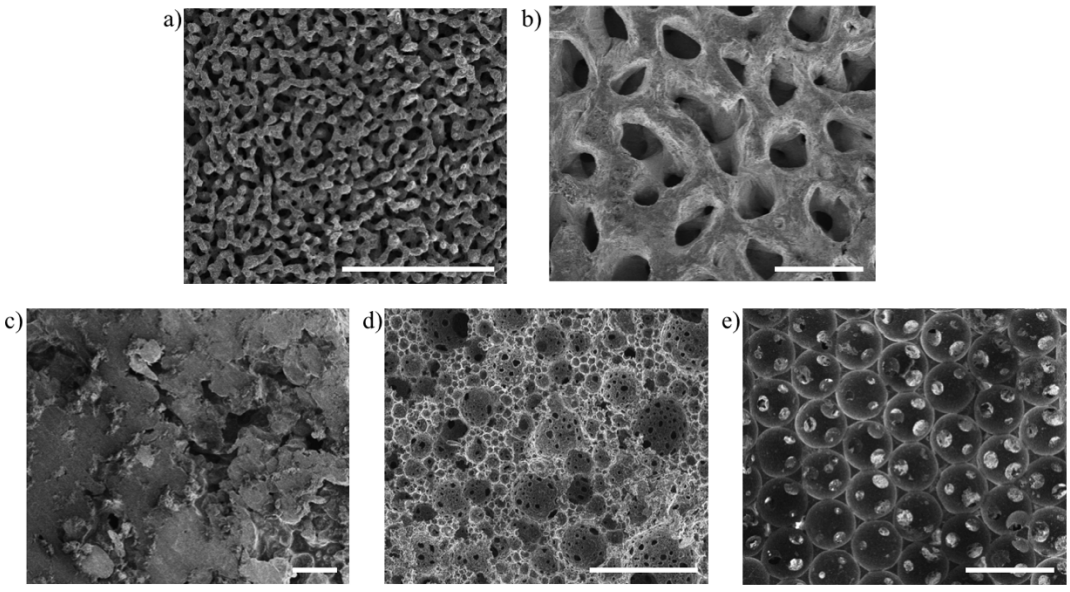

Figure 19. Porous materials for microstructural analysis. a) carbon bijel, b) polymer bijel, c) porous metal, d) polyHIPE, e) inverse opal. Scale bars: 200 μm.

3D reconstructions of the image slices generated by microCT were processed and exported using the ScanIP® module of Simpleware®.[97,98] The polymer bijel sample reconstruction is pictured in (Figure 20a) with centerlines drawn throughout the pore phase. These centerlines were calculated using a skeletonization technique termed the "medial axis," representing lines connecting points within the pore phase equidistant from the material surface.[99] The distance from the medial axis to the material surface is used to calculate the domain size distribution for the pore and solid phases throughout the material (presented as histograms in Figure 20b). The pore domain size in the bijel-derived materials exhibits the tightest, near-normal distribution of all test materials, meaning the pore size throughout the sample is approximately unchanged. Recall from the previous section that the liquid phases evolve in a self-similar manner, hence this tight distribution of pore size is expected of a bijel-derived material. By contrast, the distribution of pore size in the polyHIPE and porous metal is broad, signifying a wide range of pore sizes. The inverse opal has a bimodal distribution of pore size as a result of a microparticle templating process; the larger pores correspond to the diameter of the microparticles, while the smaller pores correspond to the diameter of microparticle contacts, termed pore throats.[100] Pore size uniformity is important for many applications such as high

permeability reactors,[101] cell migration,[19] and vascularization.[102] In Chapter 3, I discuss how pore self-similarity relates to loading soft materials and cell delivery and in Chapter

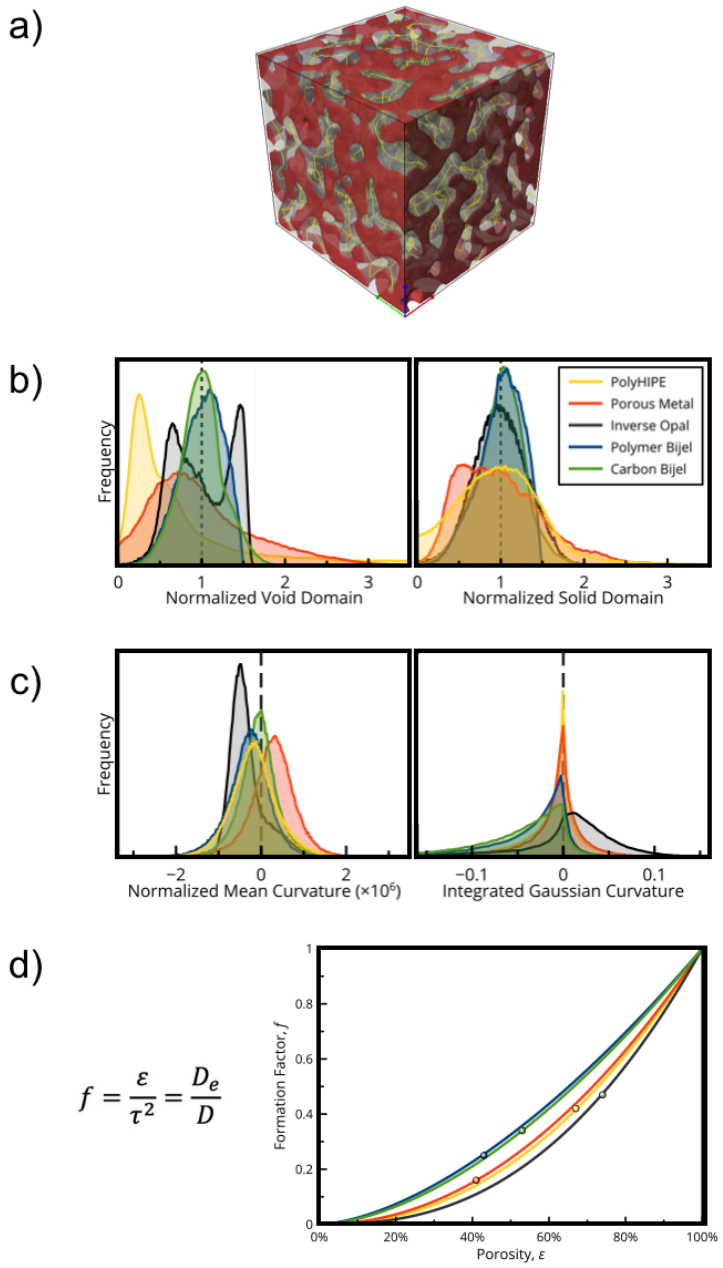

Figure 20. Microstructural characterization of bijel processed and other relevant porous materials. a) 3D reconstruction of a polymer scaffold processed using a bijel and b) domains size histograms, c) curvature histograms, and d) formation factor trends for all studied materials

4, I discuss its relation to beneficial tissue integration.

Next, the mean and Gaussian curvature of the bijel-derived samples (especially the carbon bijel) resemble near-spinodal surfaces (Figure 20c) with mean curvature centered near zero and negatively skewed Gaussian curvature. The mean curvature peak for the polymer bijel material is negative, which may be a result of delayed interfacial jamming from a lower particle loading fraction. As the percolating fluids phase separate, gravity may influence separation of fluids with differing densities, limiting the normal bijel pore size maximum to approximately 100 μm[54]; however, this limit has been pushed up to approximately 800 μm by forming "bridged bijels."[103] Nevertheless, both bijels have strongly skewed negative Gaussian curvature distributions indicating a prevalence of saddle surfaces. The mean curvature distributions observed in the other porous materials all peak away from zero and do not have dominant negative skews in their Gaussian curvature distributions. Spherical pore features drive the distribution positive (dominant in the inverse opal), while sphere-sphere connections present in all non-bijel materials give rise to negative Gaussian curvatures measurements. Curvature is highly implicated in high strength materials[21,104] and has more recently been the topic of biomaterial articles as an important factor in cell orientation,[105] migration,[106] differentiation,[107] and the foreign body response.[108] In Chapter 3, the mechanical properties of bijel-derived materials for robust cell delivery composites are exploited and discussed, while in Chapter 4, potential implications of curvature on progression of the foreign body response and tissue integration are discussed.

The ratio of the effective diffusivity, D_e, to the intrinsic diffusivity, D, through a porous material is calculated using the microstructural features tortuosity, τ, and porosity, ε, using Equation (2)[109]

$$\frac{D_e}{D} = \frac{\varepsilon}{\tau^2} \tag{2}$$

Porosity is calculated using the 3D surface reconstruction and tortuosity, a universal measure for how a diffusion path twists or deviates from a straight line,[110] is calculated using medial axis information. To compare the microstructure's effect on diffusivity in similarly porous material, a formation factor, $f = D_e/D$ is defined and scaled using a power law dependence on porosity, $f(\varepsilon) = \varepsilon^m$ where *m* is fit using least squares.[111] The formation factor curves as a function of porosity in the studied porous materials reveal that the bijel-derived materials always have the highest value and therefore, diffusive transport in these materials is the least affected by microstructure features. The formation factor trends for the two bijel-derived materials are essentially overlapping signifying that the microstructure is preserved after processing bijels with different pore sizes and materials. Diffusive transport through porous materials is of interest in many sectors including gas diffusion layers for efficient fuel cell operation[111] and pertinent to this dissertation, transport of nutrients and waste to support healthy cell proliferation and tissue growth.[24]

2.2.5 INSTANT PROCESSING OF BIJELS

Though the traditional bijel processing method is robust to selection of polymer precursors, there remains a time-limiting step (~3-4 hours) to allow for the equilibration of the added precursor. As W/L bijels are maintained at higher temperatures, the constituent fluids may evaporate, thereby disrupt the bijel microstructure and the processing steps. This evaporation related disruption is especially problematic when trying to form bijel-derived thin films. A triacrylated PEG material (ethoxylated trimethylolpropane triacrylate, denoted as PEGTA) and Darocur® 1173 photoinitiator are introduced directly to the W/L bijel system to bypass the equilibration time issue. In this new W/L/PEGTA system, the fluids are miscible at room temperature, but phase separate into a water-rich and with 2,6-lutidine/PEGTA-rich phase when heated. A probe station (Figure 21) was assembled by Herman Ching of the UCI Colloid Science Laboratory in which a laser is directed through a W/L/PEGTA-loaded cuvette and detected by a photodiode detector. The photodiode voltage and temperature of the fluid system are continuously recorded in LabView using a myDAQ data acquisition module (National Instruments), and the fluid system is heated by a hot plate. At the onset of phase separation and beyond, the fluid sample develops a cloudy appearance as droplets nucleate and grow causing laser light to scatter. Temperature at which light begins to scatter in surfactant stabilized water/oil micelles is known “Cloud Point Temperature”[112] and has been used analogously for constructing the coexistence curve for styrene trimer/polybutene bijels.[68]

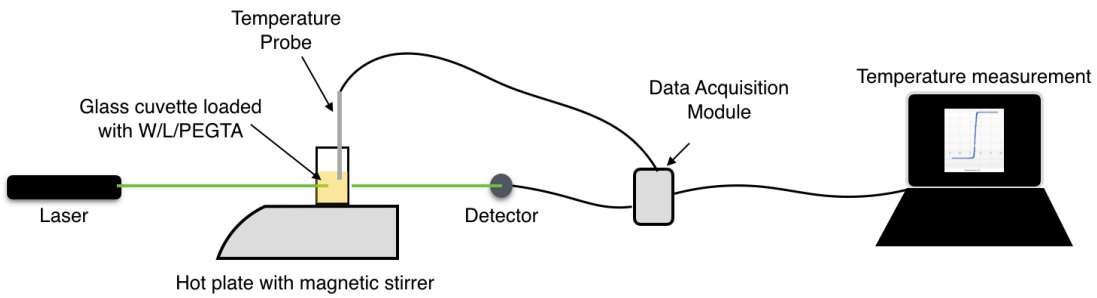

Figure 21. Cloud point temperature probe station

By varying the composition of the fluid system and recording the cloud point temperature, a W/L coexistence curve was assembled (show in Figure 22b, blue data) which resembles that reported by others.[54] The blue arrow in Figure 22b represents the critical solution (x_{Lut} = 0.064) used to traditionally form and process W/L bijels. The W/L/PEGTA coexistence curve (Figure 22b, yellow data) was assembled again by cloud point temperature and varying W/L composition while maintaining a PEGTA concentration of 22% v/v relative to the total volume. The generated data indicates that the introduction of PEGTA to the W/L bijel system shifts the Tc to approximately 37°C and the critical solution to approximately x_{Lut} = 0.048 (Figure 22b, yellow line). Formation of PEGTA scaffolds with bijel-like morphology was demonstrated using a near critical solution heated via electromagnetic radiation (microwaves) and immediately polymerized with UV light (using RITC- and FITC-labeled silica, Figure 22c and Figure 22d, respectively). The described processing here is described as “instant” because each sample can be synthesized in under five minutes, a sizeable time difference when compared to traditional bijel processing that requires at least four hours to complete. Therefore, the instant

processing method established here provides a method for large-scale production of bijel-derived consumables.

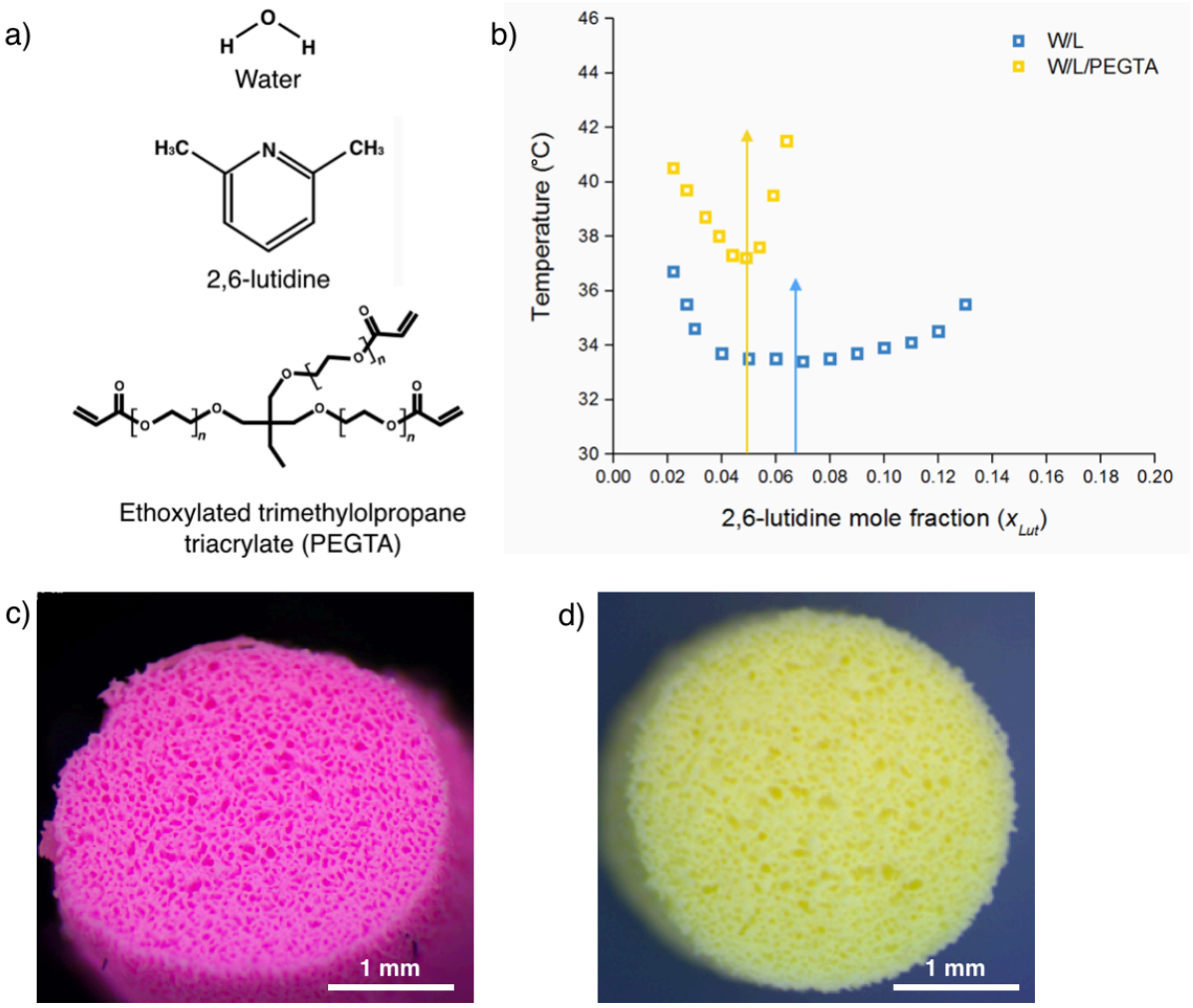

Figure 22. Demonstration of instant bijel processing. a) Coexistence curves for W/L and W/L/PEGTA bijels experimentally determined using cloud point temperature and processed polymer scaffolds using RITC-(b) and FITC-(c) labeled silica.

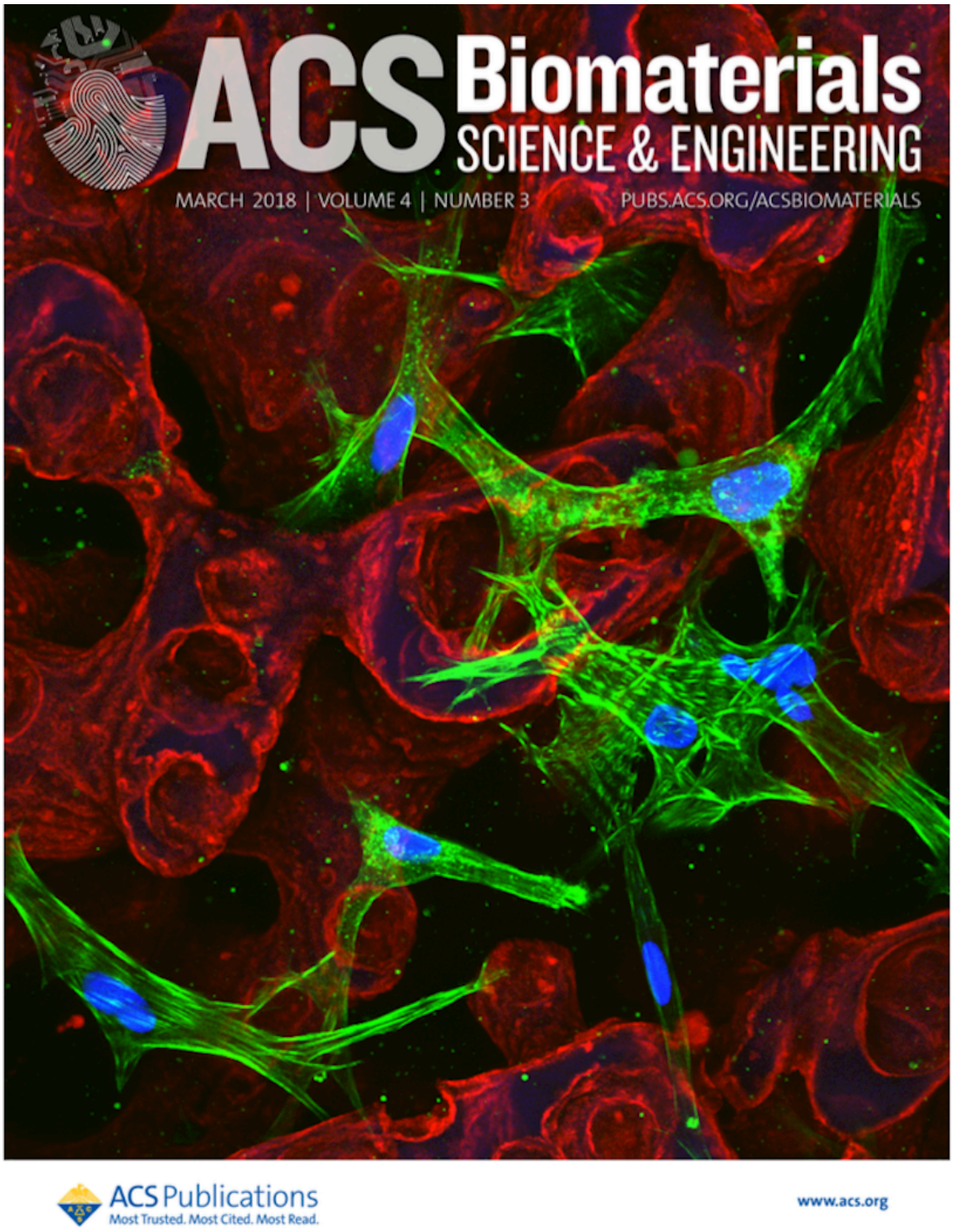

Figure 23. Composite Bijel-Templated Hydrogels for Cell Delivery. Reprinted with permission from *ACS Biomaterials Science and Engineering* **2018**, *4* (2), 587-594. Copyright 2018 American Chemical Society.

CHAPTER 3. COMPOSITE BIJEL-TEMPLATED HYDROGELS FOR CELL DELIVERY

3.1 INTRODUCTION

As broached in Section 1, hydrogels have been extensively explored as regenerative biomaterials that offer tunability of surface chemistry, stiffness, and degradability while providing a cross-linked matrix that mimics native tissue environments.[15,16] Hydrogels of both natural and synthetic origin have been widely used as regenerative medicine materials.[113–115] Fibrin, a natural origin hydrogel formed as a result of the thrombosis cascade, provides an attractive bio-mimetic extracellular matrix for cell delivery.[6,116,117] However, weak mechanical properties complicate implantation, and natural forces encountered within the body may undesirably deform fibrin during in situ gelation approaches.[118,119] Conversely, synthetic hydrogels can be used to generate mechanically robust cell encapsulation matrices using a variety of processing conditions, but they do not provide a viable fibrous three dimensional (3D) extracellular matrix (ECM) mimic for cell attachment and growth.[120] Numerous strategies have been developed that incorporate natural, cell recognizable motifs in synthetic hydrogels for the fabrication of hybrid biomaterial systems. For instance, Arg-Gly-Asp (RGD) adhesion and matrix metalloproteinase (MMP) degradation sites have been incorporated into synthetic polymers for increased control of cell viability and differentiation.[121–124] While these hybrid approaches enable more functional cell encapsulation materials, cells do not experience a completely natural fiber matrix for phenotype preservation, and transport of cell metabolites and waste is often limited. A composite system that selectively offers the

advantages of an unmodified, natural encapsulation hydrogel and a synthetic support scaffold can aid in overcoming drawbacks experienced in current cell delivery strategies.[19]

One inherent advantage of using hydrogels in regenerative medicine is the flexibility offered in processing conditions, permitting the creation of microporous scaffolds containing interconnected pore networks for enhanced proliferation, migration, and transport pathways.[9,125] Common processing techniques for generating porous hydrogels include porogen templating of particles[19,126], ice[127,128], and salt[129,130], high internal phase emulsion (HIPE) polymerization[18,131], electrospinning[132,133], and projection stereolithography (PSL).[10,24] While porogen templating, HIPE polymerization, and other process-based techniques are able to readily generate porosity in scaffolds, precise control of the entire architecture is often limited with these techniques. The result is typically a random pore morphology that can lead to unreliable loading of cells and therapeutics, underutilized scaffold surface area, unpredictable mechanical properties, and constricted transport pathways. Rapid prototyping methods such as PSL offer layer-by-layer construction of rationally designed biomaterial architectures.[134] Such techniques are able to generate arbitrarily complex scaffolds that exhibit enhanced transport and mechanical properties. Examples include porous constructs based on minimal surface models (e.g. Schwarz D, Schoen's G) marked by periodic geometric units that form fully interconnected, co-continuous solid-void phases.[10] However, using layer-by-layer techniques to fabricate features with micro-scale resolution remains inefficient, rendering scale-up processing impractical.[24,71]

Herein, we report a self-assembly-based processing technique for the generation of morphologically unique hydrogel composites comprised of fully interconnected bicontinuous phases with uniform and tunable pore sizes. We demonstrate the utility of our composites as mechanically robust cell delivery systems that enable uninhibited delivery in a natural environment. Bicontinuous interfacially jammed emulsion gels (bijels) are a new class of non-equilibrium soft materials first proposed via simulations in 2005[40] and realized experimentally in 2007.[54,101] Bijels are formed by colloidal particle self-assembly and kinetic arrest of spinodal decomposition in partially miscible binary solutions. Spinodal decomposition prompts widespread coarsening of the fluid-fluid interface when the system is quenched at its critical composition. Particles with equal affinity for the two fluid phases strongly adsorb at the interface during phase separation. Phase separation is kinetically arrested once the interfacial area is fully occupied by particles, and the mixture undergoes a sharp gelation transition (Figure 1a-c).[62,135] Bijels exhibit predictable morphological attributes distinguished by bicontinuous, fully interpenetrating, non-constricting microchannels separated by a nanoparticle monolayer.[101] Furthermore, the self-assembly of bijels driven by spinodal decomposition naturally forms a minimal surface geometry marked by uniform domain size, negative Gaussian curvature and vanishing mean curvature. These unique features culminate to form an internal architecture with saddle points at the majority of internal surface sites.[20] Finally, control of the characteristic domain size, x_i, within the range $5\ \mu m < x_i < 800\ \mu m$, is afforded through particle loading, where higher particle volume fractions arrest spinodal decomposition at an earlier stage, resulting in a smaller domain size, and vice versa.[54,103]

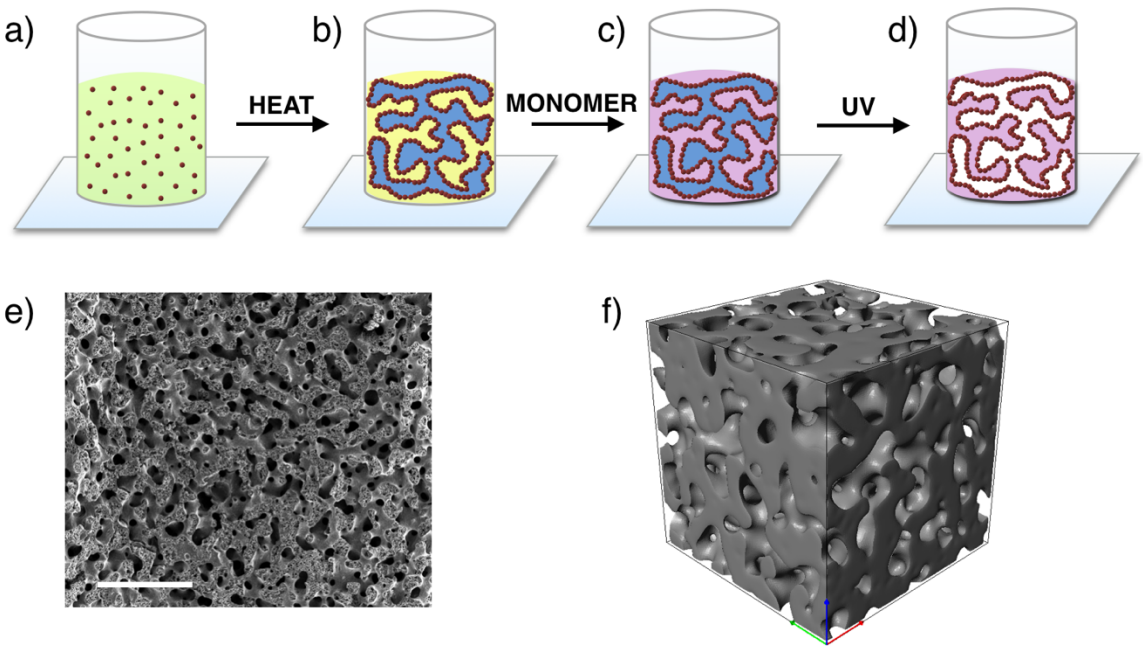

Figure 24. Bijel-templating process schematic and representative scaffold morphology. a) A mixture of water/2,6-lutidine/silica nanoparticles is loaded into a glass tube. b) The mixture is heated *via* microwaves to trigger spinodal decomposition and subsequent bijel formation as the water/2,6-lutidine interfacial area becomes fully populated by silica nanoparticles. c) PEGDA/Darocur 1173 solution is added to the top surface of the bijel and selectively partitions to the 2,6-lutidine phase. d) UV light initiates radical polymerization and excess liquids are removed from the now bijel-templated scaffold. e) Scanning electron microscopy micrograph (Scale bar: 500 μm) and f) Nano-computed tomography 3D reconstruction of a processed bijel-templated PEG scaffold.

As described in Section 2.2.1, Lee and Mohraz demonstrated in 2010 that bijels could serve as robust templates for fabrication of microporous materials containing the inherent morphological features of the parent bijel.[75] Extending these techniques, the present study utilizes bijels for the template-based synthesis of porous polyethylene glycol (PEG) scaffolds with spinodal-like microstructure, in which the domain size is specifically tuned to facilitate robust cell loading and migration, uninhibited by pore-to-pore constrictions present in porogen-templated biomaterials.[19] Composite bijel-templated hydrogels (CBiTHs) are then synthesized by filling the interconnected micro-

channel network inside the PEG scaffold with a cell-encapsulating fibrin matrix. CBiTHs combine the advantages of natural and synthetic hydrogels, enabling a mechanically robust material in which a natural 3D ECM phase is present and readily accessible throughout the volume. The utility of CBiTHs as cell delivery systems is demonstrated through tracking of normal human dermal fibroblast (NHDF) loading and delivery to initially-acellular surrounding fibrin gels.

3.2 MATERIALS AND METHODS

3.2.1 MATERIALS

All reagents and materials were used as received. Rhodamine B isothiocyanate (RITC), tetraethyl orthosilicate (TEOS), 2,6-lutidine, poly(ethylene glycol) diacrylate (PEGDA; number average molecular weight (M_n): 258 g mol^{-1}), protamine sulfate, thrombin from bovine plasma, formalin solution (neutral buffered, 10%), bovine serum albumin, and fluorescein isothiocyanate-dextran (average molecular weight: 150 kDa) were purchased from Sigma-Aldrich. (3-aminopropyl) triethoxysilane (APTES) was purchased from TCI America. Poly(dimethylsiloxane) (PDMS) was purchased from Dow Corning. 2-hydroxy-2-methylpropiophenone photoinitiator (Darocur 1173) was obtained from Ciba Specialty Chemicals. Ammonium hydroxide (Fisher Chemical), Dulbecco's modified eagle's medium (DMEM, Gibco), fetal bovine serum (Gibco), penicillin streptomycin (Gibco), phosphate buffered saline (PBS, Gibco), Alexa Fluor 488 fibrinogen (Invitrogen), Alexa Fluor 488 phalloidin (Invitrogen), 4',6-diamidino-2-phenylindole, dihydrochloride (DAPI, Invitrogen), and Triton-100x (Arcos Organics) were purchased

from Thermo Fisher Scientific. Green fluorescent protein reporter plasmid (QM511B-1, Systems Biosciences) and lentivirus titer were generously supplied by Professor Timothy Downing (UC, Irvine). Ultraviolet (UV)-curable adhesive (NOA 61) was purchased from Norland Products.

3.2.2 PREPARATION OF BIJEL-TEMPLATED HYDROGEL SCAFFOLDS

Bijels were used as the template platform for synthesizing polyethylene glycol (PEG) scaffolds. Fluorescently modified silica nanoparticles (500 nm) were synthesized following an adapted Stöber process.[136] First, RITC was coupled to APTES by mixing 12.5 mg RITC and 24.9 mg APTES in 10 mL of ethanol at room temperature overnight. The resulting dye solution was split into two flasks containing 4.18 mL TEOS, 10 mL ammonium hydroxide solution, and 56 mL ethanol and continuously stirred overnight. Silica nanoparticles were washed with deionized water and pelleted via centrifugation (12 minutes, 2500 rpm) three times and dried under vacuum at 135ºC until neutrally wetting surface chemistry was observed. Nanoparticle wetting properties were tracked using an inverted microscope coupled to a Vt-eye confocal scanner (VisiTech International). Bijels were formed by dispersing 1% (v/v) silica nanoparticles in a critical mixture of Milli-Q water and 2,6-lutidine (x_{Lut} = 0.064) using a Branson Sonifier 250 (Emerson). The mixture was transferred to a custom-assembled vessel comprised of a cylindrical glass tube (5 mm inner diameter) oriented vertically on a microscope coverslip using PDMS as a bonding agent between the two glass components (Figure 24a). Microwave heating was supplied to initiate spinodal decomposition and bijel formation (Figure 24b). Bijels were allowed to

stabilize for 10 minutes in an oven maintained at 70ºC. A hydrogel precursor solution of PEGDA containing 1% v/v Darocur 1173 photoinitiator was chosen to naturally partition into the 2,6-lutidine phase. 35 μL of this solution was gently added to the top surface of the bijel and allowed to diffuse for at least 2 hours at 70ºC (Figure 24c). Radical polymerization of the PEGDA-loaded 2,6-lutidine phase was performed using a UV lamp (Lumen Dynamics; wavelength: 300-500nm) for a period of 100 seconds, thereby locking the templated structure in place (Figure 1d). PEG scaffolds were removed from the glass vessels, rinsed twice with isopropyl alcohol, and allowed to dry uncovered at room temperature overnight.

3.2.2.1 ADDITIONAL BIJEL-TEMPLATED PEG SCAFFOLD PREPARATION AND IMAGING METHODS

Morphological features of the bijel-templated PEG scaffolds were confirmed *via* scanning electron microscopy (SEM) and micro-computed tomography (microCT). The conductive polymer poly(3,4-ethylenedioxythiophene (PEDOT) was cast in the PEG scaffold to reduce charging during SEM and enhance X-ray contrast during nano-CT. PEG scaffolds were soaked in 3,4-ethylenedioxythiophene (EDOT, Sigma-Aldrich) for 30 minutes, then placed in a solution of 0.195 g iron (III) p-toluenesulfonate hexahydrate (Sigma-Aldrich) and 1 mL isopropyl alcohol (IPA) maintained at 135 ºC for 1 hour. The sample was washed twice in IPA and dried at room temperature before imaging. SEM was performed using a Quanta 3D FEG Dual Beam Microscope (FEI) under 75x magnification with a working distance of 24.6 mm. NanoCT was performed using a Xradia

VersaXRM-410 (Zeiss) under 20x magnification with a scan resolution of 2.28 μm. The scan was processed in Simpleware (Synopsis) to generate the corresponding 3D reconstruction of the bijel-templated PEG scaffold.

3.2.3 CELL CULTURE

Adult normal human dermal fibroblasts (NHDFs) were obtained from Lonza (CC-2511) and cultured at 37^{o}C under air supply containing 5% carbon dioxide (CO_2). DMEM containing 10% fetal bovine serum and 1% penicillin streptomycin was used as the culture medium. Cells were grown to 90% confluency before passaging. Passage numbers no greater than 8 were used for all testing.

3.2.4 GFP EXPRESSION IN NHDFS

Green fluorescent protein (GFP) expression was used for live tracking of NHDFs during all experiments. GFP expression was achieved through transduction using a QM511B-1 plasmid with a GFP reporter and EF-1α promoter sequence. The plasmid was packaged in lentivirus particles. NHDFs (passage number 4) were seeded into a 12-well plate at a concentration of 150,000 cells/well. Culture medium (1 mL) supplemented with the lentivirus titer and protamine (7 μg/mL) was added to each well and cultured for 48 hours to achieve a transduction efficiency of at least 90%.

3.2.5 FIBRIN AND NHDF LOADING IN BIJEL-TEMPLATED SCAFFOLDS

NHDFs were trypsinized and re-suspended in 2.5 mg/mL bovine fibrinogen solution at a concentration of 1 million cells/mL for all loading experiments. For sterilization, bijel-templated PEG scaffolds were irradiated under UV light for 15 minutes, soaked for 5 minutes in a 70% ethyl alcohol solution, and soaked for 5 minutes in fresh PBS (x3). Fluorescently labeled fibrin was obtained by supplementing the fibrinogen solution with 5% (w/w) Alexa Fluor 488 fibrinogen. PEG scaffolds were cut into disks (3 mm diameter, 2 mm height) and dried in an oven maintained at 80°C. After drying, disks were placed on glass-bottom dishes (MatTek) and pre-wetted with 10 μL PBS. 100 μL of the cell-loaded fibrinogen solution was mixed with thrombin (1 U/mL) by gentle pipet mixing in a micro-centrifuge tube on ice. The resulting mixture was pipetted into the disks by placing the pipet tip gently on the middle section of the top surface of the disk and slowly ejecting the fluid. Fibrin gelation occurred over 30 minutes to yield NHDF-loaded CBiTHs. Culture medium was added and the CBiTH dishes were incubated at 37°C under 5% CO_2 air supply. Control fibrin gels were plated on separate glass-bottom dishes for each experiment.

3.2.6 CELL DELIVERY TO ACELLULAR FIBRIN GELS

NHDF-loaded CBiTHs were allowed to stabilize for one hour under normal incubation conditions. For delivery to acellular fibrin gels, a biopsy punch with an inner diameter of 2 mm was used to cut out cylindrical sections of the CBiTHs. The cut piece was placed onto a new glass-bottom dish and a fresh mixture of fibrinogen and thrombin

(2.5 mg/mL and 1 U/mL, respectively) was deposited circumferentially around the transferred piece. The newly deposited fibrin gels were allowed to form for 30 minutes. Culture medium was added, and the dishes were returned to incubation conditions (Figure 25).

3.2.7 TIME-LAPSE TRACKING OF NHDF DELIVERY

Confocal microscopy imaging was performed at 2-day intervals for a total of 8 days using a FluoView 1200 laser confocal scanning system (Olympus). Pixel density per area was used to report cell density in all experiments, and MATLAB (MathWorks) was used for image processing. Portable network graphics (PNG) images were read into MATLAB and passed through the multilevel threshold function “multithresh.” The dimmest pixel class, Class 1, was excluded for all subsequent processing. Pixel density, ϕ, was defined as the fraction of class 2 and 3 pixels at each radial distance beginning at the CBiTH-acellular fibrin interface. At each time point, ϕ was evaluated and total bright pixels outside the CBiTH were counted (n=3). At the conclusion of the experiment, all samples were fixed with 10% formalin solution, permeabilized with 0.1% (v/v) Triton-100x in PBS and blocked with 2% bovine serum albumin. F-actin fibrils were stained with Alexa Fluor 488 phalloidin, and nuclei were stained with DAPI for fluorescence confocal microscopy.

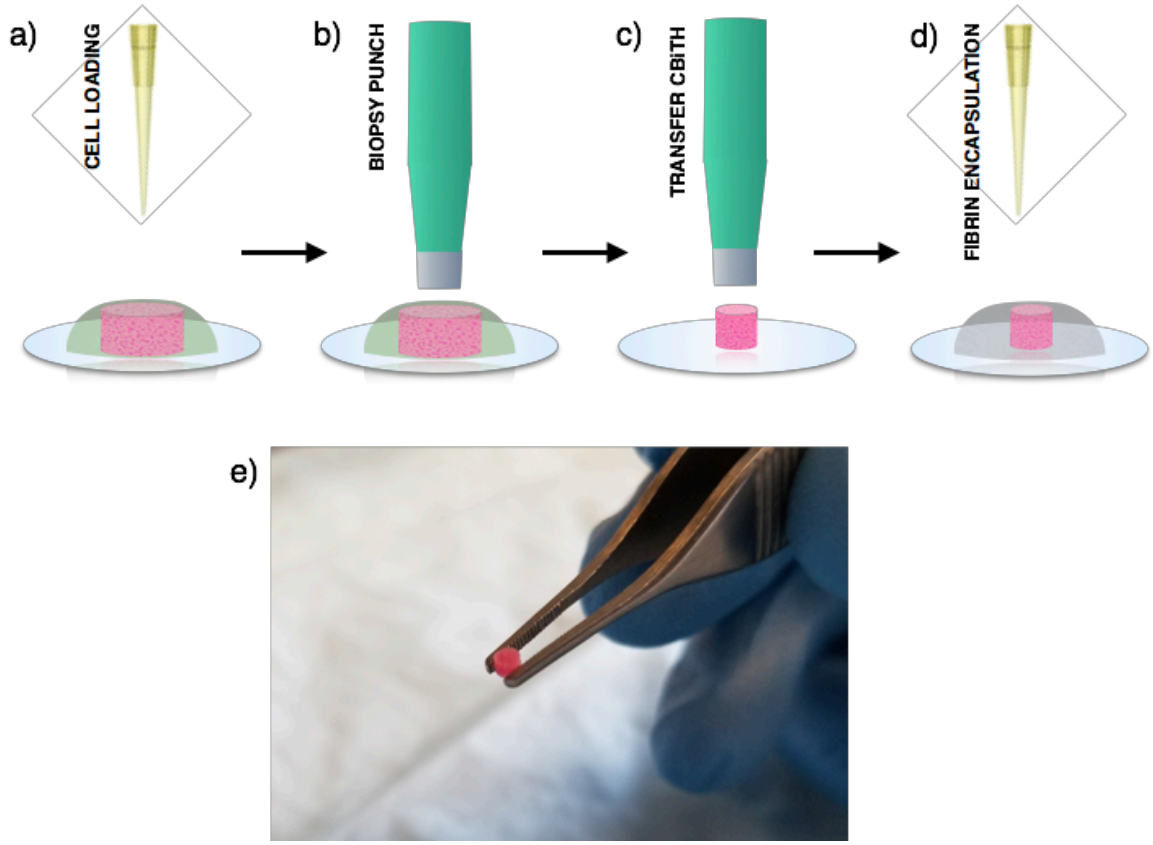

Figure 25. Cell delivery to acellular fibrin schematic. a) NHDF/fibrinogen/thrombin mixture is injected into the bijel-templated PEG scaffold to form the CBiTH. b) Biopsy punch cuts a cylindrical piece from the NHDF-loaded CBiTH. c) Cut piece is transferred to a fresh incubation dish. d) Fibrinogen/thrombin is added circumferentially around the CBiTH to encapsulate in acellular fibrin. e) CBiTH being held with forceps following biopsy punch.

3.2.8 DIFFUSION OF DEXTRAN IN BIJEL-TEMPLATED PEG SCAFFOLDS

Diffusion of a fluorescein isothiocyanate-conjugated dextran in bijel-templated PEG scaffolds was measured via time-lapse fluorescent imaging using the FluoView 1200 confocal system. Each sample (2 mm height, 1048 μm radius) was soaked in PBS for one hour and placed axially on a glass-bottom dish. A glass coverslip was then attached to the top of each sample using UV-curable optical adhesive. A dextran solution (500 μL,

5 mg/mL PBS) was loaded into the dish and images were captured under 4x magnification every 30 seconds for 60 minutes. Acquired images were then processed in MATLAB to calculate average pixel intensity per radial bin (Δr=57.58 μm). Normalized intensity was calculated by dividing average pixel intensity per bin by the average pixel intensity outside the sample. The experimental data generated from 3 separate samples were fit to a model of transient radial diffusion in cylindrical coordinates. Applying a constant-concentration boundary condition, the theoretical solution used for this model is shown in Equation 3:

$$\frac{c}{c_0} = 2\beta \sum_{n=1}^{\infty} \frac{J_0\left(\frac{\lambda_n r}{R}\right)\left[1-exp\left(-\frac{\lambda_n^2 D_e t}{R^2}\right)\right]}{\lambda_n J_1(\lambda_n)} \quad (3)$$

where r is the radial position; t is the time; R is the sample radius; D_e is the effective diffusivity of dextran in the scaffold; $\beta < 1$ accounts for the void phase of the sample available for dextran diffusion; J_0 and J_1 are Bessel functions of the first kind of zeroth and first order, respectively; and λ_n are the eigenvalues corresponding to solutions of $J_0(\lambda_n)=0$. Assuming average intensity is proportional to the local concentration, adjustable parameters β and D_e were extracted by fitting experimental average intensity data to the model using non-linear least-squared regression with 3000 terms in the series.

3.2.9 MECHANICAL TESTING

Compression tests were performed using a MTS Synergie 100 mechanical tester (MTS Systems, Eden Prairie, MN, USA). Control PEG hydrogels containing no microstructural features were prepared by UV polymerization of the PEGDA and Darocur® 1173 solution (36.2% v/v) in 2,6-lutidine in the custom-assembled cylindrical glass vessels. Samples of control PEG, bijel-templated PEG, and fibrin-loaded PEG

CBiTHs were cut into cylindrical disks (2 mm height, 2 mm diameter) using a razor blade and a biopsy punch. All samples were hydrated in PBS for at least 1 hour before testing (n=3). The cylindrical disks were placed onto the Synergie 100 stage and the compression adapter was lowered to the sample gap height of 2 mm. TestWorks4 (MTS Systems) was used to acquire data during compression to 50% of the sample height. Stress (σ) was plotted versus strain (ε), and the slope of the initial linear region was calculated using linear regression and reported as the sample's compressive modulus (E). The stress at each sample's failure point was reported as the compressive strength (σ_u).

3.2.10 STATISTICAL ANALYSIS

Two-sample, non-paired t-tests were performed in OriginPro (OriginLab, Northampton, MA, USA) for compression testing using the Bonferroni correction (three comparison groups). Results were considered statistically significant when $p < 0.0167$.

3.3 RESULTS

3.3.1 FIBRIN AND NHDF LOADING IN BIJEL-TEMPLATED PEG SCAFFOLDS

The feasibility of loading a natural hydrogel within the bijel-templated PEG scaffold was tested using fluorescently labeled fibrinogen followed by laser scanning confocal microscopy. A fibrous network microstructurally similar to control gels indicated that fibrinogen was uniformly loaded and homogeneously cross-linked within the interconnected void of the bijel-templated PEG scaffold, resulting in a hydrogel composite with bicontinuous, spinodal-like arrangement of its constituent PEG and fibrin phases

(Figure 26a-b). In the next experiment, NHDFs were added to the fibrinogen/thrombin solution and loaded in bijel-templated PEG scaffolds. NHDFs displayed spread phenotypes within the CBiTH after eight days in culture (Figure 26c).

3.3.2 CELL DELIVERY TO ACELLULAR FIBRIN GELS

Cell delivery of NHDFs to acellular fibrin gels was demonstrated using the biopsy punch technique described above. Confocal microscopy performed at two-day intervals over the span of 8 days showed that NHDFs loaded within hydrogel composite materials were able to migrate to the surrounding fibrin gels (Figure 27a; additional examples found in the Appendix 6.1). Quantitative tracking showed the development of a radial gradient in the cell population (bright pixel density), which increased over time indicating cell migration outside of the CBiTH boundary (Figure 27b). Taken as a whole, tracking of cell populations in the surrounding fibrin gels indicated the total cell density increased over time (Figure 27c). Active migration of NHDFs was directly observed via time-lapse fluorescent imaging. NHDFs were observed migrating within the fibrin-filled pores of the composite and moving into the surrounding fibrin gels over the course of 20 hours. In addition, NHDFs fixed and stained 8 days post-transfer were observed spreading within the fibrin phase of the CBiTHs, extending through pores at the boundary, and populating the previously acellular fibrin gels (Figure 28a). Confocal microscopy at increased magnification captured NHDFs at the CBiTH boundary in intimate contact with the surrounding fibrin matrix to further confirm cell delivery using the described in vitro delivery methods (Figure 28b).

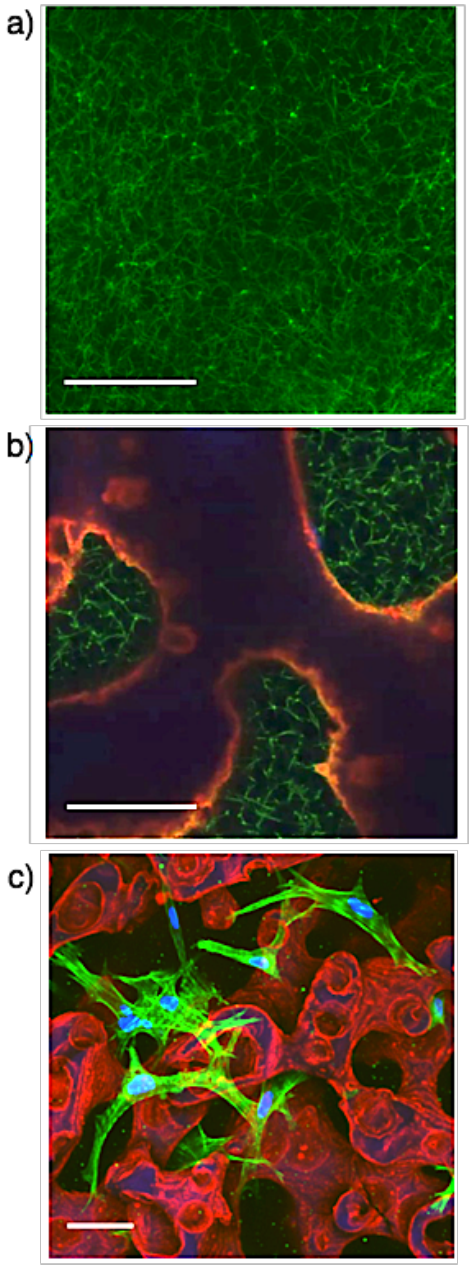

Figure 26. Fibrin and NHDF loading in bijel-templated PEG scaffolds. a) Confocal micrograph of typical fiber architecture in a fibrin control gel (Green: Alexa Fluor 488 fibrinogen, Scale bar: 50 μm). b) Confocal micrograph of a fibrin-loaded, bijel-templated PEG scaffold (CBiTH) (Green: Alexa Fluor 488 fibrinogen, Red: RITC-labeled silica nanoparticles, Scale bar: 50 μm). c) Confocal microscopy maximum intensity projection (image stack: 155 μm) of a NHDF-loaded CBiTH (Blue: DAPI labeling of cell nuclei, Green: Alexa Fluor 488 phalloidin labeling of F-actin, Red: RITC-labeled silica nanoparticles, Scale bar: 50 μm).

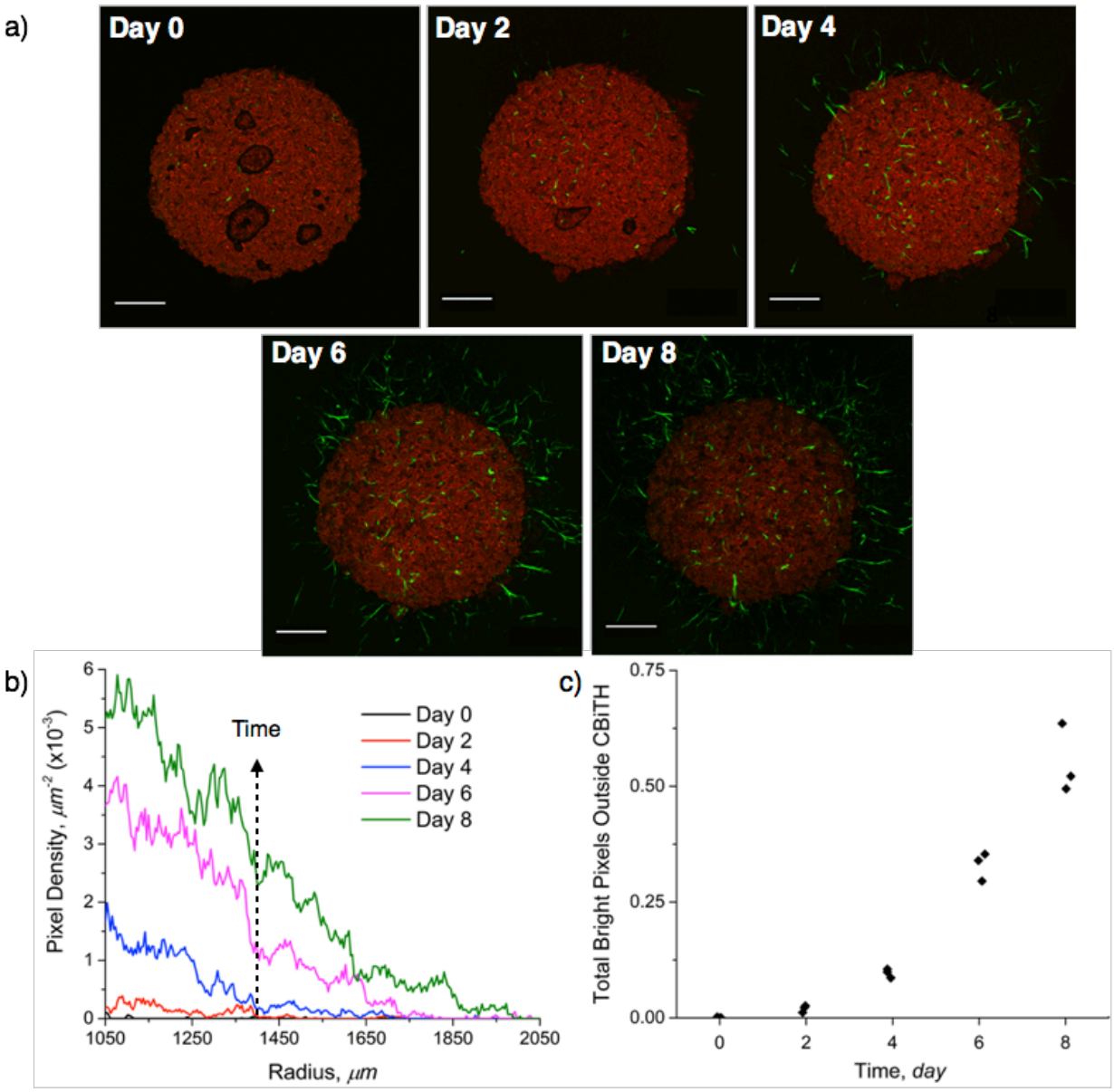

Figure 27. Time-lapse analysis of cell delivery to acellular fibrin hydrogels using NHDF-loaded CBiTHs. a) Confocal microscopy maximum intensity projections (day 0 image stack: 250 μm, days 2-8 image stack: 750 μm) tracking NHDF delivery over 8 days (Green: GFP expression in NHDFs, Red: RITC-labeled silica nanoparticles, Scale bar: 500 μm). b) Pixel density outside CBiTH boundary (Radius=1050 μm) plotted versus distance (n=3). Line color designations by time: Day 0 (–), Day 2 (–), Day 4 (–), Day 6 (–), Day 8 (–). c) Total bright pixel count outside each CBiTH versus time (n=3).

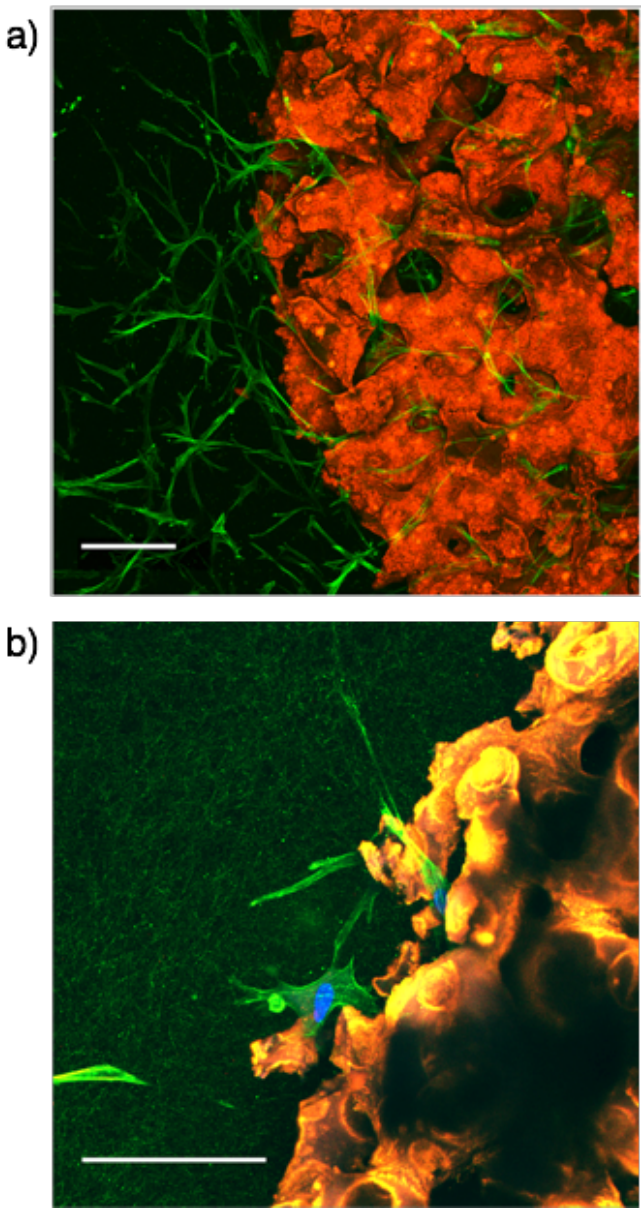

Figure 28. NHDF delivery to encapsulating fibrin after 8 days. a) Confocal microscopy maximum intensity projection (image stack: 225 μm) of the fibrin-CBiTH interface (Green: AlexaFluor 488 phalloidin labeling of F-actin, Red: RITC-labeled silica nanoparticles, Scale bar: 100 μm). b) Confocal microscopy maximum intensity projection (image stack: 75 μm) of the fibrin-CBiTH interface with added reflection imaging (Blue: DAPI labeling of cell nuclei, Green: reflected light and AlexaFluor 488 phalloidin labeling of F-actin, Orange: combination of the reflected light (green) and RITC-labeled silica nanoparticles (red), Scale bar: 200 μm).

3.3.3 DIFFUSION OF DEXTRAN IN BIJEL-TEMPLATED PEG SCAFFOLDS

The experimental results and fitting results of the transient radial diffusion model (Equation 3) for five radial locations are shown in Figure 29a. The model fits (solid lines) show good agreement with experimental data (open symbols) with extracted parameters

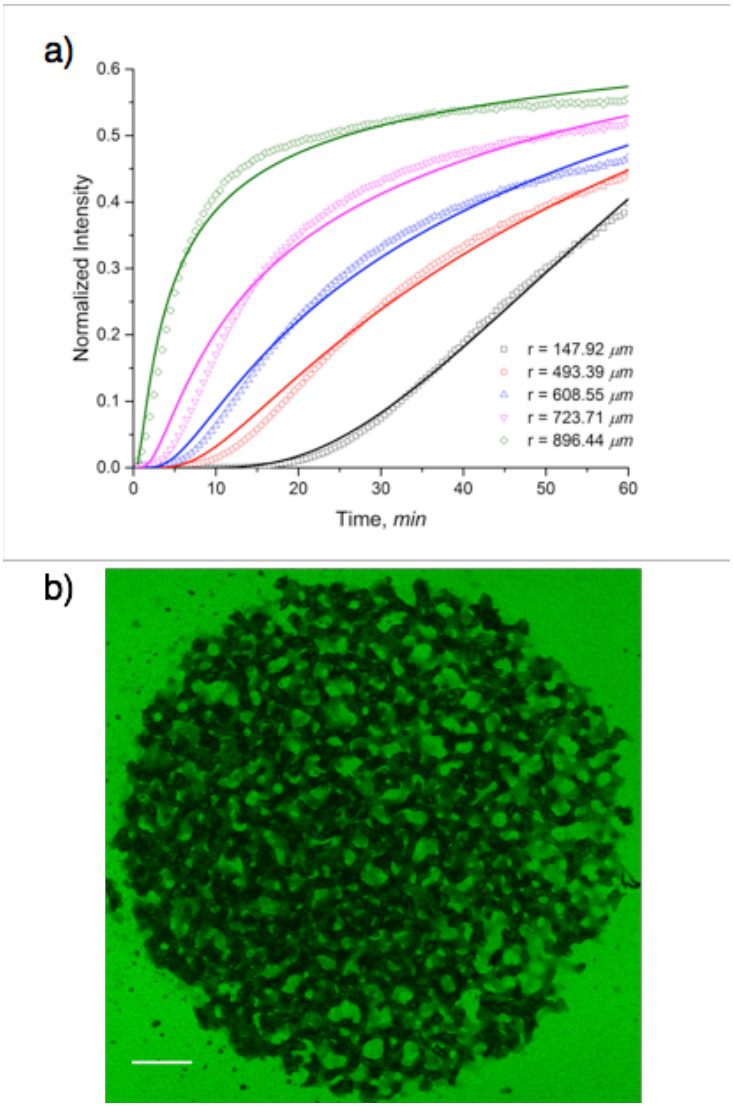

Figure 29. Dextran diffusion in bijel-templated PEG scaffolds. a) Normalized intensity over time of experimental data (open symbols, n=3) and transient radial diffusion model fits (solid lines) at 5 positions: r=147.92 μm (–), r=493.39 μm (–), r=608.55 μm (–), r=723.71 μm (–), and r=896.44 μm (–). b) Confocal micrograph of scaffold sample after overnight incubation in dextran solution (Green: fluorescein isothiocyanate-dextran, Imaging depth: 60 μm, Scale bar: 250 μm).

of D_e=5.06E-7 cm^2s^{-1} ± 15.45% and β=0.84. A confocal micrograph after overnight incubation in the dextran solution is shown in Figure 29b. Dextran, represented by fluorescence signal, was present in approximately 50% of the scaffold (Figure 30).

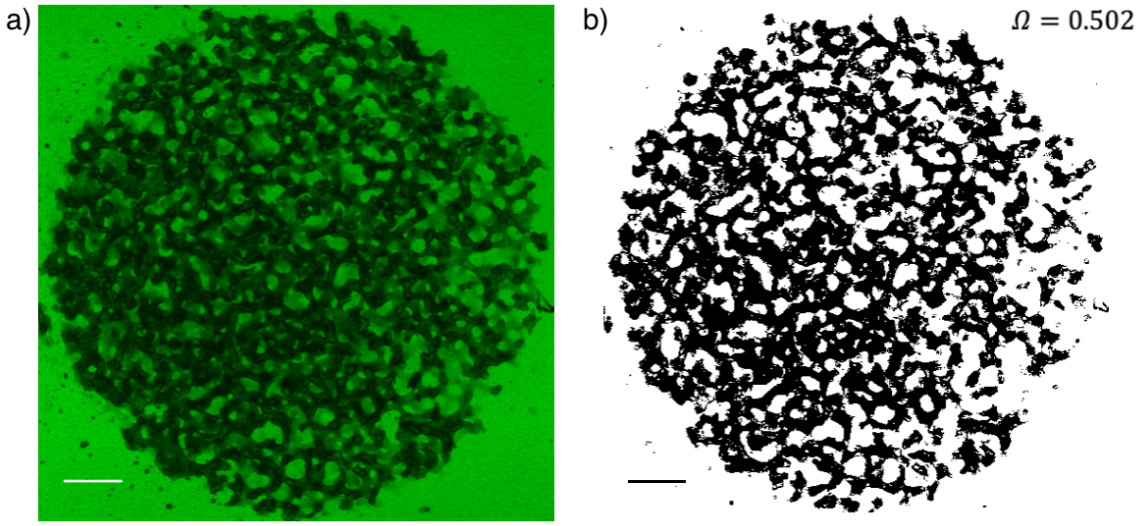

Figure 30. Intensity-based image processing example. (a) Dextran-infiltrated PEG scaffold. (b) Binarized image with dextran-filled void space depicted as bright pixels and solid scaffold depicted as dark pixels, Ω=0.502. (imaging depth, 60 μm; scale bar, 250 μm)

3.3.4 MECHANICAL TESTING

The mean compressive modulus and strength for control, bijel-templated, and fibrin-loaded bijel-templated (CBiTH) PEG samples are presented in Table 4. Control PEG specimens exhibited the greatest compressive modulus, as expected of the bulk material. Incorporation of the porous microchannel network resulting from bijel-templating decreased the compressive modulus of bijel-templated PEG scaffolds relative to controls. Fibrin loading in CBiTHs resulted in a slight increase in compressive modulus, compared to the porous PEG scaffold. No statistically significant differences were observed between bijel-templated and CBiTH compressive moduli measurements. Additionally, no statistically significant differences were observed between compressive strength measurements across all sample types.

Table 4. Compressive modulus and strength of cell delivery hydrogels

Sample	Compressive Modulus, E (kPa)	Compressive Strength, σ_u (kPa)
Control PEG	2346.53 ± 10.3%	238.00 ± 3.61%[a]
Bijel-templated PEG	800.67 ± 13.3%[a]	241.33 ± 1.53%[a]
Fibrin-PEG CBiTH	836.07 ± 15.1%[a]	238.33 ± 1.15%[a]

[a]no statistical difference detected between samples ($p > 0.0167$)

3.4 DISCUSSION

We have successfully fabricated composite systems that combine discrete phases of natural and synthetic hydrogels at characteristic length scales relevant to cell loading and migration. Our CBiTHs are comprised of a PEG scaffold which provides a mechanically robust backbone, and a sample-spanning fibrin phase which provides a natural fibrous ECM environment for cell encapsulation. The combinatorial advantages of these composites as cell delivery systems are showcased in the present study using CBiTHs to deliver NHDFs to an acellular fibrin gel in vitro. CBiTHs are structured such that cell loading is achieved uniformly throughout the entire volume, and uniform pore morphology may aid in a milder loading condition in which cells are not subjected to high shear stresses encountered in a random pore morphology. Once loaded, cells exhibit a similar morphology to those encapsulated in control fibrin gels, able to spread in a 3D ECM. The non-constricting, fully percolating microchannel network inside the composite provides ample routes for metabolite transport and allows uninhibited albeit tortuous pathways for cell migration throughout the volume and out of the composite. To further investigate the microchannel network present in bijel-templated PEG scaffolds, a fluorescence-based diffusion analysis was performed using a simple model for transient diffusion. The model fits show good agreement with experimental data. The effective diffusivity extracted from modeling (5.06E-7 cm^2s^{-1}) was comparable to the expected free diffusion of 150 kDa dextran calculated using the Stokes-Einstein equation (3.65E-7 cm^2s^{-1}).[137] The plateau intensity (β=0.84) was greater than the void fraction calculated by thresholding at steady state (Ω=0.502), which can be explained as follows. The axial

resolution of confocal imaging (58 μm as calculated using a numerical aperture of 0.13, wavelength of 488nm, and refractive index of 1)[56] is larger than the domain size in the CBiTH. Therefore, light collected at each pixel will include out of focus fluorescence from regions above and below. Consequently, the solid scaffold regions will not appear completely dark and $\beta > \Omega$.

CBiTHs can be cut, picked up, and transferred without damaging the structure of its hydrogel phases. In this work, we have demonstrated that NHDFs may be seeded in fibrin within the PEG scaffold, moved to a new dish without damage to the composite, and delivered to acellular fibrin in a repeatable fashion. NHDF migration from the CBiTH to the surrounding fibrin clot, captured extensively through time-resolved imaging, indicates that moving the CBiTH sample does not induce significant damage to the cell-encapsulating fibrin matrix. Bijel templates are readily generated through a simple temperature quench. These self-assembled templates, comprised of bicontinuous, fully interpenetrating microscale domains separated by a monolayer of particles, offer a new route to scalable cell delivery systems. Bijel templating can be readily expanded to a larger library of biocompatible hydrogel precursors, with the sole requirement being selective miscibility and preferred partitioning into one of the bijel liquid phases. In the present study, PEG-based CBiTHs were not designed to degrade. However, the bijel templating process can be modified to incorporate hydrolytically and enzymatically degradable moieties to synthesize PEG hydrogels with desired degradation profiles.[138–140] Additionally, silica nanoparticles containing the conjugated RITC fluorophore remain imbedded at the bijel-templated PEG scaffold surface and provide fluorescence during

cell tracking experiments. In further designs for cell delivery in vivo using CBiTHs, these nanoparticles can be removed prior to cell loading through additional processing with hydrofluoric acid as demonstrated in Figure 31.

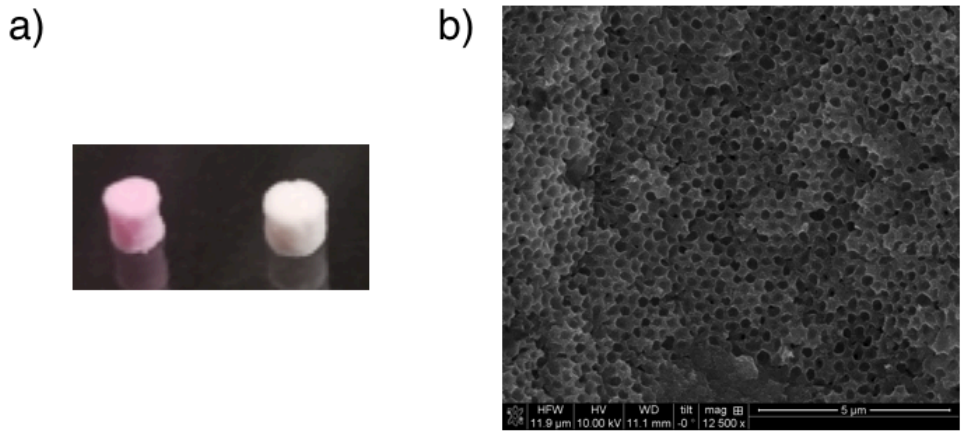

Figure 31. Silica nanoparticle removal achieved through etching with 6M hydrofluoric acid solution overnight. (a) Bijel-templated PEG scaffolds before (*left*) and after (*right*) etching process. (b) SEM micrograph of etched bijel-templated PEG scaffold post-PEDOT casting showing spherical pockets formerly occupied by silica nanoparticles.

3.5 CONCLUSIONS

We report a self-assembly-based synthesis method for a new class of cell delivery composite hydrogels. Bijels afford a robust platform for synthesis of biomaterials containing co-continuous, fully interpenetrating, non-constricting void/polymer phases displaying near-minimal surface geometry. Through fluorescence-based tracking of NHDF migration into acellular fibrin hydrogels, we have demonstrated the utility of CBiTHs as cell delivery systems comprised of a synthetic PEG scaffold and a natural

fibrin seeding matrix. Active migration of NHDFs from CBiTHs was captured via fluorescence microscopy. Image analysis confirmed radial cell density growth in surrounding fibrin over the course of eight days demonstrating cell delivery in a repeatable fashion.

CHAPTER 4. BIJEL-TEMPLATED IMPLANTABLE BIOMATERIALS FOR ENHANCING TISSUE INTEGRATION AND VASCULARIZATION

4.1 INTRODUCTION

As introduced in Chapter 1, biomaterials have found widespread use in tissue regeneration, prosthetics, and implantable devices. The functional lifetime of these biomaterials is largely contingent on the body's ability to integrate or reject a foreign object. The biological process of implant rejection – or the foreign body response (FBR) – has been, and continues to be, studied extensively.[29,141,142]. Following an implantation event, local tissue damage initiates the body's normal wound healing process. Blood proteins and platelets may adsorb to the implant surface leading to an inflammatory cascade of neutrophil investigation and macrophage recruitment, frustrated phagocytosis, formation of multi-nucleated foreign body giant cells (FBGCs), and implant failure as the result of collagen encapsulation.[143,144] Through FBR studies,[25,84,145] a number of controllable factors have been identified that have led to an enriched understanding of tissue integration tools in the design of long-lasting biomaterials.

First, implant surface chemistry dictates immediate protein adsorption and subsequent cell adhesion as hydrophobic surfaces lead to protein unfolding and irreversible adsorption.[146] Hydrophilic surfaces decrease but do not eliminate protein adsorption.[147,148] Polyethylene glycol (PEG), a hydrophilic polymer with long-range repulsion of proteins through tight complexing with water molecules,[149,150] is a commonly investigated material to mitigate the FBR to implants.[151–154] Additionally, zwitterionic surfaces formed with polymers such as carboxybetaine and Sulfobetaine,[155,156]

polyampholytes,[157,158] and poly(N-vinylpyrrolidone) (PVPON)[159,160] have been exploited as biomaterial coatings that provide a neutrally charged surface with minimal protein adsorption. An additional approach to controlling the FBR is achieved through attaching cell receptor ligands to the material to decrease inflammation and increase normal tissue healing around implants.[161] Bioactive signals, such as cluster of differentiation 200 (CD200)[162] and cluster of differentiation 47 (CD47),[163] reduce macrophage infiltration and resist inflammatory cell attachment, respectively. In this approach, the implant is not required to be anti-protein fouling as the ligands interact with responding immune cells. Secondly, implant morphology has been intimately linked to FBR mitigation.[164,165] Microscale features at the implant-tissue interface, independent of material composition, have been shown to inhibit collagen remodeling, in turn disrupting the formation of dense, thick fibrosis that would encapsulate the implant [166]. Materials with controlled local curvature or grooved surfaces have also been implicated in the differentiation of immune cells and the FBR,[108,167,168] while sharp edges and acute angles have previously been shown to promote inflammation.[169,170] In addition to surface microfeatures, the presence of an interconnected microporous network in the material's internal volume may provide a route to tissue integration and infiltration.[171] Vascularization of implantable biomaterials is particularly important for bio-interfacing devices requiring nutrient and waste shuttling to support implanted tissue such as pancreatic islets.[172]

A number of routes exist for imparting porosity to polymeric biomaterials including particle-templating,[100] salt leaching,[129] gas-foaming,[173] electrospinning,[174] cryo-gelation,[128] and emulsion polymerization.[18] These methods can create pore networks with

high degrees of interconnectivity; however, narrow connections (tunnels or windows) between void pockets may disrupt cell migration and full utilization of the void space and random structures with sharp edges or flat surfaces may increase the FBR as discussed above. As described above, bicontinuous interfacially jammed emulsion gels (bijels) offer a robust platform for synthesizing a new class of biomaterials with a fully interpenetrating, non-constricting pore network and negative Gaussian internal surface topology. Bijels, first proposed in computer simulations by Cates *et al*. in 2005[175] and demonstrated experimentally by Herzig *et al*. in 2007 as discussed in Section 2.1,[54] are unique soft materials that form as the result of kinetic arrest of partially miscible fluids undergoing spinodal decomposition. Upon quenching of a suspension comprised of a critical-composition binary fluid mixture and near-neutral wetting nanoparticles (Figure 32a) to unstable thermodynamic conditions via a rapid temperature ramp, the nanoparticles adsorb to the newly formed liquid-liquid interface (Figure 32b) and eventually halt the coarsening process once the interface becomes fully occupied by nanoparticles (Figure 32c), a jamming transition bearing mechanical signatures of a sharp gelation phenomenon.[62,135,176] The resulting bijel comprises bicontinuous, fully percolating fluid domains separated by a nanoparticle monolayer exhibiting negative Gaussian, zero mean curvatures as a result of the minimal surface-based spinodal decomposition process.[20,57,75] Dictated by selective solubility, a monomer added to the formed bijel will partition into one continuous liquid phase, and the morphology is locked in place using photopolymerization of the corresponding phase.[62,75] Bijels have previously been used as

templates for three-dimensional (3D) electrodes,[79] hierarchically porous gold[80] and silver[77] monoliths, cell delivery composites,[78] and separation fibers.[60,61]

Herein, we explore the use of bijels for developing a new class of implantable biomaterials we term bijel-templated materials (BTMs) with increased tissue infiltration and FBR mitigation potential. Bijel-templated polyethylene glycol diacrylate (PEGDA) implants were processed and implanted subcutaneously in nude mice for 28 days and analyzed with histology and immunohistochemistry. BTM implants were compared to particle-templated material (PTM) and non-templated material (NTM) implants made of PEGDA in the same mice to determine the effect of pore network morphology of tissue infiltration and FBR mitigation.

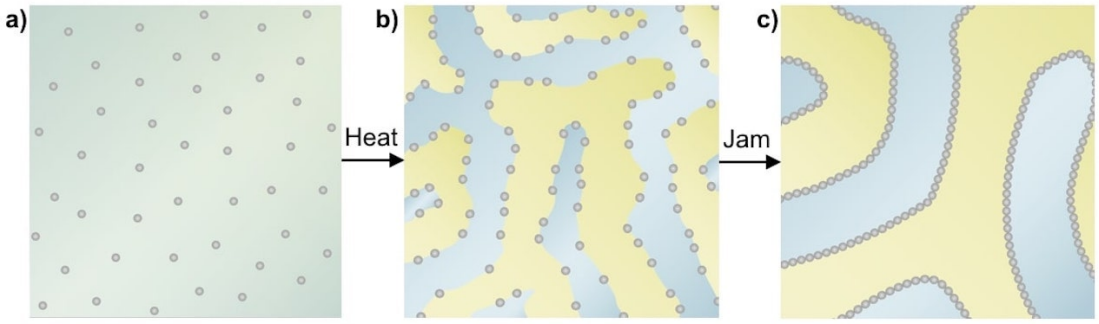

Figure 32. Bijel formation schematic. (a) Particles are dispersed in a critical composition of water and 2,6-Lutidine (x_{Lut} = 0.064). (b) Heating above the lower critical solution temperature (34.1°C) prompts spinodal decomposition and particle adsorption at the coarsening interface. (c) The system jams as the interface becomes completely occupied by particles.

4.2 MATERIALS AND METHODS

4.2.1 PREPARATION OF STUDY IMPLANTS

Bijel-templated material implants. Fluorescently labeled silica nanoparticles (~500 nm) were synthesized following a modified Stöber process[78,136]. Rhodamine B (Sigma-Aldrich) conjugated (3-aminopropyl) triethoxysilane (APTES, TCI America) was mixed overnight with tetraethyl orthosilicate (TEOS, Sigma-Aldrich) in ethanol and strong ammonium hydroxide solution (Fisher Chemical). The synthesized particles were then transferred to 50 mL conical tubes (polypropylene, Greiner), washed by centrifugation (VWR Clinical 200, 2500 rpm, 12 min) and resuspension in deionized water (three cycles), and dried under vacuum (-25 inHg) at 135 ºC. Particles were dried under vacuum to tune surface chemistry until the three-phase contact angle (θ) between Milli-Q water (Millipore, 18.2 MΩ cm at 25ºC), particles, and 2,6-Lutidine (Sigma-Aldrich) reached near-neutral wetting behavior [53]. Such behavior occurs at $\theta \approx 90^{o}$, resulting in zero net curvature at the water/2,6-Lutidine interface [52,177]. Bijels were formed by first dispersing particles (1.5% v/v) in Milli-Q water using an ultrasonic horn (Bronson Sonifier 250, Emerson). The resulting dispersion was mixed with 2,6-Lutidine ($x_{Lut} = 0.064$), placed in a glass cylinder tube (Simax, Mountain Glass Arts, 5 mm inner diameter) attached to a glass coverslip (No. 1, VWR) using polydimethylsiloxane (Sylgard® 186, Dow Corning), and microwaved for 30 seconds to stimulate phase separation and subsequent bijel formation. The vessel was capped with aluminum foil to prevent evaporation and placed in an oven at 70ºC for 5 min. A hydrogel precursor solution of polyethylene glycol diacrylate (PEGDA; number average molecular weight M_n: 258 g/mol, Sigma-Aldrich) and 2-hydroxy-2-

methylpropiophenone photoinitiator (Darocur® 1173, 1% v/v, Ciba Specialty Chemicals) was gently pipetted to the top surface of the bijel. The cylinder was re-capped and returned to the oven for three hours to allow complete transport of the precursor solution into the bijel's lutidine-rich phase. Radical polymerization was then performed to selectively polymerize the corresponding monomer-containing domains and form a microporous PEGDA sample using ultraviolet (UV) light (100 W/cm^2, wavelength: 300-500 nm, Lumen Dynamics). Each BTM implant (3 mm diameter) was cut to a length of 3.5 mm and rinsed three times in isopropyl alcohol to remove the remaining bijel liquids and unreacted precursor reagents. Silica nanoparticles were removed from the samples by performing hydrofluoric acid (HF, Fisher) etching overnight at room temperature. Rhodamine B liberated during silica etching was removed via UV-induced degradation using 1 mg/mL[1] potassium persulfate (Sigma-Aldrich) in Milli-Q water following the procedure outlined in Chen *et al.*[178]. The potassium persulfate solution was replaced every 10 minutes (6 total cycles).

Particle-templated material implants. Poly(methyl methacrylate) particles (PMMA, diameter: 32-38 μm, Cospheric) were fused in the assembled glass cylinders at 180ºC for one hour. Samples were cooled at room temperature for an additional hour, then infiltrated with a solution of PEGDA (36.2% v/v, 1% v/v Darocur® 1173 relative to PEGDA) in 2,6-Lutidine and photopolymerization was performed as described above. The resulting PEGDA-PMMA cylinders (3mm diameter) were submerged in ethyl acetate (Fisher) overnight to remove the PMMA particles, and each resulting PTM implant was cut to a length of 3.5 mm.

Non-templated material implants. PEGDA (36.2% v/v, 1% v/v Darocur® 1173 relative to PEGDA) in 2,6-Lutidine was placed in the assembled glass cylinders and photopolymerization was performed. Each NTM implant (3 mm diameter, 3.5 mm length) was soaked in deionized water overnight at 4ºC to remove 2,6-Lutidine. Implant sterilization. Dry implant samples were sterilized by three 30-minute incubations in 70% ethanol, then rinsed three times in sterile phosphate buffered saline (PBS, Gibco), and dried overnight in a sterile biosafety cabinet at room temperature. Samples were then placed in sterilization pouches and autoclaved (Steris SV-120) at 122ºC for 20 min.

4.2.2 IMPLANT MORPHOLOGY CHARACTERIZATION

Scanning electron microscopy (SEM) was performed on dry implant samples to characterize pore network morphology. Samples were sputter-coated with 6 nm of iridium to reduce charging and micrographs were acquired using a Quanta 3D FEG Dual Beam Microscope (FEI) with an excitation voltage of 10 kV at a 10 mm working distance.

4.2.3 IMPLANTATION

All procedures were approved by the UC Irvine Institutional Animal Care and Use Committee (IACUC #2008-2850). Athymic nude mice (Charles River Laboratories) approximately 8-weeks old weighing between 20 and 25 g were used for this study. Animals were anesthetized with 2% – 4% isoflurane for surgical experiments. Four small incisions, one in each quadrant of the back of the animal, less than one cm in length through the dorsal skin, were created via sterile surgical scissors. Subcutaneous pockets

were created by blunt dissection. Scaffolds were briefly hydrated with sterile saline prior to implantation. A single scaffold was placed within each pocket to prevent movement and potential overlapping of materials during the 4-week study. Implants were placed on their curved edge with the long axis oriented parallel to the spine between the top skin layer and underlying fascia. In other words, the circular flat edges of the cylinders were perpendicular to the top of the skin. The dorsal incisions were closed with surgical clips (Fine Science Tools). The animals received ibuprofen, between 50 and 80 mg/kg, via drinking water for 2 days following surgery. Animals were monitored daily and surgical clips were removed after 14 days. After 28 days, scaffolds and skin samples that received a sham incision were removed and fixed in 4% phosphate-buffered formalin and animals were sacrificed.

4.2.4 TISSUE PROCESSING & IMMUNOHISTOCHEMISTRY

All tissue samples were sent to JIT Labs (Irvine, CA, USA) for processing in paraffin, 4 μm sectioning, and staining with hematoxylin and eosin (H&E) and Masson's Trichrome (MT). Slides were imaged with a Nikon eclipse E800 microscope under 20x magnification (NA: 0.5) using the Olympus "cellSens Entry" program. Images in adjacent fields of view were stitched together using Fiji software.[179,180]

Vessel immunohistochemistry. Following previously described methods,[181] tissue sections were deparaffinized with xylene followed by antigen retrieval via overnight incubation in 0.1 M Tris/HCl buffer, pH 9 at 80°C. Sections were then washed with PBS, permeabilized with 0.5% Triton X-100 (Arcos Organics) and blocked with 5% Donkey

serum (Jackson ImmunoResearch) for 60 min at room temperature. After serum blocking, slides were incubated with 0.5% monoclonal rabbit anti-alpha smooth muscle actin (αSMA, Abcam) for labeling pericytes and 0.5% goat anti-cluster of differentiation 31 (CD31, Santa Cruz Biotechnology) for labeling vessel endothelial cells in PBS supplemented with 5% donkey serum and 0.5% Triton X-100 at 4°C overnight. Slides were then washed with PBS and incubated with 0.2% AlexaFluor488 donkey anti-rabbit (Life Technologies) and 0.25% AlexaFluor594 donkey anti-goat (Jackson ImmunoResearch) in PBS for 1 hour. Counter staining for cell nuclei was performed by incubating slides with 0.03% 4',6-diamidino-2-phenylindole, dihydrochloride (DAPI, Invitrogen) for 10 min.

Macrophage immunohistochemistry. Antigen retrieval was performed by incubating tissue sections in a citrate solution, pH 6 (Dako) in a steam cooker (Black&Decker) for 30 min. Tissue sections were permeabilized and blocked as described above. Slides were then incubated with 1% monoclonal rat anti-F4/80 (BM8, eBioscience) for labeling of all macrophage types[182,183] and 1% polyclonal goat anti-cluster of differentiation 206 (CD206, R&D Systems) for labeling of alternatively activated "M2" macrophages[8,151] in PBS supplemented with 5% Donkey serum and 0.5% Triton X-100 at 4°C overnight. Slides were washed with PBS and incubated with 0.25% AlexaFluor488 donkey anti-rat (Life Technologies) and 0.25% AlexaFluor594 donkey anti-goat (Jackson ImmunoResearch). Counter staining for cell nuclei was performed by incubating all slides with 0.03% DAPI (Invitrogen) for 10 minutes.

4.2.5 VESSEL QUANTIFICATION

Fluorescence microscopy was performed on processed tissue slides labeled for αSMA and CD31 using an Olympus IX83 microscope under 20x magnification (NA: 0.45) using an Orca R2 camera (Hamamatsu Photonics K.K.) and Micro-Manager [184]. Images were acquired for the full BTM and PTM samples in a single section, and a composite image was created by image stitching in Fiji. CD31+ vessel boundaries were traced by hand and used to calculate vessel area and centroid distance to the nearest implant boundary using custom scripts written in MATLAB (MathWorks). Only vessels that resided wholly within the template material were counted.

4.2.6 MACROPHAGE QUANTIFICATION

Laser scanning confocal microscopy was performed on processed tissue slides labeled for F4/80 and CD206 using an Olympus IX81 inverted microscope under 40x magnification (NA: 0.6) equipped with a FluoView 1200 laser scanning system and software. Laser wavelengths (λs) of 405 nm, 488 nm, and 559 nm were used to excite DAPI (cell nucleus), AlexaFluor488 (F4/80 macrophage marker label), and AlexaFluor594 (CD206 pro-healing macrophage marker), respectively. Fluorescent emissions from the three fluorophores were detected separately using photomultiplier tubes (PMTs). Specifically, a first dichroic (maximum λ: 490 nm) and barrier filter (λ: 430 – 470 nm) reflected and filtered DAPI emissions for detection in PMT 1. A second dichroic (maximum λ: 560 nm) and barrier filter (λ: 505 – 540 nm) reflected and filtered AlexaFluor488 emissions for detection in PMT 2. Lastly, a mirror and barrier filter (575 – 675 nm)

reflected and filtered the remaining AlexaFluor594 emissions for detection in PMT 3. F4/80+ and CD206+ cells were counted in images acquired along the implant interface (0 – 300 μm deep from the interface) using Fiji's cell counter plugin and the percentage of F4/80+ cells also positive for CD206 was calculated. Seven images per implant type per mouse were processed for macrophage quantification.

4.2.7 SECOND HARMONIC GENERATION

Second harmonic generation (SHG) imaging was performed on non-labeled tissue sections for a qualitative view of collagen deposition. An inverted Zeiss LSM-780 multi-photon confocal microscope was used for SHG imaging. To increase the efficiency of SHG photon detection, a mirror was placed on top of the tissue slide to back-reflect the forward-scattered light.

4.2.8 STATISTICAL ANALYSIS

Two-sample t-tests for individual mouse data and a matched paired t-test for the combined data were used to compare macrophage phenotype differences by implant type. The two sample Kolmogorov-Smirnov test was used to compare vessel area by implant type. All statistical tests were performed in OriginPro (OriginLab) with $p < 0.05$ considered a statistically significant difference between implant types.

4.3 RESULTS

4.3.1 IMPLANT MORPHOLOGY

Representative implant sample SEM micrographs are shown in Figure 33. BTM implants (Figure 33a) displayed the distinct morphological features of their parent bijel template including a fully interpenetrating, non-constricting pore network and a polymer surface with relatively uniform, negative Gaussian curvature. PTM implants (Figure 33b) displayed spherical pores, connected via smaller pore windows (presenting as dark circles) as a result of the partial fusing of the template particles. A superimposed red circle with a diameter of 32 μm is shown in Figure 33a,b to demonstrate matching pore sizes between the two templated implants. The solid, NTM implant (Figure 33c) did not display any porous morphology, as expected.

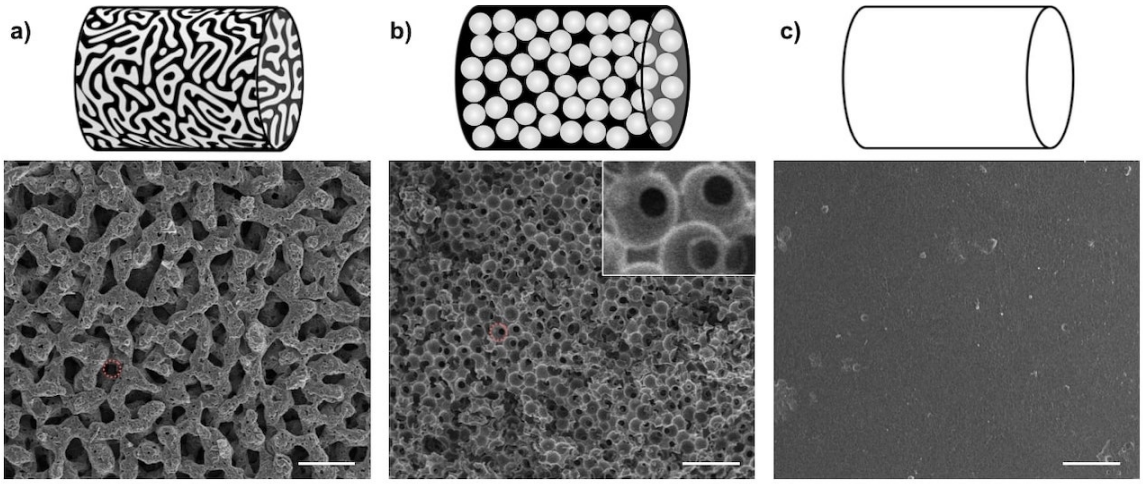

Figure 33. Template materials and scanning electron microscopy micrographs of polymer implants. Pictured are (a) BTM, (b) PTM, and (c) NTM polyethylene glycol diacrylate implants. Scale bar, 100 μm. Superimposed red circle diameter in panels a and b, 32 μm.

4.3.2 HISTOLOGY & SECOND HARMONIC GENERATION

Representative images of tissue section slides processed with H&E and MT for histology and SHG are shown in Figure 34. Cellular infiltrate, identified by hematoxylin-stained cell nuclei (violet), was observed deep (>500 μm from the implant-tissue

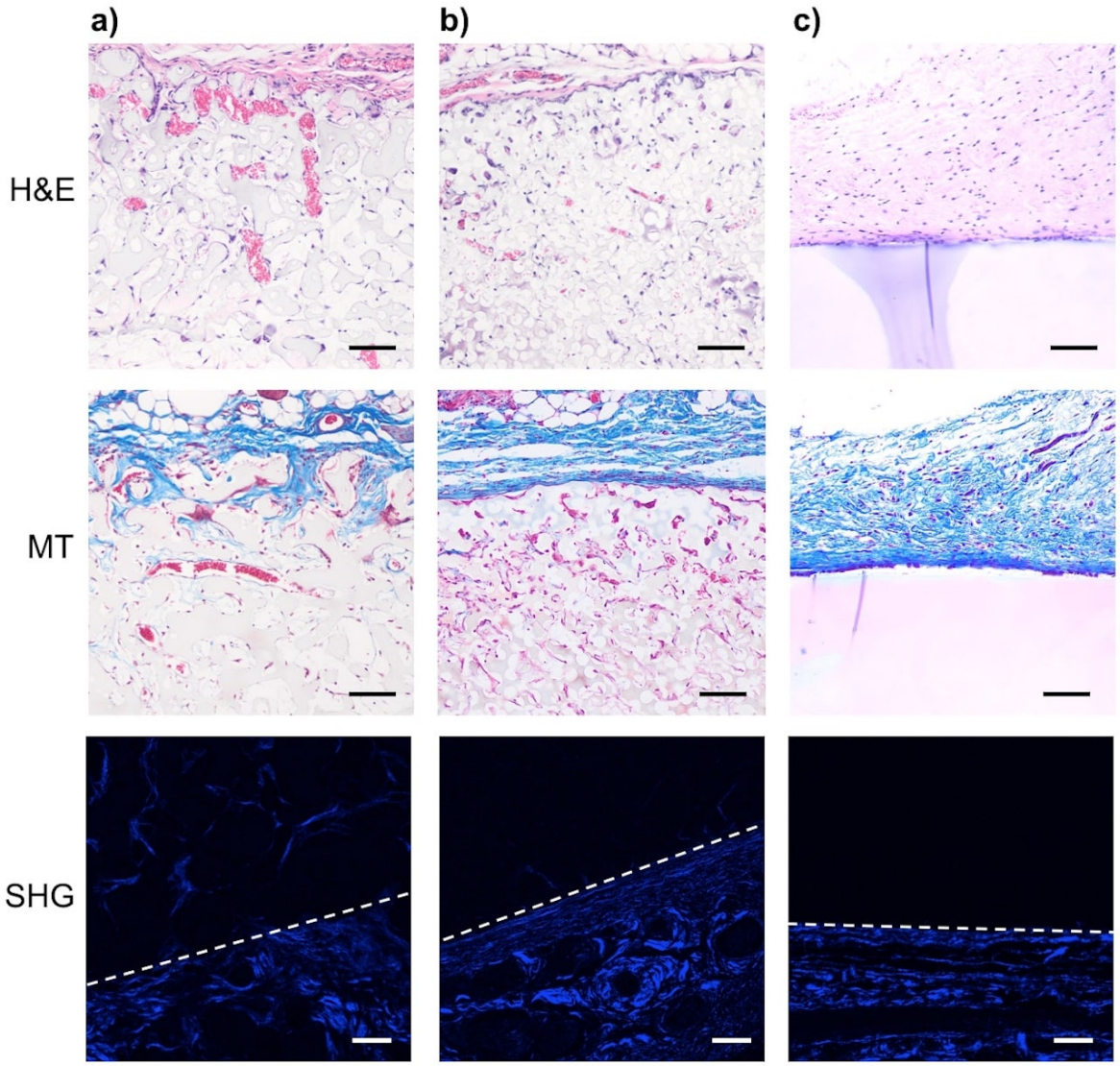

Figure 34. Histology and second harmonic generation (SHG) of BTM (a), PTM (b), and NTM (c) implants. Histology sections stained with hematoxylin and eosin (H&E) shown in row 1 and Masson's trichrome (MT) shown in row 2. Scale bar, 100 μm. Sections imaged using second harmonic generation (SHG) shown in row 3. White dashed line denotes tissue-implant boundary with implant oriented on top. Scale bar, 50 μm.

boundary) in the porous implant materials (Figure 34a-b). Infiltrate is present throughout the entire pore network in the BTM sample. Conversely, no infiltrate was present in several areas of the PTM pore network. No infiltrate was observed for the solid, NTM sample. Blood vessels were present in both porous samples. Blood vessels were observed spanning the entire pore diameter in the BTM sample, while the vessels within the PTM sample were noticeably thinner. Collagen at the implant-tissue interface was oriented parallel to the interface of PTM and NTM implants, a feature not observed in the BTM implants. Further, a diffuse collagen network was observed within the BTM pores as evidenced by a slightly lighter, broken MT collagen stain (blue). For comparison to native tissue not exposed to an implant, histology of the sham incision experiment is included in Figure 35. Further qualitative analysis of collagen deposition in the tissue at the implant-tissue interface by SHG showed a dimmer signal with a lower degree of orientation for the BTM sample (Figure 34a) relative to the PTM (Figure 34b) and NTM (Figure 34c) samples.

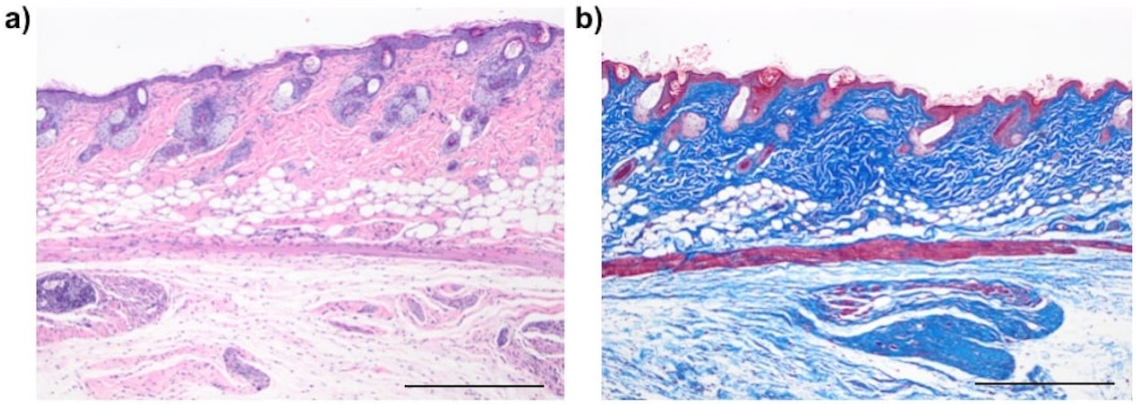

Figure 35. Sham incision skin stained with H&E (a) and Masson's Trichrome (b). Scale bar, 500 μm.

4.3.3 VESSEL IMAGING & QUANTIFICATION

Confocal microscopy images of αSMA- and CD31-labeled tissue sections are shown in Figure 36. Vessels within the pore network of BTM implants (Figure 36a) were often αSMA+ and CD31+, indicating mature vessels bounded by pericytes for stabilization and regulation of the microvasculature.[185] Similar to histology results, vessels often completely occupied the pore network in the BTM sample. Conversely, thin vessels were formed within the PTM implants (Figure 36b), some of which were not αSMA+. Scatterplots of vessel section area versus distance to nearest tissue-material boundary within the implant samples are shown for the BTM (Figure 36c) and PTM (Figure 36d). Two observations were made. First, in the region near the boundary (<400 μm), both materials have vessels, however the vessel section area in the BTM was much larger, as the morphology permits (Figure 36e,f). Second, at depths beyond 400 μm the PTM exhibited just a few small vessels resulting in the low vessel section area, whereas the BTM continues to contain large vessels out to 800 μm. Not plotted is a vessel section extending from the boundary into a BTM implant growing to over 22,000 μm^2 (Figure 37).

4.3.4 MACROPHAGE IMAGING & QUANTIFICATION

Confocal microscopy images of tissue section slides labeled for F4/80, pan-macrophage, and CD206, “M2 pro-healing” macrophage, markers are shown in Figure 38. F4/80+ cells were scattered throughout the pore network within the BTM implant (Figure 38a), many adhered to the implant material leaving much of the pore volume unoccupied. In contrast, F4/80+ cells, where present, occupied a large portion of

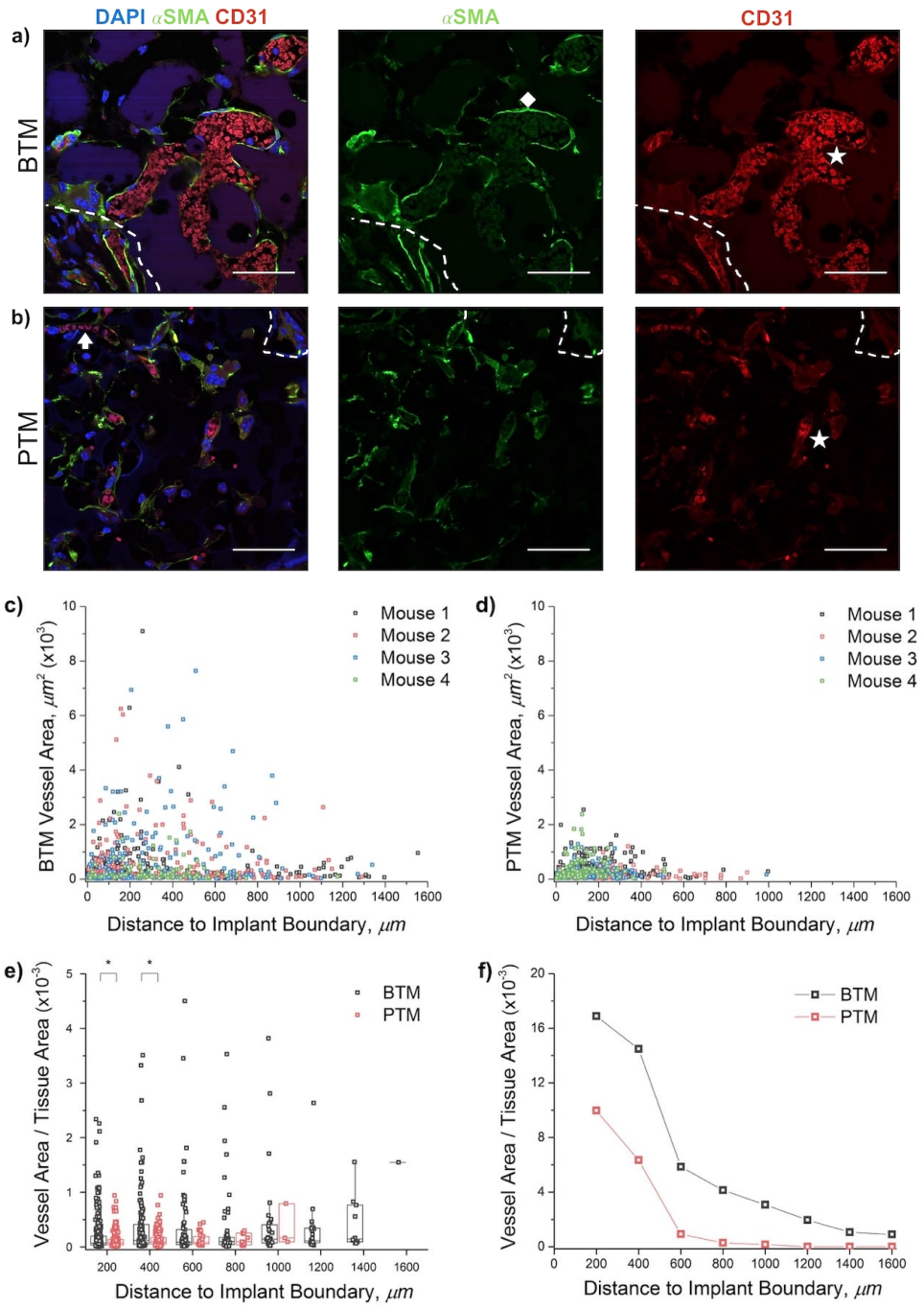

Figure 36. Vessel immunohistochemistry and quantification. Shown are CD31 (red), αSMA (green), and DAPI (blue) labeling in BTM (a) and PTM (b) implants. DAPI counterstaining shown in blue. Dashed lines denote implant boundary, an arrow denotes a thin vessel extending through pore-pore windows, a diamond denotes a αSMA+ cell, and stars denote CD31+ cells. Scale bar, 50 μm. Vessel area versus distance to nearest implant boundary in BTM (c) and PTM (d) implants. Vessel area per binned tissue area versus distance to boundary (200 μm per bin) grouped by implant type by individual (e) and total (f) vessels. *$p < 0.05$

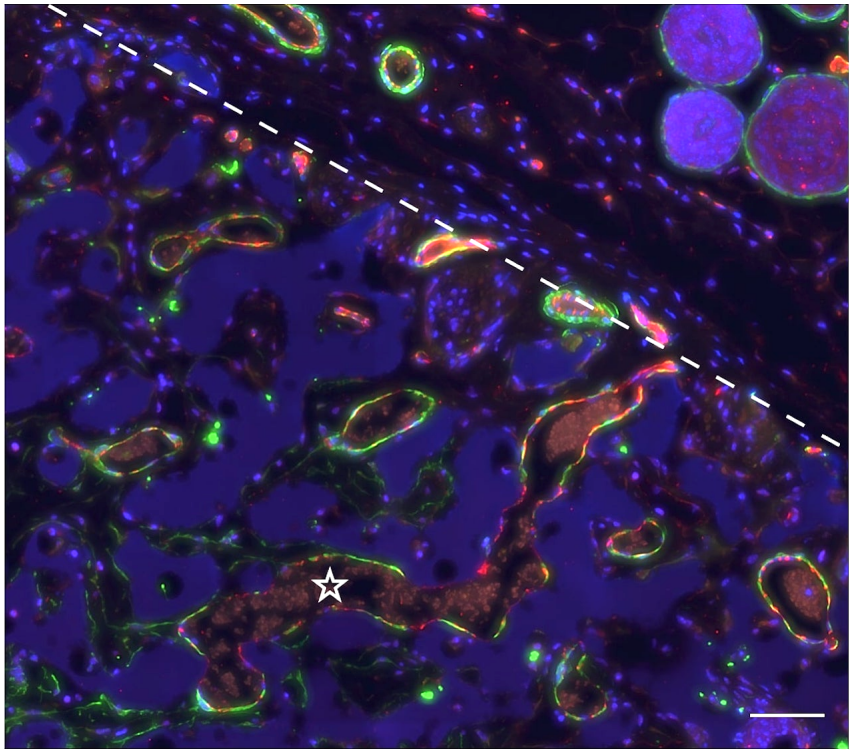

Figure 37. Vessel IHC demonstrating penetration in a BTM implant. α-SMA in pericytes and myofibroblasts labeled in green, CD31 in endothelial cells labeled in red, and cell nuclei labeled in blue (DAPI). Pericytes at vessel walls in the BTM indicate mature vasculature. Implant-tissue interface: dashed white line. Largest vessel observed (~22,000 μm^2) in study denoted by white star. Scale bar, 50 μm.

the pore network within the PTM implant (Figure 38b). Also, multi-nucleated cells, which may be foreign body giant cells, were observed that tended to be F4/80+ CD206-. The CD206 macrophage polarization marker was present in roughly 75% compared to 46% of the F4/80+ cells counted in the BTM and PTM implants, respectively (Figure 38c-d).

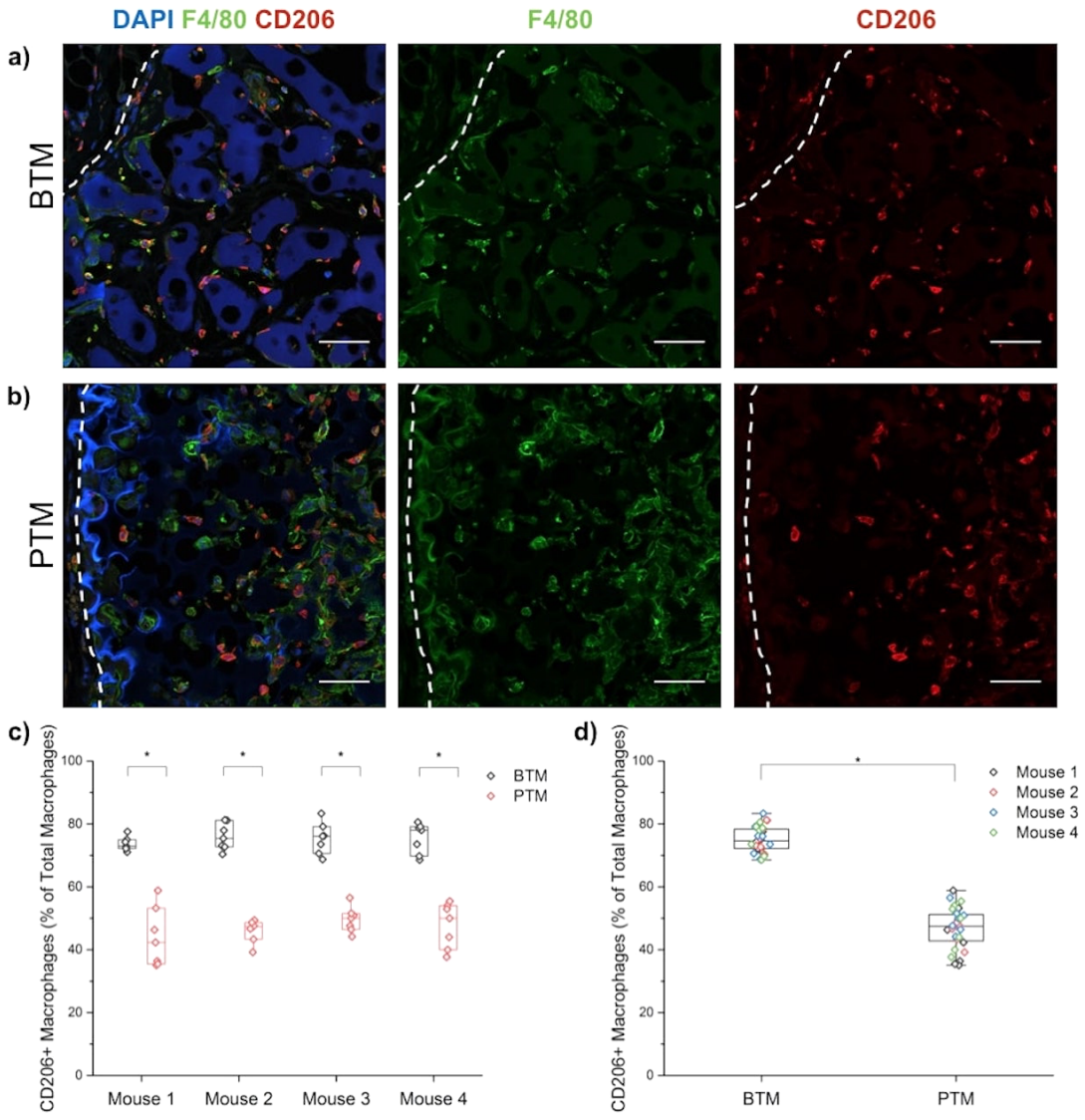

Figure 38. Macrophage immunohistochemistry and quantification. Shown are F4/80 (green) and CD206 (red) labeling in BTM (a) and PTM (b) implants. DAPI counterstaining shown in blue. Dashed lines denote implant boundary. Scale bar, 50 μm. Percent CD206+ cells relative to total F4/80+ cells for both implant types in each mouse (c-d). *$p < 0.05$.

4.4 DISCUSSION

Biomaterials templated using bijels were implanted in mice and the tissue response to the implants was analyzed after 4 weeks. To our knowledge, this is the first time a bijel has been investigated as a template for potential biomaterials or devices. Our tissue analysis revealed that BTM implants were not rejected as a result of the foreign body response as full collagenous encapsulation was not present at the implant-tissue interface. In fact, evidence suggests a shift toward a more pro-healing wound response as diffuse collagen was deposited at the implant surface and within the pore network. PTM implants were also analyzed in the same animal to provide a comparison to a class of porous biomaterial used as a coating for reducing FBR to implants,[165] a drainage implant for glaucoma,[32] an infection resistant percutaneous device,[186] and a proangiogenic tissue engineering scaffold.[7] Qualitatively, a more pronounced collagen capsule was observed at the implant-tissue interface of the PTM implants with little evidence of collagen deposition within the pore network. Immunohistochemical analysis of sectioned implants revealed a stark difference in the native tissue's ability to utilize the pore networks of the two porous implants. Specifically, the non-constricting nature of the BTM implant allowed blood vessels to not only form and occupy the entire micro-channel diameter, snaking along the curved interface (Figure 36a), but also reside deep within the implant (Figure 36c). Pericytes bounding the vessels indicated that many of the large vessels within the BTM implant were mature in nature and would remain indefinitely. In contrast, the constricting windows connecting adjacent pores of the PTM implant force vessels to narrow, often leaving much of the pore volume vacant. In some cases, red

blood cells were observed in single file inside narrow vessels (arrow Figure 36b), severely limiting blood flux in those areas of the implant. Both porous implant types were infiltrated with macrophages (F4/80+). Macrophages appeared scattered throughout the pore network of the BTM implants, while in PTM implants, they appeared to fully occupy pores within roughly five pore lengths from the tissue-implant interface. The polarization marker CD206 indicated a difference in macrophage polarization within the two porous implant types, as the BTM case directed more of the alternately activated, “M2 pro-healing” phenotype.

Implants for this study were synthesized from the same non-fouling material, PEGDA. Even with its unique protein repulsive properties, the NTM PEGDA implants triggered the FBR as evidenced by collagen encapsulation (Figure 34c) and F4/80+ CD206- cells at the implant-tissue interface (Figure 39). Differences in the tissue response are therefore attributed primarily to the implant microstructure. Importantly,

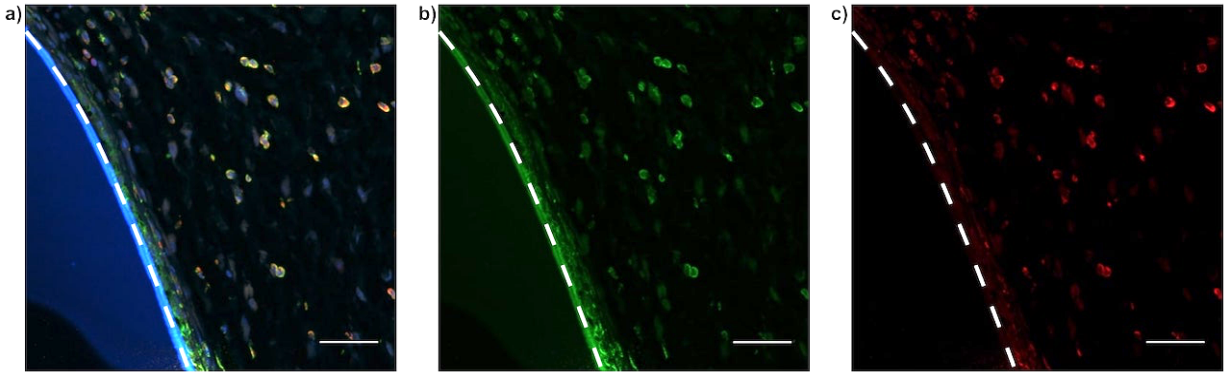

Figure 39. Macrophage immunohistochemistry for NTM PEGDA implant. Green: F4/80, red: CD206, blue: DAPI. Composite image shown in (a), F4/80-only shown in (b), and CD206-only shown in (c). Dashed lines denote implant boundary. Scale bar, 50 μm.

bijels self-assemble during spinodal decomposition, a phase separation process marked by dynamically self-similar, bicontinuous, fully percolating fluid domains [57]. The resulting energetically preferred minimum surface area interface displays negative Gaussian, zero mean (hyperbolic or saddle) curvature. These attributes are transferred to the templated PEGDA implants resulting in pore networks that do not constrict, do not have any "dead ends," with a surface displaying hyperbolic curvature. In our study, the consistent pore size allowed large vessels to penetrate deep within the BTM implants (Figure 36c). In contrast, the particle templating process relies on varying degrees of sphere fusion, which imparts pores having narrow interconnected windows upon template removal. The pore surfaces within this material display predominately positive Gaussian curvature. We find that the narrow windows within the pore network of PTM implants limits the size of penetrating vasculature. The constrictions may also play a role in the nature of the tissue infiltration as pores were often packed with F4/80+ cells. Cell migration is stunted by the constricting nature of the pore windows [19], which may influence macrophage polarization. In contrast, cells are allowed in infiltrate the labyrinth-like pore network of BTM implants unobstructed by constrictions. Allowing macrophages and other native cells to infiltrate without obstruction may lead to significant delay or prevention of a fibrotic capsule, thereby extending the lifetime of an implantable device, such as one designed to infuse a therapeutic.

Feature curvature has more recently been investigated in the context of cell adhesion, differentiation, and migration.[105–107] These studies have shown that the cell's apical stress fibers orient parallel to the direction of cell migration on substrates with a

zero Gaussian curvature (e.g. cylinders or flat surfaces). In contrast, on substrates that possess a negative Gaussian curvature (saddle surfaces), the stress fibers orient perpendicular to the direction of cell migration. Therefore, the predominance of negative Gaussian curvatures on the internal surfaces of BTM implants is expected to markedly influence cell-substrate interactions within these materials. Interestingly, macrophages in BTM implants adhered to negative Gaussian curvature surfaces were mostly polarized to the pro-healing phenotype, whereas macrophages adhered to PTM pore surfaces, having mostly positive curvature, had a higher occurrence of the pro-inflammatory phenotype, observed previously by others.[165] The specific implications of curvature's effect on macrophage phenotype and ultimate implant fate are being further explored, but the results presented in this study indicate that our negative Gaussian curvature biomaterials increase implant integration in subcutaneous host tissue. Therefore, our study introduces a new paradigm for biomaterials design based primarily on 3D morphological cues, which are created in bulk using our robust bijel templating method. Through modification of biodegradability, surface chemistry, or bioactive signals, bijel templating could provide a very attractive new class of biomaterials for practical application.

4.5 CONCLUSIONS

We report using bijels as a template platform to create a new class of uniquely structured biomaterial implants with favorable tissue response properties. Our implants comprise a fully penetrating, non-constricting pore network and a negative Gaussian surface. PEGDA BTMs were implanted in athymic mice for four weeks. The morphological

properties of the BTM implants resulted in scattered cellular infiltrate, disorganized low-density collagen deposition, increased vessel size both near the implant surface and deep within, and increased percentage of “M2 pro-healing” polarized macrophages. Overall, these factors indicate an increased integration with host tissue primarily based on the 3D morphological cues inherent to BTM implants. We have proposed future studies to investigate the tissue integration effects of these materials in immunocompetent animals to assess if tissue responses are similar when subjected to the adaptive immune response.

4.6 CONTINUING WORK

To meet the unmet need for reliable, long-lasting insulin infusion sets (IISs) discussed in Chapter 1.3, we are actively developing a new IIS paradigm in which the cannula is filled with a BTM, which also protrudes from the tip. Using this design, the protrusion is the site of beneficial tissue integration and the interconnecting pore network existing in the BTM allows flow distribution in case a portion of the protrusion is blocked. The tissue integration aspect includes deep vascularization and FBR mitigation for direct uptake of infused insulin to the vasculature and prolonged lifetime, respectively. Important to the development of the BTM-integrated IIS is the ability to bond materials to the polytetrafluoroethylene (PTFE, Teflon®) cannula. Etching of PTFE tubes is achieved using sodium naphthalene, which effectively removes fluorene atoms from the polymer backbone. The resultant exposed carbon atoms are now available for radical polymerization routes as discussed in Figure 14. This method has been demonstrated

using UV-initiated radical polymerization of PEGDA BTMs to outer lumen-etched PTFE materials (Figure 40a). This bonding method will be translated for the BTM-loaded IIS cannula, in which the inner luminal surface of the cannula is etched PTFE (Figure 40b).

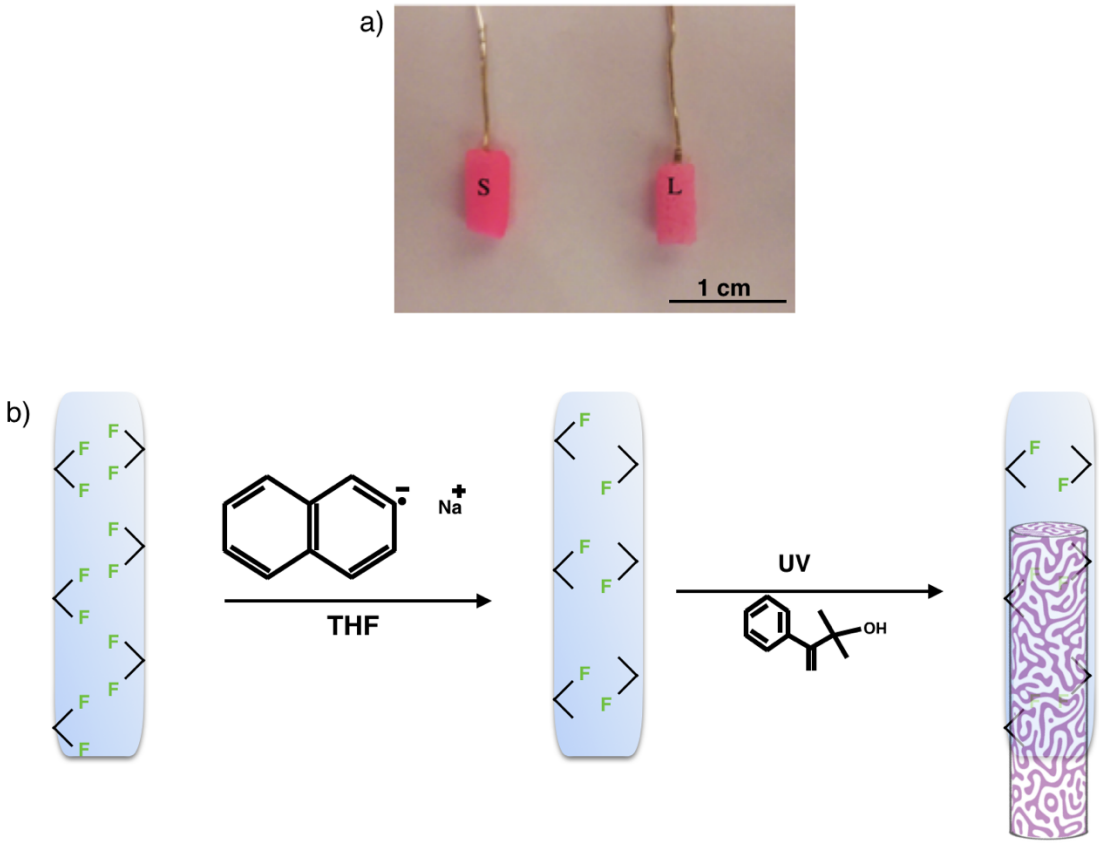

Figure 40. Etched PTFE bonding to PEG BTMs. a) Demonstration of outer lumen-etched PTFE to PEGDA BTMs with small (~20 μm, S) and large (~100 μm, L) pore size and b) reaction schematic for constructing a BTM-integrated IIS cannula in which fluorine atoms are etched from the PTFE chain with sodium naphthalene in THF and UV-initiated radical polymerization of PEGDA to the etched PTFE. Darocur® 1173 photo-initiator is used.

CHAPTER 5. CONCLUSIONS AND FUTURE WORK

5.1 CONCLUSIONS

The self-assembled bijel offers a robust soft gel template for processing morphologically distinct porous materials. In this dissertation work, bijel processing techniques were used to develop a new class of biomaterials. Gelatin methacrylate (gelMA), sulfobetaine methacrylate (SBMA), and instant processing of a multi-acrylated polyethylene glycol were introduced in Chapter 2 as new bijel-derived hydrogels. Polyethylene glycol diacrylate (PEGDA) scaffolds processed from bijels were highlighted in Chapter 3 for creating fibrin-PEGDA composite materials having interconnected, uniform, non-constricting pore channels which enabled cell seeding in a soft 3D natural environment, uninhibited cell migration throughout the scaffold, and facile delivery. In Chapter 4, an investigation into using bijel-processed PEGDA hydrogels as long-term implantable biomaterials that promote healthy tissue integration and dissuade the foreign body response was carried out, demonstrating deep vascularization and a pro-healing tissue response when compared to a commonly used pore-templated biomaterial. Building upon positive findings from this study, a new paradigm for insulin infusion set cannulas was introduced in which a bijel-processed hydrogel is incorporated within the lumen of existing devices.

5.2 FUTURE WORK

The bijel processing method used throughout this work to introduce a morphologically distinct class of biomaterials is inherently amenable to many chemistries

relevant to tissue engineering scaffolds and implantable devices. In a sense, we have only just scratched the surface of available biomaterial chemistries and as such, additional screening of biodegradable, immunomodulatory, pH-, light-, and temperature-sensitive materials is recommended. The development of our BTM-integrated insulin infusion set cannula is an ongoing project that we are currently seeking funding to extensively perform such a biomaterials screen for processing, degradation, and tissue integration properties. Further, bijel processing methods – including the instant processing method presented in Chapter 2.2.5 – are not limited to just insulin infusion sets. Coating other implantable devices, such pancreatic tissue implants and other complex organ replacement therapies that rely heavily on host vascularization and favorable tissue response to achieve long-term viability should be considered.

6. APPENDIX

6.1 ADDITIONAL CELL DELIVERY TESTS

a)

b)

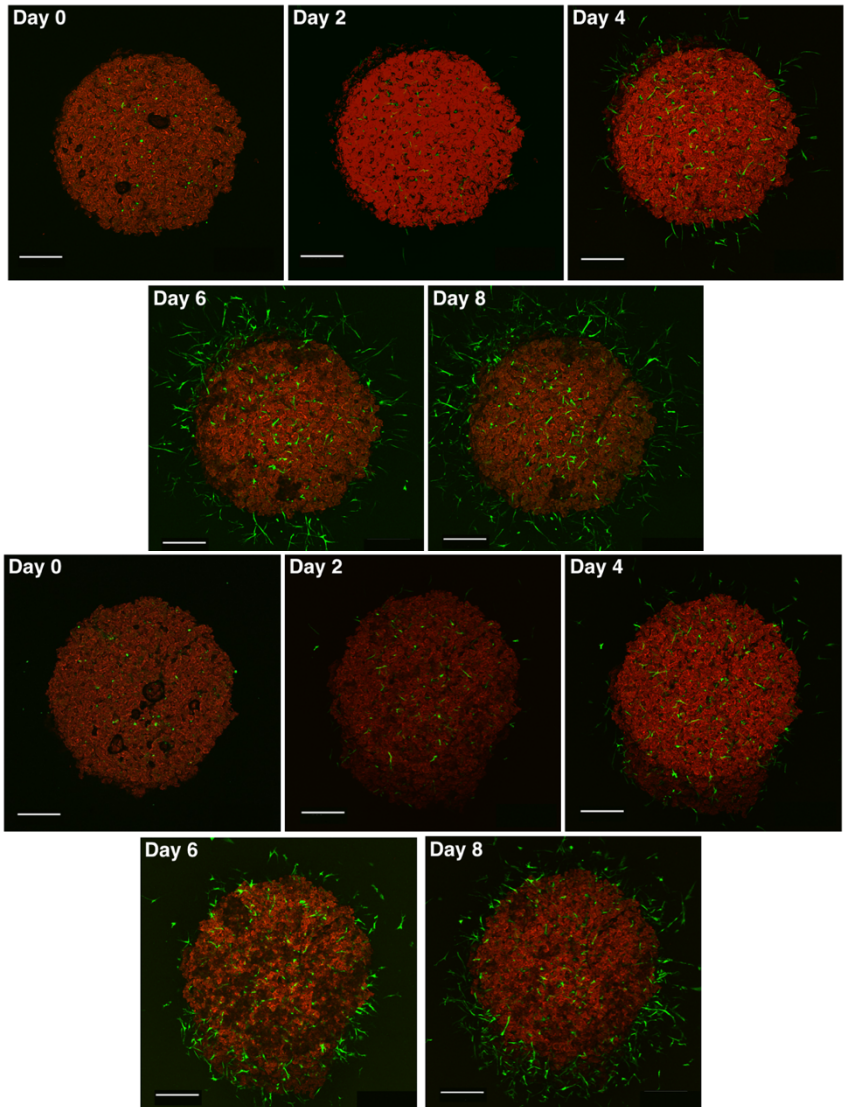

Figure 41. Time-lapse analysis of cell delivery to acellular fibrin hydrogels using NHDF-loaded CBiTHs for Sample 2 (a) and Sample 3 (b). Confocal microscopy maximum intensity projections tracking NHDF delivery over 8 days (green, GFP expression in NHDFs; red, RITC-labeled silica nanoparticles; scale bar, 500 μm). Image stack depth for all panels is 750 μm with the exception of (a) and (b) day 0, 250 μm and (b) day 6, 700 μm.

REFERENCES

1. Ratner, B. D., Hoffman, A. S., Schoen, F. J. & Lemons, J. E. *Biomaterials Science. An Introduction to Materials in Medicine*. (Academic Press, 2013).
2. Rabkin, E. & Schoen, F. J. Cardiovascular tissue engineering. *Cardiovasc. Pathol.* **11,** 305–317 (2002).
3. Rosen, P. in *Ophthalmic Surgery: Principles and Practice* (Elsevier, 2012).
4. Scotchford, C. A., Evans, M. & Vats, A. in *Basic Clinical Radiobiology* 384 (CRC Press, 2016).
5. Nih, L. R., Gojgini, S., Carmichael, S. T. & Segura, T. Dual-function injectable angiogenic biomaterial for the repair of brain tissue following stroke. *Nat. Mater.* **17,** 1–10 (2018).
6. Li, Y., Meng, H., Liu, Y. & Lee, B. P. Fibrin Gel as an Injectable Biodegradable Scaffold and Cell Carrier for Tissue Engineering. *Sci. World J.* **2015,** 1–10 (2015).
7. Madden, L. R. *et al.* Proangiogenic scaffolds as functional templates for cardiac tissue engineering. *Proc. Natl. Acad. Sci. U. S. A.* **107,** 15211–6 (2010).
8. Dollinger, C. *et al.* Controlling Incoming Macrophages to Implants: Responsiveness of Macrophages to Gelatin Micropatterns under M1/M2 Phenotype Defining Biochemical Stimulations. *Adv. Biosyst.* **1,** 1700041 (2017).
9. Annabi, N. *et al.* Controlling the Porosity and Microarchitecture of Hydrogels for Tissue Engineering. *Tissue Eng. Part B Rev.* **16,** 371–383 (2010).
10. Gauvin, R. *et al.* Microfabrication of complex porous tissue engineering scaffolds using 3D projection stereolithography. *Biomaterials* **33,** 3824–3834 (2012).
11. Lewis, J. A. Direct Ink Writing of 3D Functional Materials. *Adv. Funct. Mater.* **16,** 2193–2204 (2006).
12. Sullivan, D. C., Repper, J. P., Frock, A. W., McFetridge, P. S. & Petersen, B. E. Current Translational Challenges for Tissue Engineering: 3D Culture, Nanotechnology, and Decellularized Matrices. *Curr. Pathobiol. Rep.* **3,** 99–106 (2015).
13. Loh, Q. L. & Choong, C. Three-Dimensional Scaffolds for Tissue Engineering Applications: Role of Porosity and Pore Size. *Tissue Eng. Part B Rev.* **19,** 485–502 (2013).
14. Place, E. S., George, J. H., Williams, C. K. & Stevens, M. M. Synthetic polymer scaffolds for tissue engineering. *Chem. Soc. Rev.* **38,** 1139–1151 (2009).
15. Peppas, N. A., Hilt, J. Z., Khademhosseini, A. & Langer, R. Hydrogels in Biology and Medicine: From Molecular Principles to Bionanotechnology. *Adv. Mater.* **18,** 1345–1360 (2006).
16. Buwalda, S. J. *et al.* Hydrogels in a historical perspective: From simple networks to smart materials. *J. Control. Release* **190,** 254–273 (2014).
17. Marshall, A. J., Alvarez, M. & Maginness, M. Implantable Medical Devices Having Microporous Surface Layers and Method for Reducing Foreign Body Response to the Same. (2013).
18. Nalawade, A. C. *et al.* Inverse high internal phase emulsion polymerization (i-HIPE) of GMMA, HEMA and GDMA for the preparation of superporous hydrogels as a tissue engineering scaffold. *J. Mater. Chem. B* **4,** 450–460 (2016).

19. Stachowiak, A. N. & Irvine, D. J. Inverse opal hydrogel-collagen composite scaffolds as a supportive microenvironment for immune cell migration. *J. Biomed. Mater. Res. Part A* **85A,** 815–828 (2008).
20. Chen, H.-Y., Kwon, Y. & Thornton, K. Multifunctionality of three-dimensional self-assembled composite structure. *Scr. Mater.* **61,** 52–55 (2009).
21. Qin, Z., Jung, G. S., Kang, M. J. & Buehler, M. J. The mechanics and design of a lightweight three-dimensional graphene assembly. *Sci. Adv.* **3,** e1601536 (2017).
22. Kapfer, S. C., Hyde, S. T., Mecke, K., Arns, C. H. & Schröder-Turk, G. E. Minimal surface scaffold designs for tissue engineering. *Biomaterials* **32,** 6875–6882 (2011).
23. Martina, M. *et al.* Developing macroporous bicontinuous materials as scaffolds for tissue engineering. *Biomaterials* **26,** 5609–5616 (2005).
24. Torres-Rendon, J. G. *et al.* Bioactive Gyroid Scaffolds Formed by Sacrificial Templating of Nanocellulose and Nanochitin Hydrogels as Instructive Platforms for Biomimetic Tissue Engineering. *Adv. Mater.* **27,** 2989–2995 (2015).
25. Onuki, Y., Papadimitrakopoulos, F., Bhardwaj, U. & Burgess, D. J. A Review of the Biocompatibility of Implantable Devices: Current Challenges to Overcome Foreign Body Response. *J. Diabetes Sci. Technol.* **2,** 1003–1015 (2008).
26. Hansson, U., Blunn, G. & Ryd, L. Histologic reactions to particulate wear debris in different mesenchymal tissues. *J. Arthroplasty* **19,** 481–487 (2004).
27. Handel, N. The Effect of Silicone Implants on the Diagnosis, Prognosis, and Treatment of Breast Cancer. *Plast. Reconstr. Surg.* **120,** 81S–93S (2007).
28. Ludwig, B. *et al.* Transplantation of human islets without immunosuppression. *Proc. Natl. Acad. Sci.* **110,** 19054–19058 (2013).
29. Anderson, J. M., Rodriguez, A. & Chang, D. T. Foreign body reaction to biomaterials. *Semin. Immunol.* **20,** 86–100 (2008).
30. Hauzenberger, J. R. *et al.* Systematic in vivo evaluation of the time-dependent inflammatory response to steel and Teflon insulin infusion catheters. *Sci. Rep.* **8,** 1132 (2018).
31. Leigh, B. L. *et al.* Photopolymerizable Zwitterionic Polymer Patterns Control Cell Adhesion and Guide Neural Growth. *Biomacromolecules* **18,** 2389–2401 (2017).
32. Pourjavan, S. *et al.* STARflo: A Suprachoroidal Drainage Implant Made from STAR Biomaterial. *Surg. Innov. Glaucoma* 235–251 (2014).
33. Heinemann, L. & Krinelke, L. Insulin Infusion Set: The Achilles Heel of Continuous Subcutaneous Insulin Infusion. *J. Diabetes Sci. Technol.* **6,** 954–964 (2012).
34. Heinemann, L., Walsh, J. & Roberts, R. We Need More Research and Better Designs for Insulin Infusion Sets. *J. Diabetes Sci. Technol.* **8,** 199–202 (2014).
35. Pfützner, A. *et al.* Using Insulin Infusion Sets in CSII for Longer Than the Recommended Usage Time Leads to a High Risk for Adverse Events: Results From a Prospective Randomized Crossover Study. *J. Diabetes Sci. Technol.* **9,** 1292–1298 (2015).
36. Thethi, T. K. *et al.* Consequences of delayed pump infusion line change in patients with type 1 diabetes mellitus treated with continuous subcutaneous. *J. Diabetes Complications* **24,** 73–78 (2010).

37. Forst, T., Pfützner, A. & Ph, D. Pilot Study for Assessment of Optimal Frequency for Changing Catheters in Insulin Pump Therapy—Trouble Starts on Day 3. *J. Diabetes Sci. Technol.* **4,** 976–982 (2010).
38. Ziegler, A., Williams, T., Yarid, N., Schultz, D. L. & Bundock, E. A. Fatalities Due to Failure of Continuous Subcutaneous Insulin Infusion Devices: A Report of Six Cases. *J. Forensic Sci.* (2018). doi:10.1111/1556-4029.13841
39. Heinemann, L. *et al.* Insulin Pump Risks and Benefits: A Clinical Appraisal of Pump Safety Standards, Adverse Event Reporting, and Research Needs A Joint Statement of the European Association for the Study of Diabetes and the American Diabetes Association Diabetes Technology W. *Diabetes Care* **38,** 716–722 (2015).
40. Stratford, K., Adhikari, R., Pagonabarraga, I., Desplat, J.-C. & Cates, M. E. Colloidal Jamming at Interfaces: A Route to Fluid-Bicontinuous Gels. *Science* **309,** 2198–2201 (2005).
41. Bray, A. J. Theory of phase-ordering kinetics. *Adv. Phys.* **43,** 357–459 (1994).
42. Chan, V. W. L. & Thornton, K. Channel size distribution of complex three-dimensional microstructures calculated from the topological characterization of isodistance structures. *Acta Mater.* **60,** 2509–2517 (2012).
43. Grattoni, C. A., Dawe, R. A., Seah, C. Y. & Gray, J. D. Lower critical solution coexistence curve and physical properties (density, viscosity, surface tension, and interfacial tension) of 2,6-lutidine + water. *J. Chem. Eng. Data* **38,** 516–519 (1993).
44. Cahn, J. W. On spinodal decomposition. *Acta Metall.* **9,** 795–801 (1961).
45. Pagonabarraga, I., Desplat, J.-C., Wagner, A. J. & Cates, M. E. Interfacial dynamics in 3D binary fluid demixing: animation studies. *New J. Phys.* **3,** 1–18 (2001).
46. Lilleodden, E. T. & Voorhees, P. W. On the topological, morphological, and microstructural characterization of nanoporous metals. *MRS Bull.* **43,** 20–26 (2018).
47. Jinnai, H., Nishikawa, Y. & Hashimoto, T. Curvature distributions of spinodal interface in a condensed matter system. *Phys. Rev. E* **59,** R2554–R2557 (1999).
48. Russel, W. B., Saville, D. A. & Schowalter, W. R. *Colloidal Dispersions*. (Cambridge University Press, 1989).
49. Pickering, Spencer, U. Emulsions. *J. Chem. Soc. Trans.* 2001–2021 (1907).
50. Marku, D., Wahlgren, M., Rayner, M., Sjöö, M. & Timgren, A. Characterization of starch Pickering emulsions for potential applications in topical formulations. *Int. J. Pharm.* **428,** 1–7 (2012).
51. Dickinson, E. Food emulsions and foams: Stabilization by particles. *Curr. Opin. Colloid Interface Sci.* **15,** 40–49 (2010).
52. Binks, B. P. Particles as surfactants—similarities and differences. *Curr. Opin. Colloid Interface Sci.* **7,** 21–41 (2002).
53. Huang, C. *et al.* Bicontinuous structured liquids with sub-micrometre domains using nanoparticle surfactants. *Nat. Nanotechnol.* **12,** 1060–1063 (2017).
54. Herzig, E. M., White, K. A., Schofield, A. B., Poon, W. C. K. & Clegg, P. S.

Bicontinuous emulsions stabilized solely by colloidal particles. *Nat. Mater.* **6,** 966–971 (2007).
55. Clegg, P. S. *et al.* Emulsification of Partially Miscible Liquids Using Colloidal Particles: Nonspherical and Extended Domain Structures. 5984–5994 (2007).
56. Inoue, S. in *Handbook of Biological Confocal Microscopy* 1–17 (Springer Science+Business Media, 2006).
57. Reeves, M., Stratford, K. & Thijssen, J. H. J. Quantitative morphological characterization of bicontinuous Pickering emulsions via interfacial curvatures. *Soft Matter* **12,** 4082–4092 (2016).
58. Myers, D. *Surfactant Science and Technology*. (Wiley-Interscience, 2006).
59. Haase, M. F., Stebe, K. J. & Lee, D. Continuous Fabrication of Hierarchical and Asymmetric Bijel Microparticles , Fibers , and Membranes by Solvent Transfer-Induced Phase Separation (STRIPS). 7065–7071 (2015). doi:10.1002/adma.201503509
60. Haase, M. F. *et al.* Multifunctional nanocomposite hollow fiber membranes by solvent transfer induced phase separation. *Nat. Commun.* **8,** 1234 (2017).
61. Di Vitantonio, G., Wang, T., Haase, M. F., Stebe, K. J. & Lee, D. Robust Bijels for Reactive Separation via Silica-Reinforced Nanoparticle Layers. *ACS Nano* **13,** 26–31 (2019).
62. Lee, M. N., Thijssen, J. H. J., Witt, J. A., Clegg, P. S. & Mohraz, A. Making a Robust Interfacial Scaffold: Bijel Rheology and its Link to Processability. *Adv. Funct. Mater.* **23,** 417–423 (2013).
63. Ng, L. H. & Sadoway, D. R. Density measurements in the succinonitrile–water system. *Can. J. Chem.* **66,** 2428–2430 (1988).
64. Firoozmand, H., Murray, B. S. & Dickinson, E. Interfacial Structuring in a Phase-Separating Mixed Biopolymer Solution Containing Colloidal Particles. *Langmuir* **25,** 1300–1305 (2009).
65. Rumble, K. A., Thijssen, J. H. J., Schofield, A. B. & Clegg, P. S. Compressing a spinodal surface at fixed area: bijels in a centrifuge. *Soft Matter* **12,** 4375–4383 (2016).
66. Witt, J. A. High Energy and Power Co-Continuous Electrodes Derived from Bijels. (University of California, Irvine, 2015).
67. Cai, D. & Clegg, P. S. Stabilizing bijels using a mixture of fumed silica nanoparticles. *Chem. Commun.* **51,** 16984–16987 (2015).
68. Bai, L., Fruehwirth, J. W., Cheng, X. & Macosko, C. W. Dynamics and rheology of nonpolar bijels. *Soft Matter* **11,** 5282–5293 (2015).
69. Jung, Y. & Torquato, S. Fluid permeabilities of triply periodic minimal surfaces. *Phys. Rev. E - Stat. Nonlinear, Soft Matter Phys.* **72,** 1–8 (2005).
70. Schoen, A. H. Infinite Periodic Minimal Surfaces Without Self-Intersections. *NASA Tech. Note* (1970).
71. Billiet, T., Vandenhaute, M., Schelfhout, J., Van Vlierberghe, S. & Dubruel, P. A review of trends and limitations in hydrogel-rapid prototyping for tissue engineering. *Biomaterials* **33,** 6020–6041 (2012).
72. Kwon, Y., Thornton, K. & Voorhees, P. W. Coarsening of bicontinuous structures

via nonconserved and conserved dynamics. *Phys. Rev. E - Stat. Nonlinear, Soft Matter Phys.* **75,** 1–5 (2007).
73. Kwon, Y., Thornton, K. & Voorhees, P. W. Morphology and topology in coarsening of domains via non-conserved and conserved dynamics. *Philos. Mag.* **90,** 317–335 (2010).
74. Frijters, S. & Harting, J. Self-assembled porous media from particle-stabilized emulsions. 2–5 (2014). at <http://arxiv.org/abs/1408.2974>
75. Lee, M. N. & Mohraz, A. Bicontinuous Macroporous Materials from Bijel Templates. *Adv. Mater.* **22,** 4836–4841 (2010).
76. Fried, J. R. *Polymer Science and Technology*. (Prentice-Hall, 2003).
77. Lee, M. N. & Mohraz, A. Hierarchically Porous Silver Monoliths from Colloidal Bicontinuous Interfacially Jammed Emulsion Gels. *J. Am. Chem. Soc.* **133,** 6945–6947 (2011).
78. Thorson, T. J., Botvinick, E. L. & Mohraz, A. Composite Bijel-Templated Hydrogels for Cell Delivery. *ACS Biomater. Sci. Eng.* **4,** (2018).
79. Witt, J. A., Mumm, D. R. & Mohraz, A. Microstructural tunability of co-continuous bijel-derived electrodes to provide high energy and power densities. *J. Mater. Chem. A* **4,** 1000–1007 (2016).
80. Lee, M. N. *et al.* Developing Monolithic Nanoporous Gold with Hierarchical Bicontinuity Using Colloidal Bijels. *J. Phys. Chem. Lett.* **5,** 809–812 (2014).
81. Wang, H., Casalongue, H. S., Liang, Y. & Dai, H. Ni(OH) 2 Nanoplates Grown on Graphene as Advanced Electrochemical Pseudocapacitor Materials. *J. Am. Chem. Soc.* **132,** 7472–7477 (2010).
82. Ji, J. *et al.* Nanoporous Ni(OH) 2 Thin Film on 3D Ultrathin-Graphite Foam for Asymmetric Supercapacitor. *ACS Nano* **7,** 6237–6243 (2013).
83. Tang, Z., Tang, C. & Gong, H. A High Energy Density Asymmetric Supercapacitor from Nano-architectured Ni(OH)2/Carbon Nanotube Electrodes. *Adv. Funct. Mater.* **22,** 1272–1278 (2012).
84. Lynn, A. D., Blakney, A. K., Kyriakides, T. R. & Bryant, S. J. Temporal progression of the host response to implanted poly(ethylene glycol)-based hydrogels. *J. Biomed. Mater. Res. Part A* **96A,** 621–631 (2011).
85. Swierczewska, M., Lee, K. C. & Lee, S. What is the future of PEGylated therapies? *Expert Opin. Emerg. Drugs* **20,** 531–536 (2015).
86. Alberts, B. *et al. Essential Cell Biology*. (Taylor & Francis, 2004).
87. Chen, Y.-C. *et al.* Functional Human Vascular Network Generated in Photocrosslinkable Gelatin Methacrylate Hydrogels. *Adv. Funct. Mater.* **22,** 2027–2039 (2012).
88. Nguyen, A. H., McKinney, J., Miller, T., Bongiorno, T. & McDevitt, T. C. Gelatin methacrylate microspheres for controlled growth factor release. *Acta Biomater.* **13,** 101–110 (2015).
89. Zhao, W. *et al.* A comprehensive study and comparison of four types of zwitterionic hydrogels. *J. Mater. Sci.* **53,** 13813–13825 (2018).
90. Xiao, Z. *et al.* Zwitterionic poly(sulfobetaine methacrylate) hydrogels with optimal mechanical properties for improving wound healing in vivo . *J. Mater. Chem. B*

(2019). doi:10.1039/c8tb02590h
91. Hsieh, J. *Computed Tomography: Principles, Design, Artifacts, and Recent Advances*. (SPIE Press, 2009).
92. Shearer, T., Bradley, R. S., Hidalgo-Bastida, L. A., Sherratt, M. J. & Cartmell, S. H. Three-dimensional visualisation of soft biological structures by X-ray computed micro-tomography. *J. Cell Sci.* **129,** 2483–2492 (2016).
93. Hopkins, S. Porous Aluminum Mold Materials: "New Technology in Thermoform Tool-making. in *SAE Technical Paper Series* **1,** (2001).
94. Zhang, Y. S., Choi, S. & Xia, Y. Inverse opal scaffolds for applications in regenerative medicine. *Soft Matter* **9,** 9747 (2013).
95. Zhang, H., Yu, X. & Braun, P. V. Three-dimensional bicontinuous ultrafast-charge and -discharge bulk battery electrodes. *Nat. Nanotechnol.* **6,** 277–281 (2011).
96. Patil, U. M. *et al.* PolyHIPE Derived Freestanding 3D Carbon Foam for Cobalt Hydroxide Nanorods Based High Performance Supercapacitor. *Sci. Rep.* **6,** 35490 (2016).
97. Synopsis. Simpleware: Converting 3D Images into Models. Reference Guide. (2016).
98. Agarwal, Y., Śmigaj, W., Young, P. G., Cotton, R. & Tompsett, P. Image-based software solutions for advanced materials processing and characterization. *Mater. Today Proc.* **4,** 1860–1867 (2017).
99. Lee, T. C., Kashyap, R. L. & Chu, C. N. Building Skeleton Models via 3-D Medial Surface Axis Thinning Algorithms. *CVGIP Graph. Model. Image Process.* **56,** 462–478 (1994).
100. Fukano, Y. *et al.* Epidermal and dermal integration into sphere-templated porous poly(2-hydroxyethyl methacrylate) implants in mice. *J. Biomed. Mater. Res. - Part A* **94,** 1172–1186 (2010).
101. Cates, M. E. & Clegg, P. S. Bijels: a new class of soft materials. *Soft Matter* **4,** 2132 (2008).
102. Choi, S., Zhang, Y., MacEwan, M. R. & Xia, Y. Neovascularization in Biodegradable Inverse Opal Scaffolds with Uniform and Precisely Controlled Pore Sizes. *Adv. Healthc. Mater.* **2,** 145–154 (2013).
103. Witt, J. A., Mumm, D. R. & Mohraz, A. Bijel reinforcement by droplet bridging: a route to bicontinuous materials with large domains. *Soft Matter* **9,** 6773 (2013).
104. Mitchell, N. P., Koning, V., Vitelli, V. & Irvine, W. T. M. Fracture in sheets draped on curved surfaces. *Nat. Mater.* **16,** 89–93 (2017).
105. Bade, N. D., Kamien, R. D., Assoian, R. K. & Stebe, K. J. Curvature and Rho activation differentially control the alignment of cells and stress fibers. *Sci. Adv.* **3,** 1–9 (2017).
106. Bade, N. D., Xu, T., Kamien, R. D., Assoian, R. K. & Stebe, K. J. Gaussian Curvature Directs Stress Fiber Orientation and Cell Migration. *Biophys. J.* **114,** 1467–1476 (2018).
107. Werner, M. *et al.* Surface Curvature Differentially Regulates Stem Cell Migration and Differentiation via Altered Attachment Morphology and Nuclear Deformation. *Adv. Sci.* **4,** 1–11 (2017).

108. Veiseh, O. *et al.* Size- and shape-dependent foreign body immune response to materials implanted in rodents and non-human primates. *Nat. Mater.* **14,** 643–652 (2015).
109. Gommes, C. J., Bons, A.-J., Blacher, S., Dunsmuir, J. H. & Tsou, A. H. Practical methods for measuring the tortuosity of porous materials from binary or gray-tone tomographic reconstructions. *AIChE J.* **55,** 2000–2012 (2009).
110. Elwinger, F., Pourmand, P. & Furó, I. Diffusive Transport in Pores. Tortuosity and Molecular Interaction with the Pore Wall. *J. Phys. Chem. C* **121,** 13757–13764 (2017).
111. Zenyuk, I. V., Parkinson, D. Y., Connolly, L. G. & Weber, A. Z. Gas-diffusion-layer structural properties under compression via X-ray tomography. *J. Power Sources* **328,** 364–376 (2016).
112. Inoue, T., Ohmura, H. & Murata, D. Cloud point temperature of polyoxyethylene-type nonionic surfactants and their mixtures. *J. Colloid Interface Sci.* **258,** 374–382 (2003).
113. Ozdil, D. & Aydin, H. M. Polymers for medical and tissue engineering applications. *J. Chem. Technol. Biotechnol.* **89,** 1793–1810 (2014).
114. Patterson, J., Martino, M. M. & Hubbell, J. A. Biomimetic Materials in Tissue Engineering. *Mater. Today* **13,** 14–22 (2010).
115. Malafaya, P. B., Silva, G. A. & Reis, R. L. Natural-origin polymers as carriers and scaffolds for biomolecules and cell delivery in tissue engineering applications. *Adv. Drug Deliv. Rev.* **59,** 207–233 (2007).
116. Ahmed, T. A. E., Dare, E. V. & Hincke, M. Fibrin: a versatile scaffold for tissue engineering applications. *Tissue Eng. Part B Rev.* **14,** 199–215 (2008).
117. Brown, A. C. & Barker, T. H. Fibrin-based biomaterials: Modulation of macroscopic properties through rational design at the molecular level. *Acta Biomater.* **10,** 1502–1514 (2014).
118. Zhang, G., Wang, X., Wang, Z., Zhang, J. & Suggs, L. A PEGylated fibrin patch for mesenchymal stem cell delivery. *Tissue Eng.* **12,** 9–19 (2006).
119. Hokugo, A., Takamoto, T. & Tabata, Y. Preparation of Hybrid Scaffold from Fibrin and Biodegradable Polymer Fiber. *Biomaterials* **27,** 61–67 (2006).
120. Wang, C., Varshney, R. R. & Wang, D.-A. Therapeutic Cell Delivery and Fate Control in Hydrogels and Hydrogel Hybrids. *Adv. Drug Deliv. Rev.* **62,** 699–710 (2010).
121. Benton, J. A., Fairbanks, B. D. & Anseth, K. S. Characterization of Valvular Interstitial Cell Function in Three Dimensional Matrix Metalloproteinase Degradable PEG Hydrogels. *Biomaterials* **30,** 6593–6603 (2009).
122. Lutolf, M. P. & Hubbell, J. a. Synthetic biomaterials as instructive extracellular microenvironments for morphogenesis in tissue engineering. *Nat. Biotechnol.* **23,** 47–55 (2005).
123. Kraehenbuehl, T. P., Ferreira, L. S., Zammaretti, P., Hubbell, J. A. & Langer, R. Cell-Responsive Hydrogel for Encapsulation of Vascular Cells. *Biomaterials* **30,** 4318–4324 (2009).
124. Kim, J. *et al.* Characterization of the Crosslinking Kinetics of Multi-arm

Poly(ethylene glycol) Hydrogels Formed via Michael-type Addition. *Soft Matter* **12,** 2076–2085 (2016).
125. Langer, R. & Tirrell, D. A. Designing Materials for Biology and Medicine. *Nature* **428,** 487–492 (2004).
126. Choi, S., Zhang, Y. & Xia, Y. Three-Dimensional Scaffolds for Tissue Engineering : The Importance of Uniformity in Pore Size and Structure. **26,** 19001–19006 (2010).
127. Bai, H., Polini, A., Delattre, B. & Tomsia, A. P. Thermoresponsive Composite Hydrogels with Aligned Macroporous Structure by Ice-Templated Assembly. *Chem. Mater.* **25,** 4551–4556 (2013).
128. Welzel, P. B. *et al.* Macroporous StarPEG-Heparin Cryogels. *Biomacromolecules* **13,** 2349–2358 (2012).
129. Jiang, B., Waller, T. M., Larson, J. C., Appel, A. A. & Brey, E. M. Fibrin-Loaded Porous Poly(Ethylene Glycol) Hydrogels as Scaffold Materials for Vascularized Tissue Formation. *Tissue Eng. Part A* **19,** 224–234 (2013).
130. Park, J. S. *et al.* In Vitro and In Vivo Test of PEG/PCL-Based Hydrogel Scaffold for Cell Delivery Application. *J. Control. Release* **124,** 51–59 (2007).
131. Oh, B. H. L., Bismarck, A. & Chan-Park, M. B. High internal phase emulsion templating with self-emulsifying and thermoresponsive chitosan-graft -PNIPAM-graft -oligoproline. *Biomacromolecules* **15,** 1777–1787 (2014).
132. Mollet, B. B. *et al.* Mechanically Robust Electrospun Hydrogel Scaffolds Crosslinked via Supramolecular Interactions. *Macromol. Biosci.* **17,** (2017).
133. Li, M. *et al.* Co-Electrospun Poly(lactide-co-glycolide), Gelatin, and Elastin Blends for Tissue Engineering Scaffolds. *J. Biomed. Mater. Res. Part A* **79A,** 963–973 (2006).
134. Melchels, F. P. W. *et al.* Mathematically defined tissue engineering scaffold architectures prepared by stereolithography. *Biomaterials* **31,** 6909–6916 (2010).
135. Imperiali, L., Clasen, C., Fransaer, J., Macosko, C. W. & Vermant, J. A simple route towards graphene oxide frameworks. *Mater. Horizons* **1,** 139–145 (2014).
136. van Blaaderen, A. & Vrij, A. Synthesis and Characterization of Colloidal Dispersions of Fluorescent, Monodisperse Silica Spheres. *Langmuir* **8,** 2921–2931 (1992).
137. Larson, R. *The Structure and Rheology of Complex Fluids*. (Oxford University Press Inc, 1999).
138. Zustiak, S. P. & Leach, J. B. Hydrolytically Degradable Poly(Ethylene Glycol) Hydrogel Scaffolds with Tunable Degradation and Mechanical Properties. *Biomacromolecules* **11,** 1348–1357 (2010).
139. Neumann, A. J., Quinn, T. & Bryant, S. J. Nondestructive Evaluation of a New Hydrolytically Degradable and Photo-clickable PEG Hydrogel for Cartilage Tissue Engineering. *Acta Biomater.* **39,** 1–11 (2016).
140. Yu, J. *et al.* Synthesis and Characterization of MMP Degradable and Maleimide Cross-linked PEG Hydrogels for Tissue Engineering Scaffolds. *Polym. Degrad. Stab.* **133,** 312–320 (2016).
141. Klopfleisch, R. & Jung, F. The pathology of the foreign body reaction against

biomaterials. *J. Biomed. Mater. Res. - Part A* **105,** 927–940 (2017).
142. Williams, D. F. Tissue-biomaterial interactions. *J. Mater. Sci.* **22,** 3421–3445 (1987).
143. Ratner, B. D. & Bryant, S. J. Biomaterials: Where We Have Been and Where We Are Going. *Annu. Rev. Biomed. Eng.* **6,** 41–75 (2004).
144. Anderson, J. M. Biological Responses to Materials. *Annu. Rev. Mater. Res.* **31,** 81–110 (2001).
145. Doloff, J. C. *et al.* Colony stimulating factor-1 receptor is a central component of the foreign body response to biomaterial implants in rodents and non-human primates. *Nat. Mater.* **16,** 671–680 (2017).
146. Hoffman, A. S. Non-Fouling Surface Technologies. *J. Biomater. Sci. Polym. Ed.* **10,** 1011–1014 (1999).
147. Lynn, A. D., Kyriakides, T. R. & Bryant, S. J. Characterization of the in vitro macrophage response and in vivo host response to poly(ethylene glycol)-based hydrogels. *J. Biomed. Mater. Res. Part A* **93A,** 941–953 (2009).
148. Alcantar, N. A., Aydil, E. S. & Israelachvili, J. N. Polyethylene glycol – coated biocompatible surfaces. *J. Biomed. Mater. Res. Part A* **51,** 343–351 (2000).
149. Nurioglu, A. G., Esteves, A. C. C. & de With, G. Non-toxic, non-biocide-release antifouling coatings based on molecular structure design for marine applications. *J. Mater. Chem. B* **3,** 6547–6570 (2015).
150. Heuberger, M., Drobek, T. & Spencer, N. D. Interaction Forces and Morphology of a Protein-Resistant Poly(ethylene glycol) Layer. *Biophys. J.* **88,** 495–504 (2005).
151. Giraldo, J. A. *et al.* The impact of cell surface PEGylation and short-course immunotherapy on islet graft survival in an allogeneic murine model. *Acta Biomater.* **49,** 272–283 (2017).
152. Franz, S., Rammelt, S., Scharnweber, D. & Simon, J. C. Immune responses to implants – A review of the implications for the design of immunomodulatory biomaterials. *Biomaterials* **32,** 6692–6709 (2011).
153. Niidome, T. *et al.* PEG-modified gold nanorods with a stealth character for in vivo applications. *J. Control. Release* **114,** 343–347 (2006).
154. Jenney, C. R. & Anderson, J. M. Effects of surface-coupled polyethylene oxide on human macrophage adhesion and foreign body giant cell formationin vitro. *J. Biomed. Mater. Res.* **44,** 206–216 (1999).
155. Xie, X. *et al.* Reduction of measurement noise in a continuous glucose monitor by coating the sensor with a zwitterionic polymer. *Nat. Biomed. Eng.* 1 (2018). doi:10.1038/s41551-018-0273-3
156. Leigh, B. L. *et al.* Photopolymerizable Zwitterionic Polymer Patterns Control Cell Adhesion and Guide Neural Growth. *Biomacromolecules* **18,** 2389–2401 (2017).
157. Tah, T. & Bernards, M. T. Nonfouling polyampholyte polymer brushes with protein conjugation capacity. *Colloids Surf. B* **93,** 195–201 (2012).
158. Zhao, T., Chen, K. & Gu, H. Investigations on the Interactions of Proteins with Polyampholyte-Coated Magnetite Nanoparticles. *J. Phys. Chem. B* **117,** 14129–14135 (2013).
159. Kozlovskaya, V. *et al.* Ultrathin polymeric coatings based on hydrogen-bonded

polyphenol for protection of pancreatic islet cells. *Adv. Funct. Mater.* **22,** 3389–3398 (2012).
160. Pham-Hua, D. *et al.* Islet encapsulation with polyphenol coatings decreases pro-inflammatory chemokine synthesis and T cell trafficking. *Biomaterials* **128,** 19–32 (2017).
161. Kyung, Y., Chen, E. & Liu, W. F. Biomolecular strategies to modulate the macrophage response to implanted materials. *J. Mater. Chem. B* **4,** 1600–1609 (2016).
162. Kim, Y. K., Que, R., Wang, S. & Liu, W. F. Modification of Biomaterials with a Self-Protein Inhibits the Macrophage Response. *Adv. Healthc. Mater.* **3,** 989–994 (2014).
163. Stachelek, S. J. *et al.* The effect of CD47 modified polymer surfaces on inflammatory cell attachment and activation. *Biomaterials* **32,** 4317–4326 (2011).
164. Ratner, B. D. A pore way to heal and regenerate: 21st century thinking on biocompatibility. *Regen. Biomater.* **3,** 107–110 (2016).
165. Sussman, E. M., Halpin, M. C., Muster, J., Moon, R. T. & Ratner, B. D. Porous Implants Modulate Healing and Induce Shifts in Local Macrophage Polarization in the Foreign Body Reaction. *Ann. Biomed. Eng.* **42,** 1508–1516 (2014).
166. Brauker, J. H. *et al.* Neovascularization of synthetic membranes directed by membrane microarchitecture. *J. Biomed. Mater. Res.* **29,** 1517–1524 (1995).
167. Wang, T., Luu, T. U., Chen, A., Khine, M. & Liu, W. F. Topographical modulation of macrophage phenotype by shrink-film multi-scale wrinkles. *Biomater. Sci.* **4,** 948–952 (2016).
168. Luu, T. U., Gott, S. C., Woo, B. W. K., Rao, M. P. & Liu, W. F. Micro- and Nanopatterned Topographical Cues for Regulating Macrophage Cell Shape and Phenotype. *ACS Appl. Mater. Interfaces* **7,** 28665–28672 (2015).
169. Salthouse, T. N. Some aspects of macrophage behavior at the implant interface. *J. Biomed. Mater. Res.* **18,** 395–401 (1984).
170. Matlaga, B. F., Yasenchak, L. P. & Salthouse, T. N. Tissue response to implanted polymers: The significance of sample shape. *J. Biomed. Mater. Res.* **10,** 391–397 (1976).
171. Bryers, J. D., Giachelli, C. M. & Ratner, B. D. Engineering Biomaterials to Integrate and Heal: The Biocompatibility Paradigm Shifts. *Biotechnol. Bioeng.* **109,** 1898–1911 (2012).
172. Weaver, J. D. *et al.* Design of a vascularized synthetic poly(ethylene glycol) macroencapsulation device for islet transplantation. *Biomaterials* **172,** 54–65 (2018).
173. Mooney, D. J., Baldwin, D. F., Suh, N. P., Vacanti, J. P. & Langer, R. Novel approach to fabricate porous sponges of poly(d,l-lactic-co-glycolic acid) without the use of organic solvents. *Biomaterials* **17,** 1417–1422 (1996).
174. Bhardwaj, N. & Kundu, S. C. Electrospinning: A fascinating fiber fabrication technique. *Biotechnol. Adv.* **28,** 325–347 (2010).
175. Stratford, K., Adhikari, R., Pagonabarraga, I., Desplat, J.-C. & Cates, M. E. Colloidal Jamming at Interfaces: A Route to Fluid-Bicontinuous Gels. *Science (80-*

.). **309,** 2198–2201 (2005).
176. Herzig, E. M. *et al.* The bijel: a bicontinuous interfacially jammed emulsion gel. *NSTI-Nanotech* **2,** 657–660 (2008).
177. White, K. A. *et al.* Inversion of particle-stabilized emulsions of partially miscible liquids by mild drying of modified silica particles. *J. Colloid Interface Sci.* **359,** 126–135 (2011).
178. Chen, X. *et al.* Oxidation degradation of rhodamine B in aqueous by UV/S 2O 82-treatment system. *Int. J. Photoenergy* **2012,** (2012).
179. Schindelin, J. *et al.* Fiji: An open-source platform for biological-image analysis. *Nat. Methods* **9,** 676–682 (2012).
180. Preibisch, S., Saalfeld, S. & Tomancak, P. Globally optimal stitching of tiled 3D microscopic image acquisitions. *Bioinformatics* **25,** 1463–1465 (2009).
181. Gurlin, R. E. *et al.* Vascularization and innervation of slits within polydimethylsiloxane sheets in the subcutaneous space of athymic nude mice. *J. Tissue Eng.* **8,** (2017).
182. Lucas, T. *et al.* Differential Roles of Macrophages in Diverse Phases of Skin Repair. *J. Immunol.* **184,** 3964–3977 (2010).
183. Yu, T. *et al.* Temporal and spatial distribution of macrophage phenotype markers in the foreign body response to glutaraldehyde-crosslinked gelatin hydrogels. *J. Biomater. Sci. Polym. Ed.* **27,** 721–742 (2016).
184. Edelstein, A. D. *et al.* Advanced methods of microscope control using μManager software. *J. Biol. Methods* **1,** 10 (2014).
185. Armulik, A., Abramsson, A. & Betsholtz, C. Endothelial/Pericyte Interactions. *Circ. Res.* **97,** 512–523 (2005).
186. Isenhath, S. N. *et al.* A mouse model to evaluate the interface between skin and a percutaneous device. *J. Biomed. Mater. Res. Part A* **83A,** 915–922 (2007).